



THE EFFECT OF MICROSTRUCTURE ON MECHANICAL PROPERTIES IN INERTIA WELDED TITANIUM 6-4

By

ADAM YATES

A thesis submitted to the
University of Birmingham
for the degree of
MASTER OF RESEARCH

School of Metallurgy and Materials
College of Engineering and Physical Sciences
University of Birmingham
May 2015

**UNIVERSITY OF
BIRMINGHAM**

University of Birmingham Research Archive

e-theses repository

This unpublished thesis/dissertation is copyright of the author and/or third parties. The intellectual property rights of the author or third parties in respect of this work are as defined by The Copyright Designs and Patents Act 1988 or as modified by any successor legislation.

Any use made of information contained in this thesis/dissertation must be in accordance with that legislation and must be properly acknowledged. Further distribution or reproduction in any format is prohibited without the permission of the copyright holder.

**This Thesis is dedicated to my parents Nicola Yates and Andrew Yates
along with other family members including Brothers, Grandparents
and Great Grandparents**

ABSTRACT

The inertia welding (IW) of Ti64 was examined in terms of the microstructure and mechanical properties. The microstructure from two smalls scale inertia welded rings was observed using SEM. These microstructures were assessed in both the Hoop and Radial directions. Mechanical testing including micro-hardness, mechanical threshold and crack propagation testing, fracture toughness, tensile testing and low cycle testing was evaluated. The results show that the microstructures of both IW and LFW Ti64 are very similar with various weld zones being observed. The micro-hardness is far superior in the weld zone to that of the parent material. The most significant controlling parameter of the microstructure is the cooling rate.

The Tensile properties of both IW and LFW Ti64 are superior to that of the parent and failure will not occur within the weld, although the LCF behaviour was not as favourable in IW. Crack growth rate is slower in the hoop direction than radial direction although this trend is reversed at increased temperature due to a switch from transgranular to intergranular crack growth.

This work suggests that IW of Ti64 shows promise, although further work is required on larger scale welds before the manufacture of fan disks made from IW Ti64 can be substantiated.

ACKNOWLEDGEMENTS

I am using this opportunity to express my gratitude to everyone who has supported me throughout the course of this Masters Research programme.

Firstly I would like to thank my Supervisor's Dr Hangyue Li for her guidance, motivation and immense knowledge. Her guidance has aided me greatly during my research and I owe much of this thesis to her support.

I would like to thank Shuang Xie for all of his help and ideas during our collaborated research along with his great enthusiasm.

I would also like to thank other members of the department, Prof. Paul Bowen for accepting me onto the programme and financial support, Tim Doel and Dave Price for their help in the testing and also Andrea Malin and Jenny Henderson for their help during the administration and submission of my work.

Thanks to Tim Halford and Peter Stevens at Rolls Royce, Plc for their aid in supplying test material without which none of this research could be done.

Last but not least thanks to my family for all of your support over the years both financially and emotionally.

Thank you,

Adam

TABLE OF CONTENTS

List of Figures.....	IV - IX
List of Tables.....	X
List of Abbreviations.....	XI
1 INTRODUCTION.....	1 - 3
1.1 Background.....	3
1.2 Project aims and objectives.....	4-5
2 METALLURGY OF TITANIUM ALLOYS.....	6
2.1 Introduction.....	6
2.2 Classifications of Titanium alloys.....	6
2.2.1 α and near α titanium alloys.....	7
2.2.2 $\alpha - \beta$ titanium alloys.....	7 - 8
2.2.3 β titanium alloys.....	8
2.3 Processing methods and heat treatment.....	8
2.3.1 Titanium processing methods.....	9
2.3.2 Heat treatment.....	10
2.4 $\alpha - \beta$ Titanium alloys.....	10
2.4.1 Phases in $\alpha - \beta$ titanium alloys.....	11 - 12
2.4.2 Phase transformations in $\alpha - \beta$ titanium alloys.....	12 - 13
2.4.3 Microstructure of $\alpha - \beta$ titanium alloys.....	13 - 14
2.5 Ti-6Al-4V.....	14
2.5.1 Phase transformations in Ti64.....	15 - 17
2.6 Mechanical behaviour of Titanium alloys.....	18
2.6.1 Fatigue.....	18 - 19
2.6.1.1 Mechanical threshold.....	19
2.6.1.2 Low cycle fatigue.....	20
2.6.1.3 Fatigue crack propagation.....	21
2.6.2 Tensile strength.....	21
2.6.3 Fracture toughness.....	22
3 INERTIA WELDING AND ITS APPLICATION IN TITANIUM ALLOYS.....	23
3.1 Introduction.....	23
3.2 Friction welding.....	23 - 25
3.3 Inertia welding.....	25
3.3.1 Stages of Inertia welding.....	25 - 26
3.3.2 Process variables.....	26
3.4 Inertia welding of Titanium alloys.....	27

3.4.1	The weld region.....	27
3.4.1.1	The CWZ in inertia welding.....	27 - 28
3.4.1.2	The TMAZ in inertia welding.....	28
3.4.1.3	The HAZ in inertia welding.....	29
3.4.1.4	Weld width in inertia welding.....	30
3.4.2	Mechanical properties of Inertia welded titanium alloys.....	31
3.4.2.1	Micro-hardness.....	31
3.4.2.2	Tensile properties.....	32
3.4.2.3	Fatigue and crack propagation.....	32
4	EXPERIMENTAL AND ANALYTICAL METHODS.....	33
4.1	Materials.....	33
4.2	Welding of the materials.....	33 - 34
4.3	Post weld heat treatment (PWHT).....	34
4.4	Sample preparation.....	34 - 38
4.5	Microstructure analysis.....	39
4.5.1	Optical microscopy (OM).....	39
4.5.2	Scanning electron microscopy (SEM).....	39 - 41
4.6	Mechanical testing.....	42
4.6.1	Micro-hardness testing.....	42 - 43
4.6.2	Mechanical threshold testing.....	44 - 48
4.6.3	Low cycle fatigue (LCF) testing.....	48 - 49
4.6.4	Tensile testing.....	49
4.6.5	Fracture toughness testing.....	50
5	RESULTS AND DISCUSSION.....	51
5.1	Characterisation of Ti64 to Ti64 inertia weld.....	51
5.1.1	Microstructure of parent material.....	51 - 53
5.1.2	Microstructure of weld region.....	53 - 56
5.1.2.1	CWZ.....	57 - 58
5.1.2.2	TMAZ.....	59 - 63
5.1.2.3	HAZ.....	63 - 66
5.1.3	Micro-hardness distribution across the weld region.....	67 - 70
5.2	Mechanical testing.....	71
5.2.1	Effect of welding parameters and temperature on Tensile strength.....	71 - 74
5.2.2	Effect of welding parameters on LCF behaviour.....	75 - 76
5.2.3	Effect of welding parameters, weld orientation and temperature on Mechanical threshold and Crack Propagation.....	77 - 82
5.2.4	Effect of welding parameters, weld orientation and temperature on Fracture toughness.....	83 - 86

6 CONCLUSIONS.....	87
6.1 Microstructure development in Inertia welded Ti64 and its effect on micro-hardness.....	87
6.2 Mechanical properties in Inertia welded Ti64.....	88
6.3 General conclusions.....	89
7 FUTURE WORK.....	90
8 REFERENCES.....	91 - 97

LIST OF FIGURES

Figure 1.1 Image of Rolls Royce Trent XWB engine.....	1
Figure 1.2 Schematic of modern day Rolls Royce Trent engine and the materials used in its production.....	2
Figure 2.1 Schematic diagram showing volume fractions of α and β phases and concentrations of Al and V in Ti64 in relation to temperature.....	15
Figure 2.2 Phase diagram and corresponding microstructures in relation to different annealing temperatures and cooling rates.....	16
Figure 3.1 Photographs of the inertia welding process during the a) initial phase, b) intermediate phase and c) consolidation stage.....	26
Figure 4.1 Schematic diagram of the weld samples taken from the PDRIW119-02 welded ring to be used for Fracture toughness, Low cycle fatigue, crack propagation and tensile testing.....	35
Figure 4.2 Schematic diagram of the weld samples taken from the PDRIW119-03 welded ring to be used for Fracture toughness, Low cycle fatigue, crack propagation and tensile testing.....	36
Figure 4.3 Schematic diagram showing how the samples were taken from the welded rings to carry out microstructure analysis and crack growth testing.....	37

Figure 4.4 Photograph of the Beuhler-Isomet 4000 linear precision saw used to section the samples to the required geometries.....	38
Figure 4.5 Photograph of the Opal 460 Mounting press used to prepare samples in Bakelite for microstructure analysis and micro-hardness testing.....	38
Figure 4.6 Photograph of the Struers Labopol-5 automatic polishing machine used to grind and polish the samples used for microstructure analysis and micro-hardness testing.....	38
Figure 4.7 Photograph of the S4000 field emission gun (FEG) electron microscope used for microstructure analysis.....	41
Figure 4.8 Photograph of the Jeol 7000F microscope with Oxford Inca EDS, Wave WDS and crystal EBSD used for microstructure analysis.....	41
Figure 4.9 Jeol 6060 microscope with Oxford Inca EDS used for microstructure analysis.....	41
Figure 4.10 Optical image taken of an example of a micro-hardness plot across the weld region.....	42
Figure 4.11 Photograph of the Struers automatic hardness testing machine used to carry out the micro-hardness profiles across the weld regions.....	43
Figure 4.12 Optical image showing how the micro-hardness plots were plotted by at least 3 times the width of the diamonds away from each other.....	43
Figure 4.13 Photograph of the Beuhler Isomet – slow speed saw with a silicon cutting blade used to cut the notches for threshold testing and crack propagation work....	44

Figure 4.14 Photograph of an example of one of the Servo-hydraulic testing machine used to carry out the threshold, crack propagation and fracture toughness testing...45

Figure 4.15 Photograph showing the DC power supply, PD wires, PD box and chart recorder used in the threshold, crack propagation and fracture toughness testing...45

Figure 5.1 SEM image of equiaxed α grains in a transformed β matrix at X1000 magnification.....51

Figure 5.2 SEM image of coarse acicular α particles within a transformed β matrix at X3000 magnification.....52

Figure 5.3 Optical image of the weld zone showing the different regions within the weld.....53

Figure 5.4 Optical image of the weld zone showing the shape and width of the weld in the PDRIW119-02 welded ring.....54

Figure 5.5 Optical image of the weld zone showing the shape and width of the weld in the PDRIW119-03 welded ring along with the different regions within the weld.....54

Figure 5.6 SEM image showing the radial flow of the material within the TMAZ within the PDRIW119-03 welded ring at X200 magnification.....56

Figure 5.7 SEM image of the CZ within the PDRIW119-02 weld at X1400 magnification.....57

Figure 5.8 SEM image of the CZ showing the fine acicular α and lathes present within the PDRIW119-03 weld at X2000 magnification.....57

Figure 5.9 SEM image of the basket-weave microstructure observed within the CZ of the PDRIW119-03 weld.....58

Figure 5.10 Optical image showing the hoop flow in the PDRIW119-02 weld.....	59
Figure 5.11 Optical image showing the hoop flow in the PDRIW119-03 weld.....	59
Figure 5.12 Optical image comparing the CZ to the inner TMAZ in the PDRIW119-03 weld.....	60
Figure 5.13 SEM image of the TMAZ within the PDRIW119-02 weld at X10K magnification showing the α and β phases and fine acicular α	61
Figure 5.14 Optical image comparing the inner TMAZ and outer TMAZ within the PDRIW119-03 weld.....	62
Figure 5.15 Optical image comparing the outer TMAZ and HAZ within the PDRIW119-03 weld.....	63
Figure 5.16 Optical image comparing the HAZ and parent material within the PDRIW119-03 weld.....	64
Figure 5.17 SEM image of the HAZ at X3500 magnification showing the transformed β phase and coarse acicular α	65
Figure 5.18 SEM image of the parent material at X2000 magnification showing the variations in secondary α precipitates.....	65
Figure 5.19 Optical images of the changes in weld zone microstructure as you move away from the weld interface.....	66
Figure 5.20 Micro-hardness profile of the PDRIW119-02 weld with high energy density and rotational speed but reduced pressure.....	67
Figure 5.21 Micro-hardness profile of the PDRIW119-03 weld with lower energy density and rotational speed but higher pressure.....	67
Figure 5.22 Micro-hardness profile comparison between the PDRIW119-02 and PDRIW119-03 welds.....	68

Figure 5.23 Micro-hardness profile superimposed onto an optical image of the weld microstructure.....	69
Figure 5.24 Graph showing Stress: Strain curve at 20°C produced by SMaRT for Rolls Royce, Plc at the Swansea Materials Research and Testing facility.....	72
Figure 5.25 Graph showing Stress: Strain curve at 150°C produced by SMaRT for Rolls Royce, Plc at the Swansea Materials Research and Testing facility.....	72
Figure 5.26 Graph showing Stress: Strain curve at 300°C produced by SMaRT for Rolls Royce, Plc at the Swansea Materials Research and Testing facility.....	73
Figure 5.27 Graph showing Stress: Strain curve for PDRIW119-02 weld samples produced by SMaRT for Rolls Royce, Plc at the Swansea Materials Research and Testing facility.....	74
Figure 5.28 Graph showing Stress: Strain curve for PDRIW119-03 weld samples produced by SMaRT for Rolls Royce, Plc at the Swansea Materials Research and Testing facility.....	74
Figure 5.29 Graph showing S-N curves for data produced by SMaRT for Rolls Royce, Plc at the Swansea Materials Research and Testing facility.....	76
Figure 5.30 Graph showing the effect of stress intensity factor (ΔK) on crack growth rate within the weld zones (T003-T012) and the parent material.....	77
Figure 5.31 Graph showing the effect of stress intensity factor (ΔK) on crack growth rate in the Hoop and Radial direction at room temperature.....	81
Figure 5.32 Graph showing the effect of stress intensity factor (ΔK) on crack growth rate in the Hoop and Radial direction at room temperature.....	81

Figure 5.33 Graph showing the effect of stress intensity factor (ΔK) on crack growth rate in the Hoop direction at room temperature and 400°C.....	81
Figure 5.34 Graph showing the effect of stress intensity factor (ΔK) on crack growth rate in the Radial direction at room temperature and 400°C.....	81
Figure 5.35 Optical images of the fracture surface observed in the PDRIW119-02 welds FT003 (Hoop) and FT006 (Radial) at room temperature.....	85
Figure 5.36 Optical images of the fracture surface observed in the PDRIW119-02 welds FT004 and FT008 (Hoop) and FT005 (Radial) at 400°C.....	85
Figure 5.37 Optical images of the fracture surface observed in the PDRIW119-03 welds FT016 (Hoop) and FT013 (Radial) at room temperature.....	85
Figure 5.37 Optical images of the fracture surface observed in the PDRIW119-03 welds FT0010 and FT014 (Hoop) and FT009 and FT011 (Radial) at 400°C.....	85

LIST OF TABLES

Table 4.1 The chemical composition of commercial Ti-64 as supplied by Rolls Royce, Plc.....	33
Table 4.2 The welding parameters that were used in to weld the two rings PDRIW119-02 and PDRIW119-03.....	34
Table 4.3 The grinding and polishing papers used along with the procedures used at each stage of the polishing stages.....	39
Table 4.4 The Scanning Electron microscopes (SEM) used in the microstructure analysis.....	40
Table 5.1 Tensile results of the work carried out by SMaRT for Rolls-Royce, plc at the Swansea Materials Research and testing facility.....	71
Table 5.2 Low cycle fatigue (LCF) results of the work carried out by SMaRT for Rolls-Royce, plc at the Swansea Materials Research and testing facility.....	75
Table 5.3 A summary of the fracture toughness testing results carried out on 12 samples provided by Rolls-Royce, plc at various test parameters.....	83

LIST OF ABBREVIATIONS

Abbreviation	Description
02	PDRIW119-03 Weld
03	PDRIW119-02 Weld
BCC	Body Centred Cubic
CZ / CWZ	Central Weld Zone
CFW	Circular Friction Welding
EBSD	Electron Backscatter Diffraction
EBW	Electron Beam Welding
EDM	Electrical Discharge Machining
EDS	Energy-dispersive X-ray spectroscopy
FEG	Field Emission Gun
FSW	Friction Stir Welding
HAZ	Heat Affected Zone
HCP	Hexagonal Close Packed
ID	Inner Diameter
IW	Inertia Welding
LCF	Low Cycle Fatigue
LFW	Linear Friction Welding
OD	Outer Diameter
OM	Optical Microscope
PD	Potential Difference
PM	Parent Material
PWHT	Post Weld Heat Treatment
RFW	Rotary Friction Welding
SEI	Secondary Electron Imaging
SEM	Scanning Electron Microscope
Ti	Titanium
TIG	Tungsten Inert Gas
TMAZ	Thermo-mechanically Affected Zone
UTS	Ultimate Tensile Strength
WDS	Wave-dispersive X-ray spectroscopy

CHAPTER 1 INTRODUCTION

Over the last century the advancements within the aerospace industry have been extensive. These advancements have come as a direct result of people in the modern world wanting increased performance and speed whilst expecting reduced costs.

These expectations are apparent in both commercial aircraft with longer flights and reduced flight times required while at the same time ensuring flights are economical, and also defence where speed and performance are always looking to be improved upon.

Rolls-Royce, plc. is a company that specialises in producing turbine applications for travel in land, sea and air covering a number of industries from defence to commercial. As a company Rolls-Royce has been at the cutting edge of technology for a number of decades and is now the second largest supplier of aero-engines in the world.

The latest and most advanced engines currently being produced by Rolls-Royce are the Trent series gas turbine engines, such as the Trent XWB (figure 1.1). These Trent engines, as mentioned, are built for efficiency on long haul flights and are referred to as 'bypass' turbine engines.



Figure 1.1: Trent XWB engine (5)

The conflicting issue with these large bypass engines is whilst efficient in terms of fuel consumption, their enormous size leads to an increase in weight of the aircraft and consequently requiring more fuel in order to propel it. This lead to a huge amount of investment into the materials used in the latest Trent engines (figure 1.2), with a number of superalloys and composites being developed to increase efficiency.

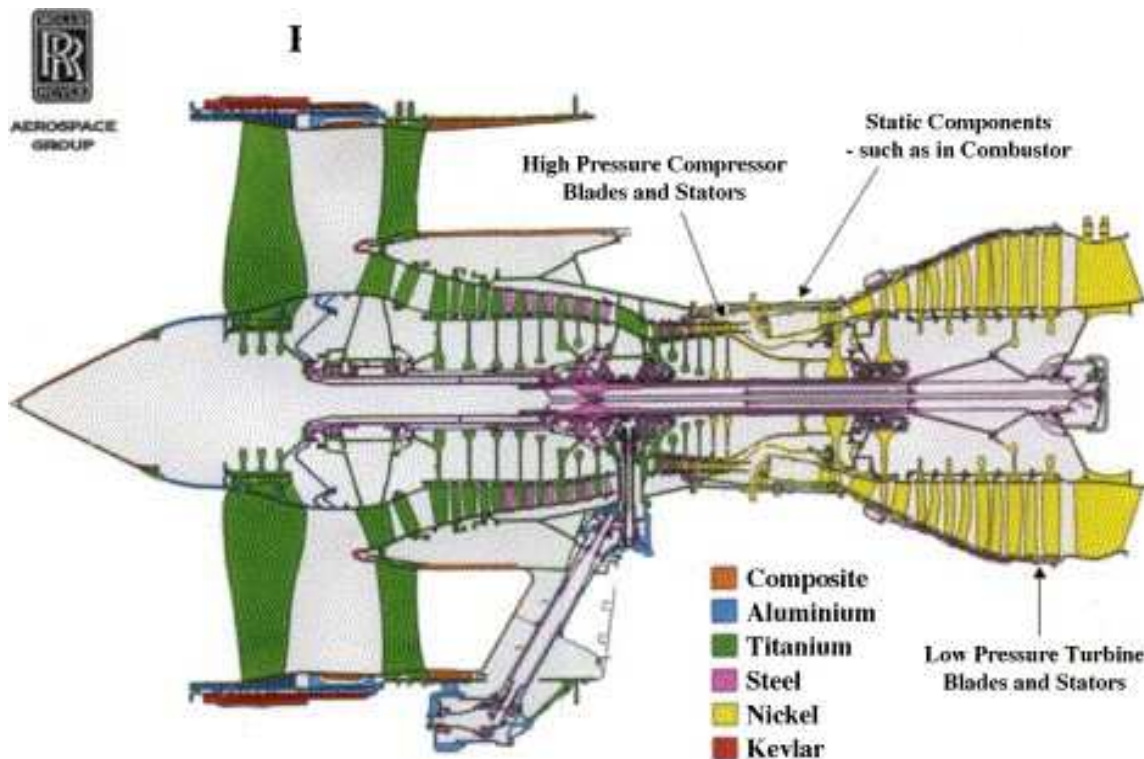


Figure 1.2: Alloys used in various parts of Rolls Royce Trent engine (9)

Common materials in use are nickel alloys for the high temperature sections, composites, steel and aluminium alloys within the casing and also titanium alloys for use in the fan and low pressure compressor regions. Nickel is used despite its reasonably high density, as it is the only alloy that can currently withstand the high temperatures that the high pressure compressor and turbine regions are exposed to whilst still maintaining its mechanical properties and integrity. Titanium, whilst having a very low density and robust mechanical properties at lower temperatures, can be compromised by oxidation at temperatures above 600°C and is therefore not

suitable for use within these high pressure sections, where temperatures can exceed 1100°C [3].

Titanium alloys occupy the greatest weight fraction (over 40%) within the latest Trent engines despite them being of a much lower density. As a result of this much research is currently being undertaken in order to maximise the amount of titanium used within the aerospace industry and producing alloys capable of operating at higher temperatures than is currently possible [3].

1.1 Background

The front of the engine where the fan and compressor zones are located is the largest area of the engine as it has to utilise as much air as possible. The components within these zones are therefore constructed using titanium as opposed to nickel due to its vastly reduced density. The components found within these zones include the blades, disks and also the engine casing. As can be seen in figure 1.1, the compressor and fan blades are located around a central disk. Friction welding is often used to attach these blades to the central disk. Friction welding comes in a number of forms such as friction stir welding (FSW) to join sheets, rotary friction welding (RFW) and also linear friction welding (LFW) which is used to attach the blades to the central disk without the need for mechanical attachment, these components being known as 'BLISKS' (bladed disks) [4]. This development in LFW in particular was a big discovery for the aerospace industry, allowing the production of stronger components with a longer life cycle and also reducing weight. This reduction in weight due to better welding techniques and advancements in materials processing coincided with the turbine engines used by Rolls Royce becoming larger to accommodate the growing demand for aircraft usage.

The latest engine the Trent XWB expected to be released commercially on the Airbus A350 in 2014 has a fan diameter of 118 inches (3m) with a significant part of this being the central disk. The development of future fan disks is expected to exceed the

900mm at current and consequently make it impossible to source these components from forging houses in single pieces. This meant that in order to make the Trent engines even bigger a new method of constructing the fan disks from several parts was required. As the disks were rounded in geometry research was done into a form of friction welding known as Inertia welding (IW). Research suggested that the quality and size of the welds may be very similar to that of the LFW process that had proven to be highly successful. This led researchers to look at (IW) as a way of welding three components of rounded geometries together to form a disk to the size required. The second advantage of this modular design was that with many forging houses able to supply these smaller component parts for the disk it gave Rolls-Royce wider access to the market. The material used within the fan to produce the blades and disk is Titanium due to its excellent mechanical properties at low temperatures (-50-300°C).

1.2 Project aims and objectives

A large amount of research has been undertaken in LFW of titanium alloys which has produced promising results. As LFW and IW have a number of similarities in terms of the processing parameters, and therefore microstructures and mechanical properties they produce within welds. This research will be evaluated along with that of IW which has been rarely researched.

The most common titanium alloys used within the aerospace industry are Ti-6V-4Al (Ti64) and Ti-6Al-2Sn-4Zr-6Mo (Ti6246). Whilst work has been carried out on the IW of Ti6246 and also LFW of Ti64 there is no known work that has been carried out on IW of Ti64. This therefore will be the focus of the study, as Ti6246 is a very expensive alloy and is generally only used within the compressor sections of the engine where performance at high temperature is key. Therefore the use of Ti64 is much more appropriate in this application within the fan. Microstructure analysis and evaluation using SEM and optical microscopy, along with numerous mechanical

tests such as micro-hardness and threshold tests. The presence and size of the Central zone (CZ), Thermo-mechanically affected zone (TMAZ) and the Heat affected zone (HAZ) will be observed, measured and tested for micro-hardness, in both the hoop and transverse directions across the weld. This will allow for the assessment of whether Ti 6-4 is a suitable material to be IW to produce modular fan disks within a gas turbine engine. Along with this it can then be compared to the work done on LFW of Ti-64 and evaluated in conjunction.

CHAPTER 2 METALLURGY OF TITANIUM ALLOYS

2.1 Introduction

This chapter aims to a background into titanium and its alloys, starting with an overview of the various classifications of alloys and processing routes. It then becomes more specific focusing on α - β titanium alloys. Finally the α - β alloy, which this thesis is based upon Ti64, is reviewed and its phase transformations, microstructure and mechanical properties are discussed.

2.2 Classification of Titanium alloys

Titanium is often thought of a single alloy with very specific properties. However, in fact there are a number of different forms of titanium alloys that can be defined. As the alloying elements within Titanium govern its β -transus temperature and therefore phase transformation. The β -transus temperature can be stated as the lowest temperature where 100% β phase is able to be obtained [3]. These elements can be classed as:

- 1) α stabilizers – e.g. oxygen, nitrogen, carbon and aluminium. These form less than four bonds with other atoms which allows them to dissolve in the α phase and increase the β -transus temperature. Oxygen and aluminium are the most common added to titanium increasing the strength with quantities. Although more than 8% aluminium causing a brittle form of alloy.
- 2) β stabilizers – e.g. molybdenum, vanadium, chromium, manganese and nickel. These elements form more than four bonds with other atoms and therefore cause a gradual decrease in β -transus with decreasing (%wt.) until a

compound is formed and a two phase structure results from this. These elements can be divided up into β -isomorphous such as molybdenum and vanadium which exhibit complete solubility with titanium and β -eutectoid such as manganese and chromium which are less soluble and form intermetallic compounds making heat treatment less effective.

- 3) Neutral elements – e.g. silicon, tin and zirconium form four bonds with other atoms and have a negligible effect on the β -transus

This means that three classes of Titanium alloys can be identified [8].

2.2.1 α and near α Titanium alloys

The α titanium alloys contain either or both neutral alloying elements and α stabilisers, whilst the near α alloys contain α stabilising elements along with small amounts of β phase stabilisers lead to an elevation in the β -transus temperature. The alloying elements added within these alloys allow titanium to maintain its HCP structure as the inter-metallic compounds that form as a result i.e. titanium aluminide, possess hexagonal crystals themselves. However the presence of these compounds due to the addition of too much alloying element (i.e. aluminium) can cause weakness within the structure. The near α alloys are more likely to be used in gas turbines due to increased mechanical properties above 400°C. When these alloys are cooled rapidly fine acicular microstructures are produced, where a slower cool results in more plate-like α structures [7, 8, 63 & 64].

2.2.2 α - β Titanium alloys

These alloys contain a mixture of both α and β phases. Examples of this alloy are Ti-64 and Ti-6246 which are very common materials used within the aerospace industry (fan blades and disks) and other high end applications. They possess characteristics of α and β alloys with both good formability and also high strength at room

temperature with moderate strength at high temperatures. This is due to the elements being used strengthening the α phase with 4-6% β (8), to retain large amounts of β phase when the alloy is quenched. In order to form α - β alloys with the required mechanical properties heat treatment is carried out to manipulate the microstructure and state of the β phase. The disadvantage to these alloys is that they can be difficult to weld. Heat treatment and control of processes allows these alloys to be designed to suit many needs, which is why they are so desirable. Fast cooling forms equiaxed structures which make it difficult for fatigue cracks to nucleate. If the cooling is from above the β transus then acicular α structures form and although cracks may nucleate with greater ease, the growth rate is very slow. These alloys also have good fracture toughness [7, 63 & 64].

2.2.3 β Titanium alloys

These alloys generally contain large amounts of transition metals i.e. Vanadium, yttrium and molybdenum amongst others which can be stated as β stabilizers. They lower the β -transformation temperature and stabilise the β phase. These elements are split into two groups β -isomorphous and elements forming eucotoid systems. As a rule one β -isomorphous element will be added to the titanium along with one eucotoid element. The isomorphous such as Molybdenum and Vanadium prevent the formation of inter-metallic compounds and when mixed with the eucotoid elements which raise the eutectoid temperature form alloys with minimal inter-metallic's at high temperatures [3]. These β alloys have excellent formability qualities, although as a result of their BCC structure are susceptible to brittle-ductile transformation making them poor alloys for use at low temperatures and unsuitable for use within the fan of a turbine engine [7, 63].

2.3 Processing methods and heat treatment

Titanium and its alloys are the subject of various processing methods that enable us to produce a material with highly desirable mechanical properties from a very basic bauxite ore. Once a titanium bar, billet or sheet has been formed heat treatment is used to finely define its mechanical properties and remove any apparent residual stresses.

2.3.1 Titanium processing methods

The processing of titanium from the very beginning where it is extracted from its ore to the end product can be explained through four main stages:

- 1) Rutile reduction to titanium sponge
- 2) Melting of the sponge to produce an ingot
- 3) Primary fabrication to produce mill products
- 4) Secondary fabrication to produce finished shapes

Once these products have been formed they must undergo specific heat treatment processes in order to produce products with the required properties for the application.

The third stage in the process primary fabrication where mill products such as bars, billets and sheets are produced is considerably more important than secondary fabrication in terms of its influence on the resultant microstructure and hence mechanical properties [3, 10]. The temperature at which the sponge is melted to produce ingots is often below the β -transus temperature enabling a very fine microstructure to be formed. The secondary fabrication then allows this microstructure to be adjusted to meet specific mechanical property requirements.

These secondary processes include: forging, machining, milling and joining. Forging is the most popular of these processes and a high temperature in operation within

the α - β region will lead to a greater amount of β being available. When α - β alloys are quenched above β -transus an acicular or Widmanstatten microstructure will result [3, 10, 64].

2.3.2 Heat treatment

Heat treatment is a method employed to ‘personalise’ the mechanical properties of titanium alloys as they generally do not have the required mechanical properties in their processed condition. Various methods of heat treatment can be used whereby the material is carefully heated and cooled under very precise environmental conditions in order to alter the physical and mechanical properties of the material. The common methods of heat treatment in titanium and reasons they are employed are [3, 42]:

- 1) Reduce residual stresses developed during fabrication (**stress relieving**)
- 2) produce an optimum combination of ductility, machinability, and dimensional and structural stability (**annealing**)
- 3) increase strength (**solution treating and aging**)
- 4) optimize properties such as fracture toughness and fatigue strength

2.4 α - β Titanium alloys

The α - β titanium alloys make up the largest group of commercially available alloys. They have a huge market within the aerospace sector. This is due to their desirable properties of having a very high strength/weight ratio hence allowing for more economic aircraft during flight whilst maintaining performance. They have excellent mechanical properties at room and low temperatures which are vital within the large fan. Finally they exhibit very good corrosion resistance and therefore maintenance

time and costs of titanium parts are kept to a minimum. The two most common commercially available α - β titanium alloys and ones very prevalent within aerospace are Ti64 and Ti6246.

The reason for these properties is related to the microstructures of these alloys and the phases present and phase transformations that occur upon processing [8].

2.4.1 Phases in α - β titanium alloys

1) Equilibrium phases

These phases occur when a system is in steady state. Phase diagrams may be used to predict their compositions at certain temperatures. There are three main equilibrium phases.

α Phase: This possesses a HCP structure and can be classified as primary α (α_p) or secondary α (α_s). The grain structure of α_p varies and can be equiaxed, lamellar or mixed. Lamellar structures are apparent if the alloy is cooled from above the β transus. The alloys can be heat treated to try and obtain a microstructure with more equiaxed grains. This is done by processing below the β transus. α_s also has varying microstructure and is apparent within an alloy if cooled from below the β transus [8].

α_2 Phase: Again as a HCP structure and chemical formula Ti_3X , such as Ti_3Al . This forms when temperature are high during ageing of alloys with high amounts of α stabilizers being present. Diffusionless transformations generally occur in these phases and can lead to non-equilibrium phases, martensitic non-equilibrium phases are present in some titanium alloys. Titanium alloys with high concentrations of α phase are generally used for increased temperature applications where corrosion resistance is not of as much significance [8, 15].

β Phase: The β phase possesses a BCC structure and is far more stable at high temperatures above the β transus than a HCP structure. This is due to it having more space in its crystal structure. Alloys heavily concentrated with β phase allow for the alloy's mechanical properties to be improved through heat treatment, mainly solution treating and ageing which improves strength [8, 63].

2) Non-equilibrium phase

When cooled rapidly from above the β transus temperature, this can be seen as a transformation from β phase to a martensitic form. Martensites vary in their crystal structures.

Martensitic α' : This is a supersaturated α phase with the same crystal structure, therefore making it very difficult to identify α' from an acicular α . Titanium alloys containing α' have increased hardness values due to the very fine microstructure of the α' phases. The microstructure of these α' phases can be classified as either lath martensite or acicular martensite [8].

Martensitic α'' : This forms as an orthorhombic structure and its formation is dependent upon the amount of β stabilizers that are present within the β phase. Some elements such as Nb, Mo and W allow for the transformation of α' to α'' whereas the presence of V as in Ti64 can prevent this transformation, therefore α'' is often not present within this alloy. The hardness of these α'' when they are present within Ti64 is very low [8].

2.4.2 Phase transformations in α - β titanium alloys

Phase transformations have a significant influence on the resultant mechanical properties of α - β titanium alloys and therefore it is important to consider them. The two transformations that are considered to be the most important are firstly diffusional transformations ($\beta \rightarrow \alpha$) and diffusionless ($\beta \rightarrow$ martensitic α' or α'').

Diffusional transformation ($\beta \rightarrow \alpha$): This involves the diffusional nucleation and growth of the α phase. These α nucleation may be on the grain boundary or within the grains themselves starting at the grain boundaries. Cooling from above the β transus temperature α tends to nucleate at the β grain boundaries. As this cooling continues, α plates nucleate and grow into the grains parallel to each other either from the formed α grain boundaries or the original β grain boundaries. The parallel growth of these α plates are referred to what eventually become α colonies within a β phase. The main determiner of the nature of these α colonies is the cooling rate of the alloy. If cooled very slowly and the β grains are very coarse then these colonies can grow to be quite long (hundreds of microns). These large length colonies are then referred to as lamella and the microstructure characterised as being of a lamellar nature. In contrast if the alloy is cooled rapidly then the β grains will be much smaller and contain far fewer α plates. These microstructures are described as basket-weave or sometimes Widmanstätten in appearance [8].

Martensitic transformation ($\beta \rightarrow \alpha'/\alpha''$): The α' and α'' phases can be formed during rapidly cooling due to the martensite being able to form.

2.4.3 Microstrcuture of a $\alpha - \beta$ Titanium alloy

As mentioned previously the processing of titanium alloys is what foremost determines their resultant microstructures. The processing routes can be either wrought, cast or powder metallurgy with consequent heat treatment methods also having an effect [3]. These microstructures within α - β titanium alloys can be categorised into three main groups: lamellar, bi-modal and also equiaxed.

Lamellar: These microstructures are formed from homogenization treatment in the β phase. This is governed by the cooling rate as it determines the length of the α colonies and resultant α lamellae growing from the β grain boundaries [8].

Bi-modal: These microstructures contain both equiaxed α grains and transformed β and are formed from within a $\alpha + \beta$ phase. Again homogenization treatment is used in operation within the β phase field then deformation and recrystallisation in the $\alpha+\beta$ field. As with lamellar structures the cooling rate is very important during recrystallisation as it determines the size of the primary α , α lamellae and transformed β grains. Coarse acicular α grains are also common in this microstructure [8].

Equiaxed: These microstructures consist of primarily equiaxed α grains with intergranular β phases. The process that produces this type of microstructure is almost identical to that of the bi-modal structure. The only difference is the cooling rate during recrysallisation and a reduced annealing temperature. If the rate is low enough then primary α will grow and no α lamellae will be present within the grains [8]. These equiaxed grains can be very small due to the grain boundaries being pinned as a result of the low temperatures. This type of annealing within the $\alpha + \beta$ phase can also be referred to as mill annealing [3, 10,11].

2.5 Ti-6Al-4V

Ti-6Al-4V otherwise referred to by its tradename, Ti-64, is an α - β alloy widely used within the aerospace industry and one which will be studied within this thesis. The main stabilising element within this alloy is Aluminium (Al) which increases the β -transus temperature and also a slight increase in strength. Another element present within Ti64 is vanadium (V), which can be classified as a β -isomorphous stabilizer. V compared to other β -isomorphous stabilizers such as molybdenum is quite weak however.

2.5.1 Phase transformations in Ti64

Phase diagrams may be used to calculate the composition of Ti64 and also the amount of α and β phase present. Figure 2.1 below shows the percentage of each phase present within Ti64 compared with temperature (a) and also the concentrations of Al and V in each phase (b).

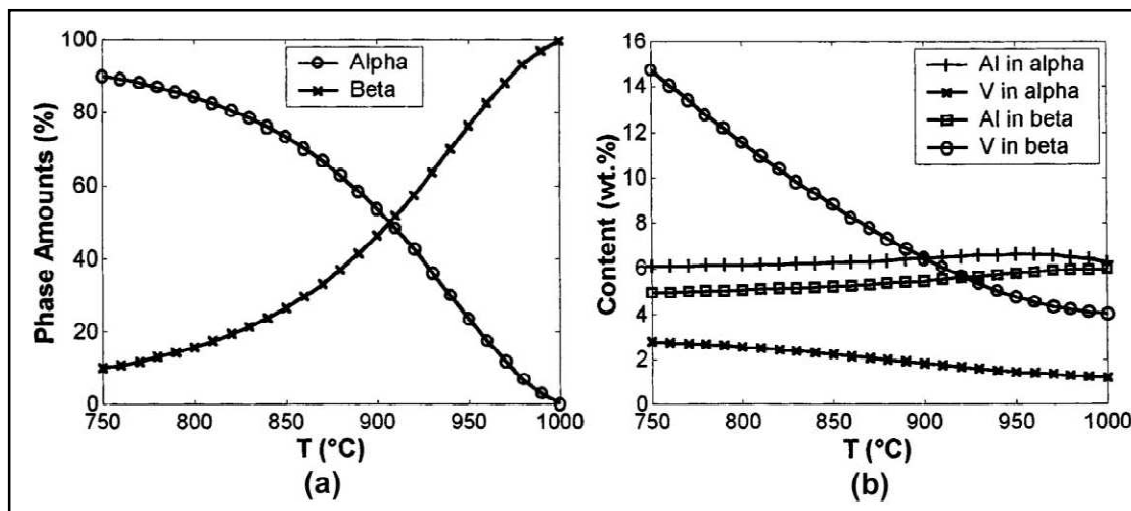


Figure 2.1: (a) Volume fraction of α and β phases vs. temperature in a Ti 6-4 alloy; (b) Concentrations of Al and V in each phase vs. temperature (8, 49).

This diagram correlates with what is known of the β -transus temperature 995°C with 100% β present at 1000°C (50). Figure 2.1b clearly shows approximately 4% Vanadium (V) and 6% Aluminium (Al) within the β phase at 1000°C. During the α - β transformation Al begins to occupy the α phase and V leaves the α phase. Therefore the amount of V in the β phase increases with the formation of α precipitates [8].

The formation and appearance of microstructures is said by some to be most closely controlled by cooling rate after heat treatment. This can be seen in figure 2.2.

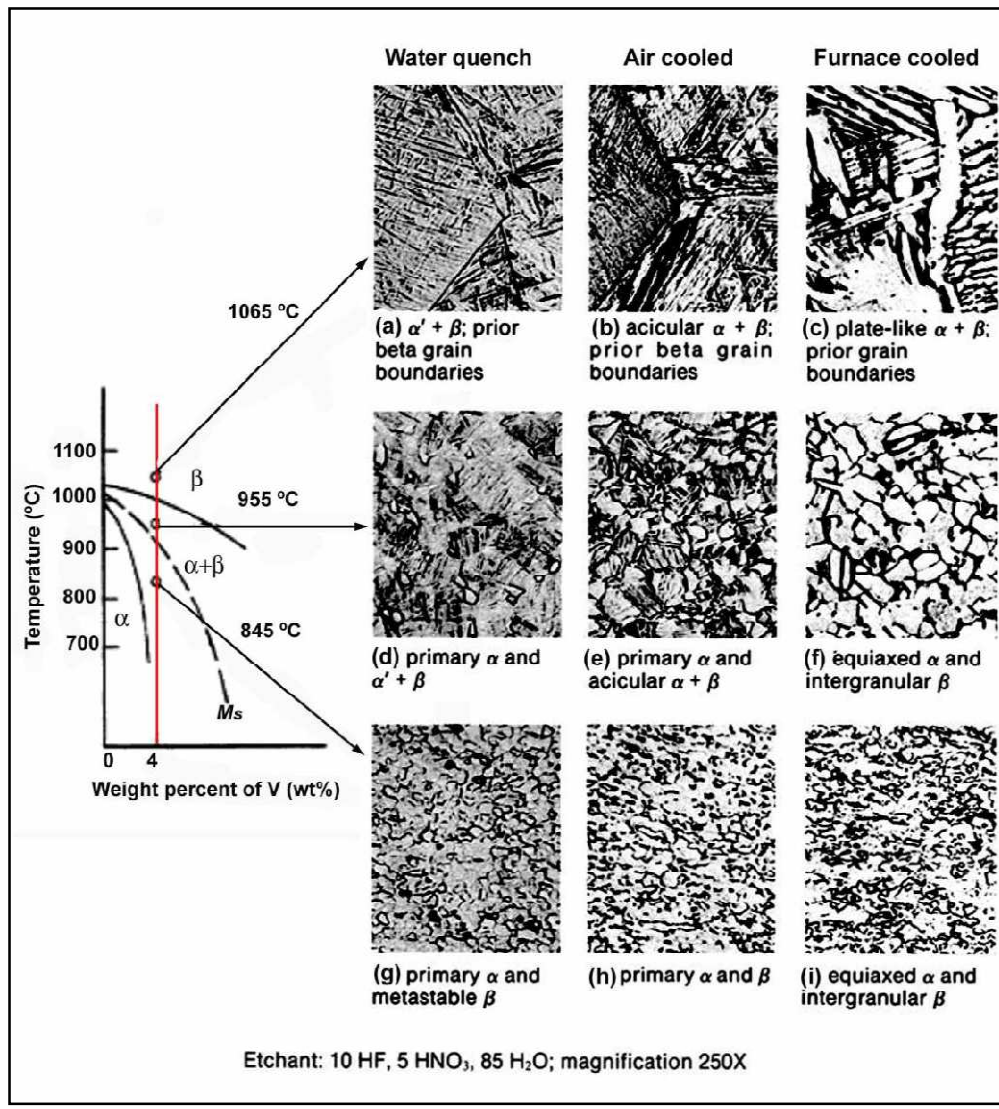


Figure 2.2: Ti-64 phase diagram and the microstructures obtained under different annealing temperatures and cooling rates (8, 50).

Slow cooling results in parallel α plates in a β matrix. When this cooling rate is increased there are more α plates that nucleate although their size is reduced. There is also an increase in acicular α nucleation inside β grains (basket-weave structure) as shown in 2.2 (b). If this cooling rate is increased further still as occurs when water quenched, a martensitic transformation will occur figure 2.2 (d) and (e) again show the effects of cooling rate on the microstructure. When the Ti alloy is cooled within the furnace (slow cooling rate) an equiaxed microstructure is formed with the presence of intergranular β . Where when this cooling rate is increased in (d) a bimodal structure is formed. This is most likely due to the faster cooling preventing the growth of the α phases.

The rapid cooling of Ti leads to the breakdown of β as the martensite is transformed. The amount of martensite formed as a result of this fast quench depends upon what elements are present within the β phase. A high % of V often leads to a low fraction of V proportionally in the β phase. When water quenched from above the β -transus temperature, martensitic α' is observed .

This shows how important not only the heat treatment of these Ti alloys is but also the quenching and cooling post treatment. This has a big effect on the resultant microstructures and therefore mechanical properties obtained. As discussed in the introduction a very common usage of Ti alloys within the Aerospace sector is within the fan including various blades and disks. Properties required for these applications include high fracture toughness and various fatigue resisting properties prohibiting crack growth. Generally a fully lamellar structure is optimal for high fracture toughness and reducing crack growth rates. Whilst fine equiaxed structures are preferable for high hardness values and prevention of crack initiation [8, 51].

2.6 Mechanical behaviour of Titanium alloys

2.6.1 Fatigue

As the majority of failures that occur within the aerospace industry are due to fatigue failures the analysis of this is vitally important. Fatigue can be explained by defining it as the progressive and localised structural damage resulting from variable strains at maximum stresses [14]. The process of materials failing as a result of fatigue can fundamentally be classified into five stages [15].

- 1) Plastic deformation before crack initiation
- 2) Initiation of microcracks
- 3) Propagation of cracks to form macrocracks
- 4) Propagation of macrocracks
- 5) Failure

The fatigue properties of titanium can be analysed in terms of its observed microstructure. In the α - β alloys i.e. Ti64 surface microcracking was found within the α phase and interface cracking between the α and transformed β [16]. Critical stress values were found to be important to the initiation of these cracks. Above these values cracks initiated early in the cycles, where below this the cracks initiated much later at the α - β interface. Bowen and Stubbington [17] found that within Ti64 fatigue cracks were found to initiate at various places within the microstructure. These were across α grains and across and or along α - β interfaces. The crack growth across grains was a direct result of the samples being exposed to high stresses, with low stresses leading towards interface initiation. This may be down to the larger α grains being susceptible to these crack initiations [17].

The microstructure was also found to have a large influence on the fatigue crack behaviour within titanium. Alloys with coarse grains and basket-weave structures resist crack propagation, whereas fine grains resist crack initiation [11]. The best combination of microstructure for α - β alloys is therefore one possessing a fine grain

size [10]. Acicular α grains also show improved resistance to crack growth initiation, as oppose large equiaxed grains [18].

One of the difficulties with designing against these fatigue cracks is the contradiction in microstructures required to design against crack initiation and crack growth. An α - β microstructure with very fine α grains size and minimal transformed β offers excellent resistance to crack initiation. Whereas to ensure good resistance to the propagation of these cracks much transformed β is favoured.

2.6.1.1 Mechanical threshold

Mechanical threshold testing is a form of fatigue testing. The fatigue threshold is calculated by determining the nominal stress value that is required to cause a sample to fail in terms of cycles. This data is then represented in the form of S-N curves where stress (S) is plotted against the number of cycles to failure (N). The mechanical threshold can be defined as the maximum stress that a material can endure without experiencing failure. As the amount of load naturally has a large effect on how many cycles the material is able to endure, the tests must be conducted at a uniform load (amplitude). This amplitude is referred to as the R ratio. This can be defined as the minimum peak stress over the maximum peak stress ($R = \sigma_{\min}/\sigma_{\max}$). A lower R Ratio represents a greater difference between the minimum and maximum amount of stress being exerted on a sample. Therefore, a greater stress range and lower R ratio relates to a shorter fatigue life [13].

The shape of these graphs can be quite sharp in many alloys, meaning crack growth via fatigue occurs quickly as the amount of stress is increased. However, in titanium alloys the shape tends to be far more gentle, becoming flat at around 10^7 cycles. The samples tested using these tests can be either smooth or notched which has an effect on the fatigue capability of the sample[11].

In Ti64 small fatigue threshold cracks have been found to grow at lower stresses than larger cracks [19, 20]. Higher stress ratios were found to produce lower mechanical threshold values as a result of more rapid crack growth rates [21].

2.6.1.2 Low cycle fatigue (LCF)

Another fatigue property essential to turbine engines is low cycle fatigue (LCF). This is particularly important as it refers to the number of cycles (take-offs) that the component parts of the engine can be exposed to before failure. Typically in LCF this is a maximum of 10^4 cycles. LCF involves stresses at high amplitudes and low frequency, eventually causing it to undergo permanent plastic deformation and fail.

The microstructure and morphology of the alloys is what determines its fatigue properties. In titanium, crack initiation occurs quite readily, although its total fatigue life is long. This means that the crack propagation properties within the alloy are what determines LCF, with high amplitude loads contributed to this early crack initiation [22]. LCF can be linked to fracture toughness in respect of crack propagation as microstructures that result in low growth rate also produce high fracture toughness. Crack initiation at the surface in Ti64 has been observed generally along slip bands in the α phase and also between α and transformed β [16]. However as mentioned previous work carried out by Stubbington and Bowen [17] found that these cracks could be initiated at several locations within the microstructure of Ti64. They also found that grain size was important in crack initiation with larger α grains being more susceptible to crack initiation at high stresses than smaller ones [17]. The issue in α - β titanium alloys is that fine microstructures are required to prevent crack initiation but coarse basket-weave microstructures are needed to hinder propagation. Therefore a combination of fine α grains and coarser β grains is the most favourable. These fine grains reduce the slip paths where the transformed β reduces the number of α - β interfaces and

therefore propagation. Acicular α was also found to reduce crack propagation rates by making the path for crack growth challenging [17].

2.6.1.3 Fatigue crack propagation

Fatigue crack propagation is often analysed to determine how a pre-existing crack will grow and develop within a material. The waveforms used will again be cyclic and the crack will be measured in terms of its growth rate/cycle at a specified stress intensity.

As the prevention of cracks at some stage during a components life cycle is impossible, it is therefore essential that much research is carried out as to how quickly these cracks will grow and at what stage they become a risk to the structural integrity.

The microstructure that favours the prevention of crack propagation is the same as that desirable within LCF, which was discussed in the section previous.

2.6.2 Tensile strength

Tensile strength is the maximum amount of stress (MPa) a particular material can be subjected to by stretching or elongating it before it fails. Tensile tests are carried out to measure the stress versus the strain that a material is being subjected to, allowing for the plotting of a stress-strain curve. The peak of the curve is stated as reaching the ultimate tensile strength of a material. This is then followed by fracture.

Titanium alloys and in particular Ti64 exhibit reasonably high tensile strength values, although Ti6246 is considerably higher. Donachie [10] found the tensile strength of Ti6246 to range from (938-1027 MPa). Similar results were found by Pardhi [3] who also carried out tensile testing on Ti6246 that had been inertia welded. He tested over the temperature range 27-450°C with tensile strengths of 1126 MPa being

observed at room temperature, dropping to 861 MPa at 450°C. This decrease in tensile strength with increasing temperature is typical of alloys.

2.6.3 Fracture toughness

This can be described as the ability of a material possessing a crack to resist fracture. The critical value is known as the stress intensity factor (K_{IC}) and defines the critical stress at which a crack will begin to propagate. The value of K_{IC} is dependent upon the crack orientation within the material and the corresponding direction of the stress being applied in correlation to it. This property can be closely related to the tensile strength and also fatigue failure, with the critical crack size for crack growth being paramount to these mechanical properties also [10].

Fracture toughness with titanium alloys is very variable and closely related to alloy composition and microstructure [10]. High fracture toughness values, whilst being highly sought after within aerospace applications, must be carefully considered. This is due to many other mechanical properties mainly yield strength, having a negative correlation with increasing fracture toughness values. Donachie [10] carried out much research into this particular issue. He found that the fracture toughness (44-66 MPa \sqrt{m}) of Ti64 had double the fracture toughness (22-23 MPa \sqrt{m}) of Ti6246. He also discovered that the type of α present within these alloys was significant. The values stated were for mainly equiaxed α morphologies, which compared to β transformation morphologies were considerably lower in fracture toughness, with the K_{IC} within the β transformation structures being double. The conclusion from work on Ti-64 and Ti-6246 regarding K_{IC} is that for optimum balance of properties a microstructure containing transformed β to create a challenging path for crack growth. While to maintain strength as much as much primary α and acicular α was also desirable [3]. The areas at grains boundaries are most susceptible to these cracks beginning to propagate from microcracks to macrocracks.

CHAPTER 3 INERTIA WELDING AND ITS APPLICATION IN TITANIUM ALLOYS

3.1 Introduction

Many welding techniques involved in engineering can lead to areas of stress concentration and therefore mechanical vulnerability within a material. Within the aerospace industry common forms of these welding techniques are Tungsten Inert Gas (TIG) welding and also Electron Beam Welding (EBW). These increases in stress concentrations, known as residual stresses, mean that even the most sought after alloys are at risk of fracture and failure. A class of welding processes that has been found to alleviate these weaknesses over the past couple of decades is friction welding.

3.2 Friction welding

This form of welding employs the forces of friction to generate heat at two component interfaces in motion. Lateral force is used to drive the two interfaces into contact with each other. The combination of heat and opposing forces of the two interfaces causes the two component pieces to become plastic. Once plastic the two components begin to fuse and eventually once motion has ceased they will become one component part as the materials cool.

As a result of the two components joining in a solid state the contaminants and oxides are virtually non-existent forming a near perfect joint. This lack of melting within the process also allows for dissimilar materials to be joined together [24]. The main advantage of these processes is that they work below the melting point of the

material causing plasticity but not melting of the components. This leads to the formation of more desirable microstructures within the weld region.

Within friction welding there are a large number of variations that have been developed.

Linear friction welding (LFW) – involves heat generation by creating friction between two surfaces by laterally forcing one component against the other which is stationary in a reciprocating motion. This creates large amounts of friction over a very small area and causes the two interfaces to become plastic. As the reciprocating component is forced against the static component, the plastic region is expelled from the contact interface as ‘flash’. The axial forces are slowly removed and the reciprocation of the component halted gradually, bringing the components into alignment, causing them to fuse as the temperature drops and the interface returns to a solid state forming a single solid component [26]. The main use of LFW is in joining the blades to the central disks in order to create a bladed disk (‘Blisk’). This reduces weight within the engine due to a smaller weld joint being required, along with improving mechanical and metallurgical properties as a result of smaller forgings being possible.

Rotary friction welding – can be split up into two very similar welding procedures Circular Friction Welding (CFW) and Inertia Friction welding (IFW). The process for the two is very similar. In CFW a component is rotated against a static component under axial force. This leads to the material in the weld zone becoming plastic as a result of the friction generated heat. Any contamination, like LFW, is removed via flash as the material is forced out of the weld zone due to the forces squeezing the components together. The rotation is then halted when enough material has been removed, with axial forces remaining until a solid component is formed [3].

IFW is very similar to this but with slight variations. The rotating component is attached to a flywheel, which is then rotated to a specific speed creating kinetic

energy in the flywheel. As the two components are brought together the flywheel rotation is stopped while the axial force remains. The rotating component is slowed down by the friction created at the interface between the opposing components. This again generates heat causing the materials to become plastic and the rotating component eventually comes to a stop as the energy is lost in the form of frictional heat, creating a single solid component on cooling. IFW is generally preferred to CFW in the aerospace industry due to its smaller weld region, due to shorter weld time [3, 25].

3.3 Inertia welding

3.3.1 Stages of Inertia welding

The IFW process can be split up into three main stages [27]:

- 1) **The initial stage** - The two components come into contact. The kinetic energy that was generated as a result of the high rpm of the flywheel is dissipated via heat conduction through friction at the component interface. This causes a rapid increase in temperature and the components become plastic.
- 2) **The intermediate stage** - The pressure being applied at the interface causes the now plastic material to be expelled from the weld region in the form of flash. The release of this material consequently leads to the components reducing in length (upset).
- 3) **The consolidation stage** - When the required upset is reached and rotation stops as a result of all of the kinetic energy being dissipated from the flywheel via frictional heat. The material begins to cool rapidly while axial pressure is maintained.

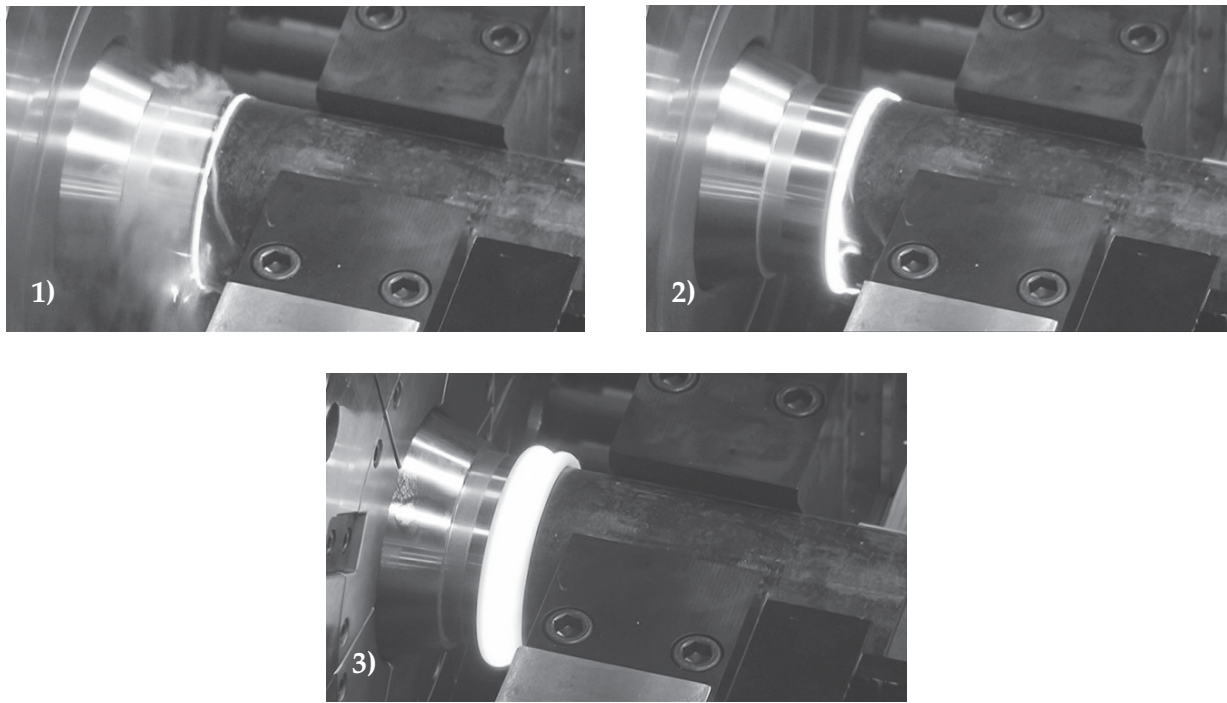


Figure 3.1: Inertia welding process showing 1) Initial Phase, 2) Intermediate Phase 3) Consolidation Phase
 (Courtesy of Manufacturing Technology, Inc [70])

3.3.2 Process variables

IFW is relatively simple compared to many of the other friction welding processes. This is due to there being few parameters within the process that are required to be controlled. The process parameters within IFW are listed below [27]:

- 1) **Moment of inertia (I)** – resistance of the flywheel to rotation.
- 2) **Flywheel rotational speed (N)** – measured in rpm (revolutions per minute)
- 3) **Axial pressure (P)** – pressure under which the two components are forced together via the drive motor

The moment of inertia and flywheel rotational speed determine the total amount of kinetic energy that is available at the interface, where the axial pressure determines the total weld time of the process.

3.4 Inertia welding of Titanium alloys

The amount of work that has gone into the inertia welding of titanium alloys is relatively low, especially that involving friction welding and more specifically inertia friction welding. The microstructures and resultant mechanical properties are fundamentally dependent on the prior parent material that is being welded together.

3.4.1 The weld region

During the inertia welding process of a similar but different titanium alloy (Ti6246), specific zones are formed at the weld which gives friction welding its identity. These weld zones starting from the initial contact of the two parent materials and working outwards back into the parent material are the Central Weld Zone (CWZ), Thermomechanically Affected Zone (TMAZ) and also the Heat Affected Zone (HAZ) before reaching the pre-weld parent material.

3.4.1.1 The CWZ in Inertia welding

Work done by Pardhi, 2010, looked more specifically at each of the weld zones and microstructures present in inertia welded Ti6246. The grains were found to be very fine equixed β grains with needle-like martensitic α . The reason for this microstructure is the transformation of α to β due to the huge increase in temperature at the weld interface (above the β -transus temperature) [44]. The appearance of this transformed microstructure is then governed by the cooling conditions once the inertia welding process has ceased. The needle-like martensitic α is formed directly as a result of very rapid cooling. The size and orientation of these α plates is determined by this cooling rate. The reason for the very fine grain size within this region is due to the temperatures reached during the inertia welding process exceeding that of the β -transus temperature resulting in recrystallisation [3, 44].

The CWZ in LFW of Ti64 was measured to be approximately $100\mu\text{m}$. There are often very fine acicular features observed when Ti-64 is friction welded which was observed by Yina (2013) and this may be a difference between the microstructures of Ti64 and Ti6246, due to the variation in the welding process [8].

3.4.1.2 The TMAZ in Inertia welding

The structure observed within the TMAZ is very distinct and can be described as deformed β grains orientated radially away from the CWZ and gives the impression of material flow. Much like the CWZ the TMAZ contains mainly martensitic α precipitates without the recrystallisation. This zone however, is generally much wider than that of the CWZ most likely due to the less rapid cooling within this region (8). The inner TMAZ has many similar features to that of the CWZ such as fine grain size and acicular α . With distance from the weld interface features present within the parent material become more apparent, mainly the coarser α plates, although these are only partially dissolved. In some literature these partially dissolved α plates can be coined “phantom α phases”. The reason for this partial precipitation of α precipitates is that the temperatures in which this region is exposed to are around the β -transus temperature and for only a very short time preventing complete homogenisation. The primary reason for this incomplete homogenisation is that the β stabilizers do not have sufficient time to diffuse into the primary α grains (45). For this reason the TMAZ is not fully deformed by the process and still retains some characteristics of the parent material [3, 8].

3.4.1.3 The HAZ in inertia welding

The reason for the separation of the HAZ into two separate zones unlike other friction welding processes is the rapid induction of heat into the material and then a sudden removal of energy input. This leads to a high impact of heat close to the weld interface that quickly reduces as you move away from this interface. This results in numerous very small zones not dissimilar to LFW and the need for the characterisation of two separate zones. Whereas in comparison to this work by Pardhi (2010), Yina (2013) suggests that Ti-64 after LFW has two separate TMAZ zones and the HAZ is often virtually non-existent after the friction welding of Ti-64. [3, 8].

The inner HAZ is still affected by the heat generated at the weld interface and as result martensitic α can be observed along with phantom α . As you move into the outer HAZ the formation of these α precipitates becomes less apparent and the microstructure becomes much more similar to that of the parent material. This zone has been found to consist primarily of the coarse α platelets of the parent microstructure along with the presence of secondary α [3].

These secondary α platelets are formed during the ageing of Titanium alloys and dissolve when exposed to high temperatures and then a subsequent very rapid cooling. This is the reason for the lack of this platelets within the inner zones and an increase in number as you head away from the weld interface throughout the HAZ [3].

3.4.1.4 Weld width in inertia welding

Pardhi (2010) carried out work into the effects of welding parameters on the width of weld zone. He defined the weld width as the distance between the weld interface and outermost edge of the inner HAZ. An increase in axial pressure reduced the width of the HAZ due to an increase in upset, i.e. more material is expelled from the weld in the form of flash due to the increase in pressure. An increase in rotational speed had the opposite effect however. This increase in speed, lead to much more energy being created when two components came into contact. This lead to heat dissipating through the material further and therefore increasing the size of the weld zone. This heat dissipation was a result of the longer welding time due to the heat taking longer to be consumed by the flywheel, resulting in the weld region being fluid for longer [3, 46].

It should also be noted that the shape of the weld region within inertia welding is very distinct. Due to the rotational nature of the two components coming together and there being a bigger concentration of heat at the centre compared to that at the edge of the components where heat is much faster dissipated. The inertia weld appears as a curve, with a noticeably thicker weld zone at the surface of the material than the centre. This is compared to LFW where the weld shape is fairly regular all the way across due to linear action as opposed to rotary [3, 8].

3.4.2 Mechanical properties of Inertia welded Titanium alloys

3.4.2.1 Micro-hardness

Work done by Pardhi [3] found that within IW of Ti6246 the hardness at the weld centre (460 Hv), was much higher than that of the parent material with a steady decline through the TMAZ and HAZ. This was thought to be a direct result of grain refinement and phase transformation within the weld region. However, there was also an observed slight decrease compared to the rest of the weld at the very centre of this zone due to the formation of oxides and appearance of porosity. This was also found by Wanjara and Jahazi [12] who carried out work on friction welding of Ti64, although this was not apparent in Yina's work on LFW of Ti64 [8]. The orientation of the weld was found to affect the hardness values. Those measured from the side of the weld showed that there was a higher peak hardness region at the inner (ID) and outer diameter (OD) due to the curve of the weld region.. The outer HAZ (340Hv) was found to have a lower hardness than the parent material (380Hv) due to the absence of secondary α . The high hardness at the CZ and increase in amount of martensitic α was found to correlate, areas with increased β fields caused the material to be softer. Weld joints formed when processing conditions lead to poor consolidation with the presence of oxides and porosity also reducing hardness values.

Work carried out by Yina (2013) found a CWZ much harder than that of the HAZ and parent. However, the LFW process of Ti64 produced reduced hardness values in the CWZ (360-370 Hv), HAZ 300-310 Hv) and in the parent material (320-330 Hv). Yina's results on Ti-64 are similar to those of Wanjara & Jahazi (2005) and Attallah et al (2009) [47, 48].

For a more detailed account of micro-hardness profiles in inertia welds see work produced by Pardhi (2010), who directly assessed weld size and grain size and the associated hardness values in each zone along with in depth assessments of welding parameters [3].

3.4.2.2 Tensile properties

Unlike many other welding processes the advantage of friction welding is that a weld zone is created far superior in terms of properties than those of the parent material. Work done by Pardhi (2010) proved this in inertia welded Ti6246 at both room temperature and elevated temperatures of 400°C [3]. Although it can be said that the weld zone is superior in tensile strength than that of the parent material in Ti6246, to actually examine the tensile strength of the weld itself is very difficult. This is due to the nature of the test and that the specimen will always fail well into the parent material away from the weld zone. The most likely explanation for the increased strength in tension within the weld is the very refined microstructure due to re-crystallisation and fine α precipitates.

3.4.2.3 Fatigue and crack propagation

Fatigue behaviour and crack growth within titanium alloys is a very important area to explore due to the cyclic nature that the material is subjected to within aerospace applications. Pardhi (2010) conducted some work on the crack growth behaviour of Ti6246 at varying stress ratios and temperatures. He found that lower stress ratios of 0.01 related to slower crack growth rates compared to those of higher stress ratios of 0.4-0.8. The crack growth rate was also observed to be faster at higher temperatures.

CHAPTER 4 EXPERIMENTAL AND ANALYTICAL METHODS

4.1 Materials

The samples used are taken from the inertia welding of two Ti64 rings. These Ti64 welds were obtained from Rolls-Royce, plc with the chemical composition of the material shown in Table 4.1.

Al (wt. %)	V (wt. %)	O (wt. %)	Fe (wt. %)	C (wt. %)	N2 (wt. %)	H2 (wt. %)	Y (wt. %)	B (wt. %)	Ti (wt. %)
5.5- 6.75	3.5-4.5	0.17- 0.23	0.30 Max	0.1 Max	0.03 Max	0.01 Max	0.1 Max	0.001 Max	remainder

Table 4.1 - Chemical composition of commercial Ti64 as per Rolls-Royce, plc

4.2 Welding of the materials

Once the welding process was completed and the flash removed a welded ring was produced of diameter 180 mm, length 125 mm and wall thickness 20 mm. The wall thickness of the weld was 9mm as some material was removed during machining of the flash surrounding the weld.

There were two welds produced for the thesis via this inertia welding process. The inertia values for both were constant. However, varying energy input and pressures were used as shown in Table 4.2.

Weld PDRIW119-	Energy Density (MW/m ²)	Initial Angular Speed (RPM)	Pressure (MPa)	Inertia (Kg/m ²)	Weld Area (mm ²)	Cold Upset (mm)
02	37.70	807.35	69.00	56.30	5325.30	5.41
03	30.60	728.02	137.90	56.30	5344.70	4.88

Table 4.2- Inertia welding parameters used

4.3 Post weld heat treatment (PWHT)

On completion of the welding process, both welds were exposed to heat treatment within a furnace heated to 600°C. This heat treatment lasted for one hour before the welds were removed and cooled in air. The exact details of this PWHT procedure were not disclosed by Rolls-Royce, plc.

4.4 Sample preparation

Samples used for the various types of mechanical testing were extracted from the welds in the axial direction as shown in figures 4.1 and 4.2 using Electrical Discharge Machining (EDM).

The samples used for the microstructure analysis and mechanical threshold testing were taken from the areas where material was spare within these welds again using EDM.

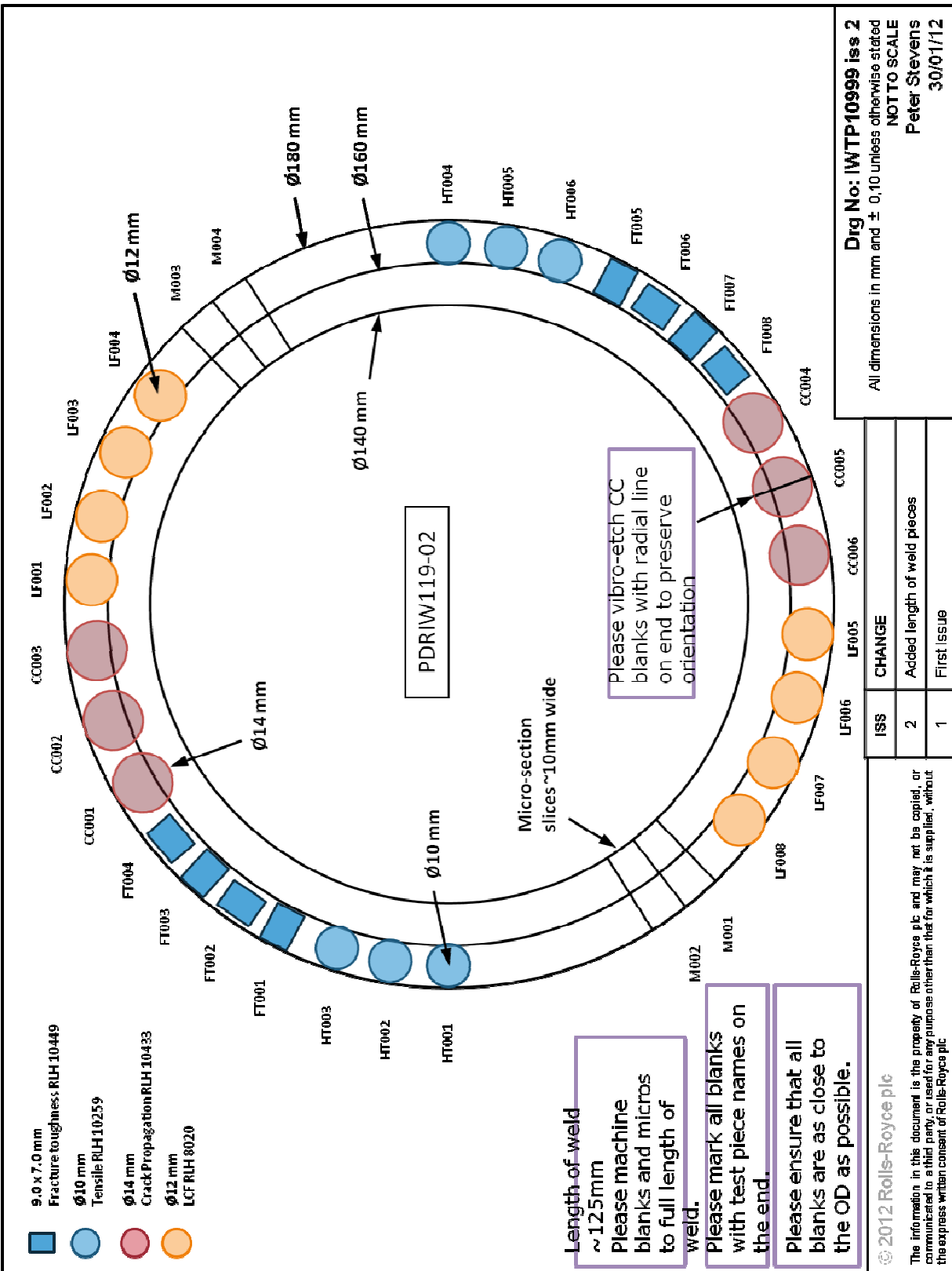


Figure 4.1: Sectioning of Inertia welded PDRIW119-02 Ring

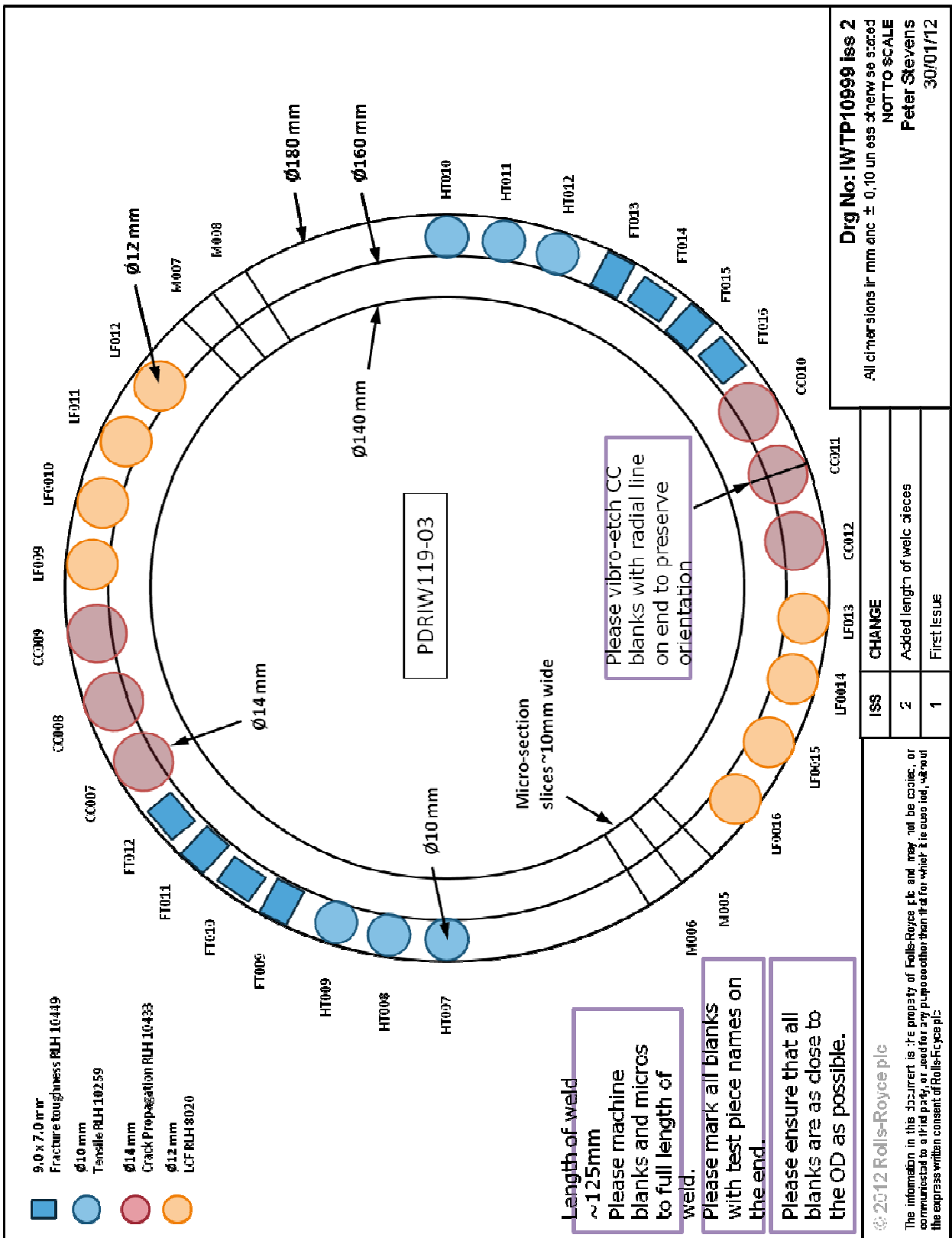


Figure 4.2: Sectioning of Inertia welded PDRIW119-03 Ring

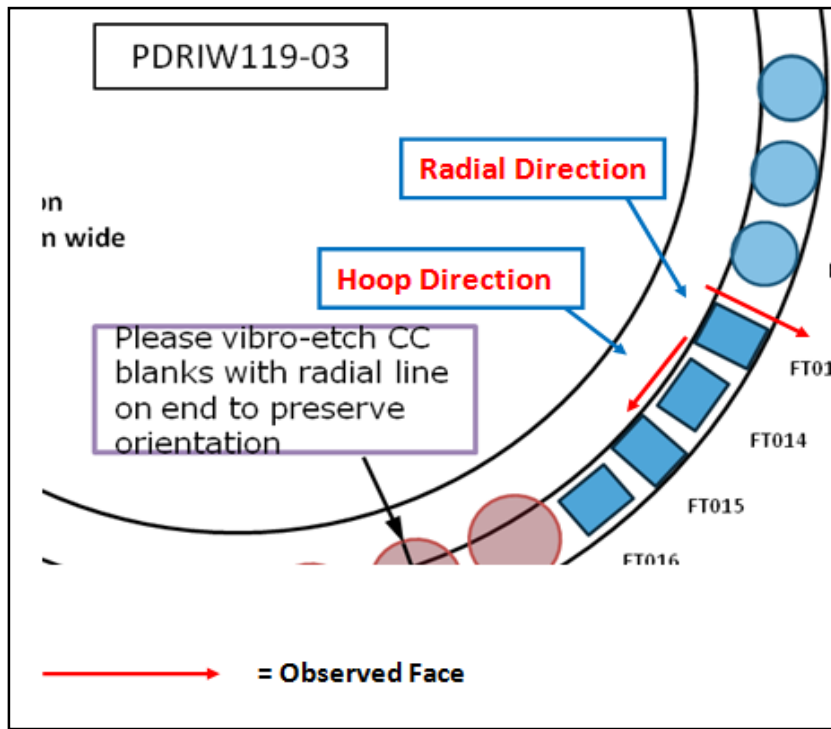


Figure 4.3: Sectioning of hoop and radial samples for microstructure analysis and threshold testing

Samples were also required for microstructure analysis using both Optical Microscopy (OM) and Scanning Electron Microscopy (SEM) along with the micro-hardness plots. These samples were cut from two orientations out of the welded rings again using EDM in both the hoop and radial orientation as shown in figure 4.3. The cross section of these samples was 10 mm X 8 mm with the larger side being used to grow the crack. A Beuhler-Isomet 4000 linear precision saw (figure 4.4) with a silicon cutting blade was used to produce samples of the required geometry. These samples were then mounted in conductive Bakelite using an Opal 460 mounting press (figure 4.5). In order to obtain a good quality of image to detect grains and features and to remove any scratches on the surfaces, the samples were ground and then polished using a Struers Labopol-5 automatic polishing machine (figure 4.6). With each sample a sequential procedure was used including a variety of discs and solutions, which can be found in table 4.3 [28]. The final stage of sample preparation for the microstructure work was etching. This was carried out using a solution composed of 2ml HF, 10ml HNO₃ and 88ml H₂O [29].



Figure 4.4: Beuhler -Isomet 4000 Linear Precision Saw



Figure 4.5: Opal 460 Mounting Press



Figure 4.6: Struers Labopol-5 automatic polishing machine

4.5 Microstructure analysis

In order to gain an understanding of the microstructure of the welds that had been produced and characterise the welds in accordance with mechanical properties, both Optical microscopy and SEM were used.

Step	Surface	Abrasive	Lubricant	Rpm	Time
1	MD-Piano220	SiC	water	300	As needed
2	MD-Largo	9µm-dimond suspension	N/A	150	5 min
3	MD-Chem	OP-S	N/A	150	5-10 min

Table 4.3-Grinding and Polishing procedure

4.5.1 Optical microscopy (OM)

The samples for this were prepared as stated in the sample preparation section. There were two microscopes used in this research. Firstly the Leica optical microscope was used to measure notch sizes and actual crack lengths within the threshold work. However, the primary microscope used for in depth microstructure work was the Zeiss Akioskop-2 using Axiovision software. This was used to analyse the weld as a whole and compare the differences in weld orientation, weld size, different weld zones and also to look for any noticeable flow lines apparent as a result of the welding process. During this, techniques such as mosaic were employed using the software.

4.5.2 Scanning electron microscopy (SEM)

During the SEM work, the samples were prepared using the same techniques as in OM. SEM was used in order to characterise the weld and the various zones present within, looking at the microstructure of each zone and any features present. This can

then be compared to the mechanical tests that had been conducted. These images and observations were to be the basis for explaining the mechanical properties of the IW Ti64. The parent material (PM) was observed to see the effect the welding process had on the microstructure and the changes that occurred. Various SEM machines were used to obtain these high magnification images using secondary electron imaging (SEI). These were the S4000 field emission gun (FEG) electron microscope (figure 4.7), Jeol 7000F with Oxford Inca EDS, Wave WDS and Crystal EBSD (figure 4.8) and Jeol 6060 with Oxford Inca EDS (figure 4.9). The individual parameters for the microscopes used in SEM can be seen in table 4.5.

Electron Microscope	SEI/BSE	Accelerating voltage (Kv)	Working distance (mm)
S4000	SEI	20	20
Jeol 7000F	SEI	20	10
Jeol 6060	SEI	20	10

Table 4.4 - SEM machines used and parameters

SEM was also used to analyse fracture surfaces after threshold and fracture toughness testing using the S4000 electron microscope and observing the microstructure within the fatigue region (threshold testing) and fracture region (fracture toughness). The fatigue region could be analysed in terms of microstructure at various ΔK . Ultimately this analysis was used to explain the crack growth behaviour occurring through the weld.



Figure 4.7: S4000 field emission gun (FEG) electron microscope

Figure 4.8: Jeol 7000F with Oxford Inca EDS, Wave WDS and Crystal EBSD



Figure 4.9: Jeol 6060 with Oxford Inca EDS

4.6 Mechanical testing

The specimens used for testing were produced largely by Rolls-Royce, plc using EDM. The samples for the various tests were taken from the welded rings as shown in figures 4.1 and 4.2. The specimens were taken from both the 02 and 03 welds and from different orientations in order to fulfil a complete testing matrix. Numerous mechanical tests were performed with varying specimen dimensions required.

4.6.1 Micro-hardness testing

The samples for micro-hardness testing were prepared in the same way as those for OM and SEM, with etching carried out to clearly show the weld and enable a hardness profile to be created. The profiles ran across the weld interface. Within the parent material a total of two hardness indents were made at each location and within the weld zone a total of five were used in order to attain as much data as possible from this region. This profile can be seen in figure 4.10.

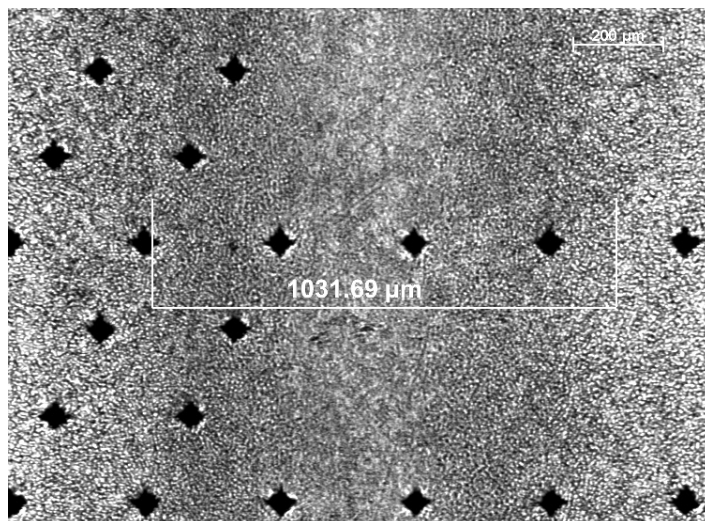


Figure 4.10: Micro-hardness plot across the weld region

The testing was completed on a Struers automatic hardness testing machine (figure 4.11), with a 1kN load applied and a 10 second time gap between measurements. The indenter used was a Vickers hardness indenter and each indentation was spaced by at least three times the indentation diameter as shown in figure 4.12.



Figure 4.11: Struers automatic hardness testing machine

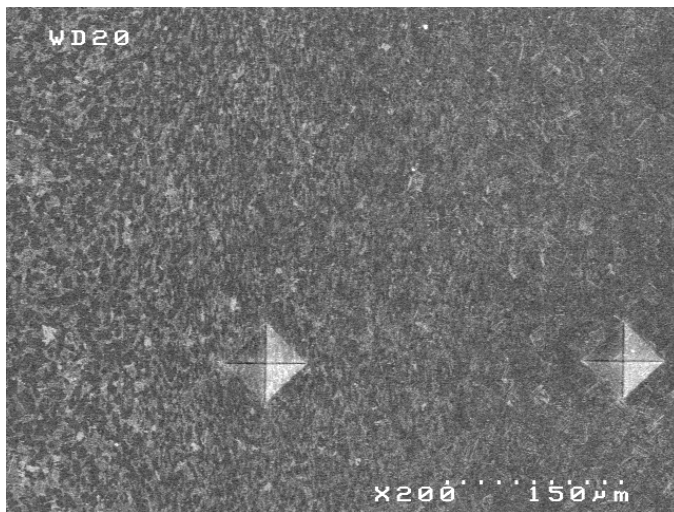


Figure 4.12: Micro-hardness indent spacing at X200 magnification

To ensure that the results obtained are 'real' three profiles were taken across each of the two welds. These hardness values (H_v) could then be plotted against the distance (mm) from the weld centre (CZ), comparing the varying results from each weld.

4.6.2 Mechanical threshold and crack propagation testing

The mechanical threshold and crack propagation tests carried out in this research were conducted in line with the standard testing procedures of British Standards Institute DD 186:1991 [30]. These samples were etched using a solution of 2ml HF, 10ml HNO₃ and 88ml H₂O (29). This was done in order to be able to visibly see the weld region. The samples were then placed under the Leica microscope with a mark being placed in the CZ. This mark was used as a guide for the notch (~1.2mm) to be cut using a Buehler Isomet – slow speed saw with a silicon cutting blade (figure 4.13).



Figure 4.13: Buehler Isomet – slow speed saw with a silicon cutting blade

The sample geometries are measured using calibrated vernier callipers to determine the required loads needed at the start of testing. Reverse bending is then carried out to sharpen the notch tip to allow for more likely linear crack growth and a straight crack front. The machine used for this testing was an ESH Servo-hydraulic testing machine (figure 4.14). Potential difference (PD) wires are welded to the sample to measure the current at the notch tip in mV. This is used to monitor the crack length during testing. The specimen is then placed under the required load with a DC

power supply being connected at either end of the sample for uniform current distribution, via crocodile clips (figure 4.15).

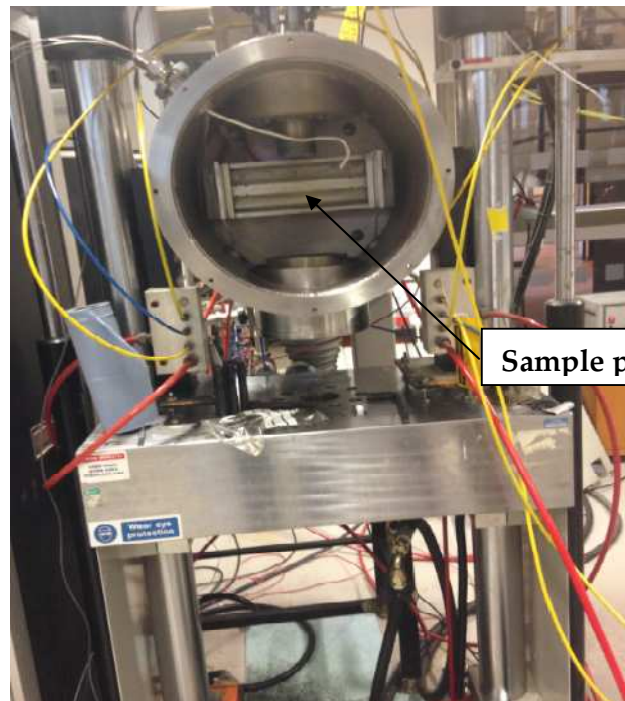


Figure 4.14: ESH Servo-hydraulic testing machine

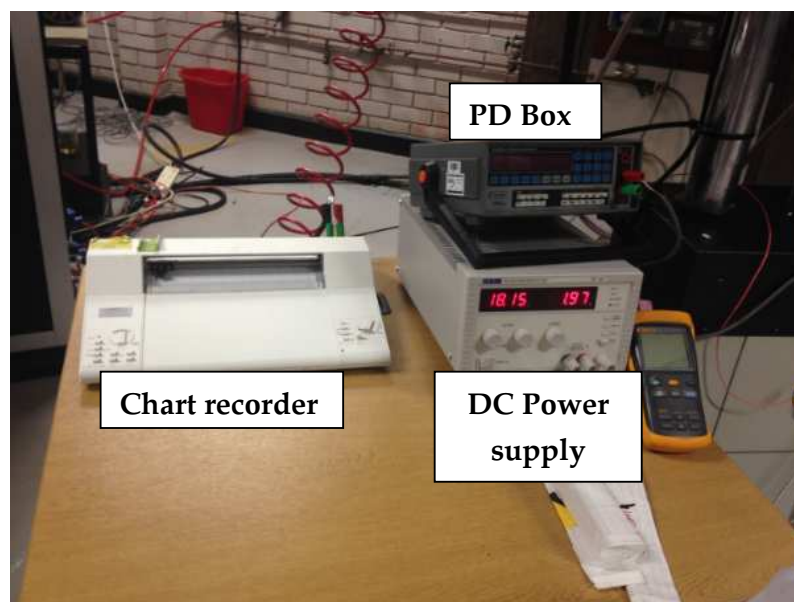


Figure 4.15: DC Power supply connecting to sample by PD wires.
Along with PD box and chart recorder

This method of monitoring crack length using PD operates on the principle that the “electrical resistance of a conductor increases with reduction in its cross sectional area”[3], this results in an increase in observed PD on the display and correlates with an increase in crack length. As well as a visual display on the PD box, a chart recorder is also used to plot the PD change over time (figure 4.15). Ceramic rollers are placed either side of the specimen at 10 and 20 mm. This testing procedure is therefore referred to as a 4-point bending test in accordance with British Standards Institute DD 186:1991 [30]. The waveform used within this testing was sinusoidal, operated at a frequency of 10 Hz.

The calibration function used to calculate the crack length and therefore a/W (crack length/sample width). This can be seen below in equation 1 [70]. This equation applies to samples loaded in a 4-point bend setup.

$$\frac{a}{W} = f\left(\frac{V}{V_o}\right) = -0.21395 + 0.59859 \left(\frac{V}{V_o}\right) - 0.15197 \left(\frac{V}{V_o}\right)^2 + 0.01733 \left(\frac{V}{V_o}\right)^3$$

Equation 1

Firstly the crack must be initiated and this is referred to as the pre-cracking stage. A K_{max} is selected that produces an appropriate ΔK within the stress area. The pre-cracking stage is conducted at a relatively high K_{max} although way below K_{IC} (fracture toughness), to initiate the crack and then reduced by 20% once the threshold testing began. Each time the load was changed the number of cycles was recorded from the cycle counter which along with crack length (a) was used to calculate fatigue crack growth rate (da/dN). It should be noted that the actual crack length was measured after the testing procedure was complete, by opening the sample up at the notch. This allowed a correction to be applied to the value calculated using the DC potential difference calibration method. The calculation for

da/dN is shown below in equation 2 [70], where N is the number of cycles. This five point secant of representing the crack growth was employed in order to give a smooth data plot.

$$\frac{da}{dN} = \frac{a_{+2} - a_{-2}}{N_{+2} - N_{-2}}$$

Equation 2

These da/dN plots are then plotted on a graph against the stress intensity factor range (ΔK), which can be calculated using equation 3 [70]. These graphs represent the crack growth curve and are generated using a lo-log plot, an example can be seen in figures 5.30-5.34.

$$\Delta K = \frac{3(P_{max} - P_{min})YS}{B(\frac{W}{10})^{1.5}}$$

Equation 3

Here B is the thickness of the sample, W is the width and S is the span between the outer and inner loading points i.e. 10mm. Y is referred to as the compliance function which can be described by the Walker and May polynominal. This function (Y) is shown below in equation 4 [3,31, 70].

$$Y = 1.99\left(\frac{a}{W}\right)^{0.5} - 2.47\left(\frac{a}{W}\right)^{1.5} + 12.97\left(\frac{a}{W}\right)^{2.5} - 23.17\left(\frac{a}{W}\right)^{3.5} + 24.8\left(\frac{a}{W}\right)^{4.5}$$

Equation 4

The stress ratios were selected, and the K_{max} was gradually reduced until threshold was reached in accordance with C which varied between 0.25 and 0.4. If threshold was not reached before $a/W=0.45-0.55$ [30], then the testing was stopped.

The stress ratio used in these tests was 0.1 and the testing was conducted at both room temperature and 400°C.

As mentioned the actual crack length was measured in order to give more accurate results.

This same setup was used to carry out the crack propagation phase of the testing. Once the crack had stopped growing or $a/W=0.45-0.55$ [30], the test was stopped. The next phase of the crack growth testing was then carried out (crack propagation). The test was started at a K_{max} below that at which the threshold testing began and increased by 20% so that as ΔK gradually increased so would the rate of crack growth until eventually the sample failed.

4.6.3 Low cycle fatigue (LCF) testing

The LCF testing was carried out by Rolls Royce, plc at Swansea Materials Research & Testing Ltd (SMaRT). The test pieces were again extracted from the two dissimilar welds using EDM. The load controlled LCF tests were carried out on an ESH servo-hydraulic testing machine with a load capacity of +/- 100kN, similar to that used in the threshold work.

During these tests a matrix of varying loads were applied to produce data that showed a range of different S-N curves. All of the LCF tests were carried out at 150°C, with the heat applied using multi zone radiant split furnaces. These temperatures were monitored using two type N thermocouples, located close to the centre of the sample. The amplitude was kept constant using a 0.25 Hz trapezoidal waveform with an R ratio of 0.1 being used. The dimensions of the test pieces can be seen in figures 4.1-4.3 with the measurements being taken using calibrated vernier callipers and micrometers. These samples conform to test piece design LCF RLH

8020 [32]. There were 12 LCF tests carried out in total with six being from each of the two welds.

In order to allow for true results, failure within the sample was defined as a complete fracture of the sample. These tests were performed in adherence to the SMaRT STOP documents for Force Controlled LCF Testing [33], in line with the British Standard BS6072:2011 [32, 34].

4.6.4 Tensile testing

The tensile testing was carried out by Rolls-Royce, plc at Swansea Materials Research & Testing Ltd (SMaRT). The test pieces were again extracted from the two dissimilar welds using EDM. These tensile tests were carried out on a Zwick servo-hydraulic testing machine with a load capacity of +/- 100kN. The tests were carried out in accordance with the Rolls-Royce testing procedure MMM31005 [35].

During the initial loading period of the tests, the strain rate was set at 0.3% strain per minute. Then upon reaching the proof stress, the control mode is changed to displacement mode and the rate is increased up to 10% per minute until specimen fracture takes place. The tensile testing was conducted at three different temperatures, room temperature (RT), 150°C and 300°C. The dimensions of these test pieces can be seen in figures 4.1-4.3 [32]. There were five tensile tests carried out on each of the two welds. These samples conform to test piece design RLH 10259 [32]. The results for these tests were plotted on stress-strain curves with the Proof stress, Ultimate Tensile Strength (UTS) and strain to failure values being recorded.

These tests were performed in adherence to the SMaRT STOP documents for Test Methods and Data Analysis for Tensile Testing of Metallic Materials [36], in line with the British Standards BS EN 2002-2:2005[37], BS EN 6892-1:2009 [38] and BS EN ISO 6892-2:2011 [32, 39].

4.6.5 Fracture toughness testing

The method used to carry out the testing of the samples via fracture toughness testing was very similar to that of the mechanical threshold testing. The testing was carried out in line with the standards ASTM E 1820-05 and ASTM E399-90, whereas with the mechanical threshold tests the samples required notch preparation, the samples for fracture toughness testing were supplied already notched by Rolls Royce, plc.

The method used to setup the test and pre-cracking stage is identical to that of the threshold test. However, where in threshold testing the K_{max} was reduced by 20% in order to find the mechanical threshold (stage at which the stress applied is too small to be able to continue to propagate the crack. The k_{max} for fracture toughness testing was kept constant until a value of 0.5 a/W was reached. Once this value had been reached a ramp up rate of 0.1mm/min or 0.5mm/min was used to propagate the crack very rapidly until a stress intensity factor was reached (K_{IC}) was reached that caused the samples to fracture. The K_{IC} can be calculated by the below equation 5 [71, 72].

$$K_{IC} (MPam^{0.5}) = 3 \left(\frac{Pq}{KN} \times 1000 \right) \times \left(\frac{\frac{S}{B}}{\frac{W}{1000}^{1.5}} \right) \times \left(\frac{f \left(\frac{a}{w} \right)}{1000000} \right)$$

Equation 5

These K_{IC} values can be seen as peaks on fracture toughness curves as will be apparent in the results and discussion.

The stress ratios used in these tests were either 0.1 or 0.5 and the testing was conducted at both room temperature and 400°C.

CHAPTER 5 RESULTS AND DISCUSSION

5.1 Characterisation of Ti64 to Ti64 Inertia weld

5.1.1 Microstructure of parent material

The microstructures of the Ti64 samples observed were generally bi-modal microstructures. These consist of equiaxed α grains situated in a transformed β matrix (figure 5.1). Within this transformed β matrix was secondary α in the form of coarse acicular α plates (Figure 5.2).

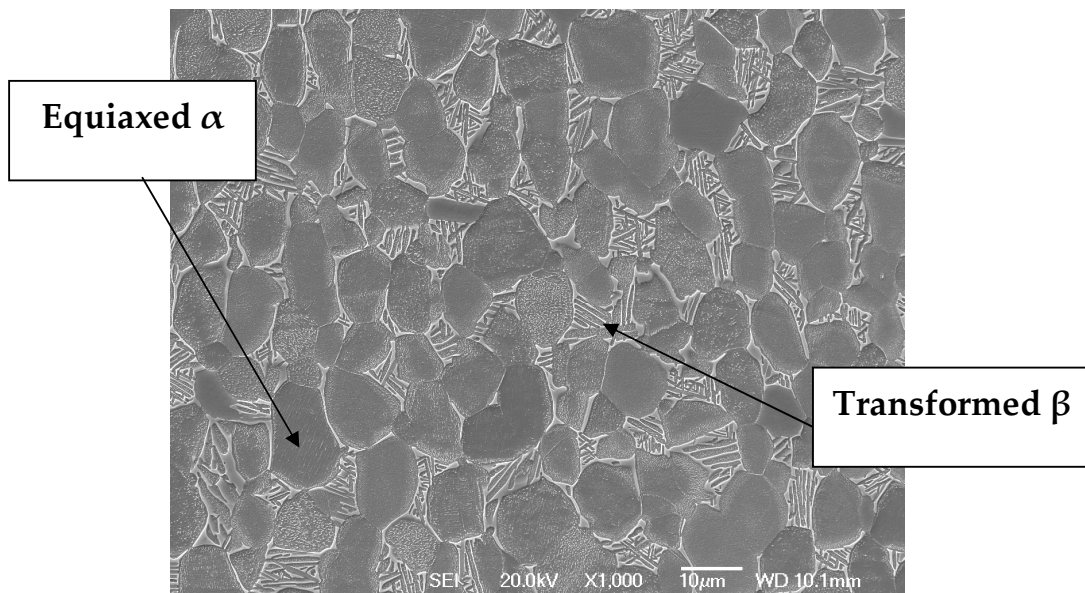


Figure 5.1: Equiaxed α grains in a transformed β matrix at X1000 magnification

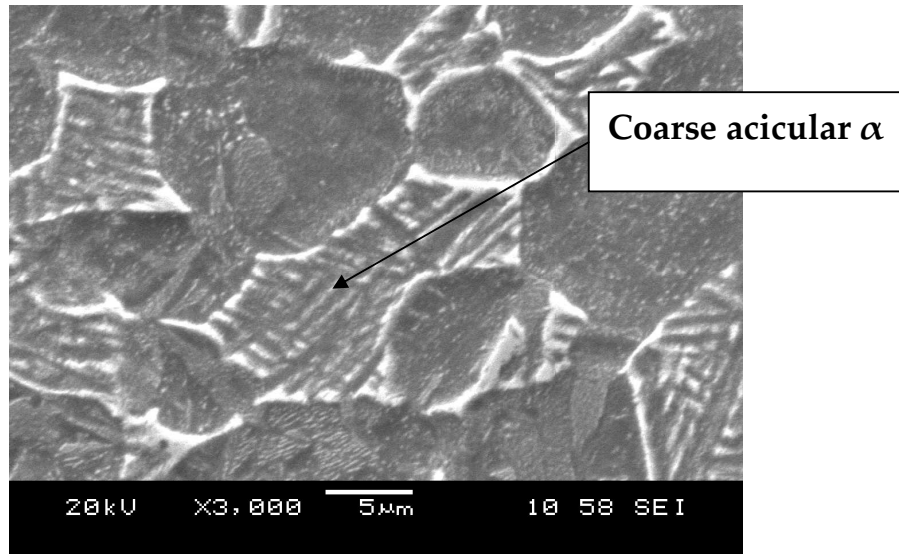


Figure 5.2: Coarse acicular α particles within transformed β at X3000 magnification

These parent microstructures whilst being influenced by the welding process and mainly determined by prior and subsequent processes. The equiaxed primary α grains and transformed β are a result of the prior processing and heat treatment. To attain this type of microstructure it is generally said that four main processes are involved. Initially homogenization in the β phase field, deformation in the α - β field followed by re-crystallisation again in between fields. The final part of the heat treatment process is ageing.

This ageing process is crucial to giving titanium its properties as it allows the alloying elements (vanadium and aluminium amongst others) to diffuse through the structure due to them still being in solution after the quench and form inter-metallic particles giving the Ti64 its enhanced mechanical properties. This solution treating and ageing process is carried out at low temperatures around 500-600°C. This low temperature treatment is the reason for Ti64 performing best at lower temperatures below 500°C and typically 350-400°C. The rate of the quench from the homogenization temperature governs the size of the α grains and also acicular α within the transformed β matrix. This martensitic α requires a fast quench in order

to allow the martensitic α to form. The re-crystallisation process is another variable that can be varied. By varying the cooling rate of this re-crystallisation it is possible to influence the fracture toughness of the material [8, 52, and 53].

5.1.2 Microstructure of weld zone

The microstructure of the different weld zones were observed and evaluated. The variations in microstructure throughout these different zones is a direct result of the inertia welding process. The CZ, TMAZ and HAZ (figure 5.3 & 5.5) will be observed and the changes evaluated in line with distance from the weld interface. It is these microstructural observations that govern the resultant mechanical performance of the components once welded.

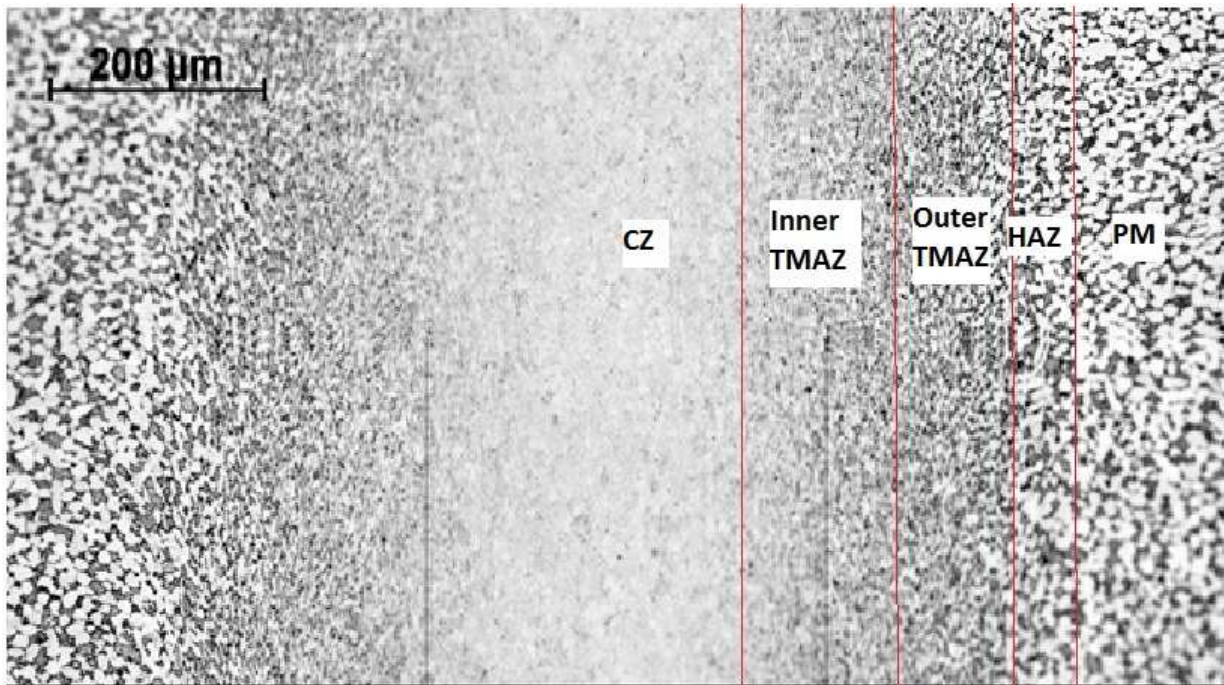


Figure 5.3: The different observed zones observed within the 02 weld

As seen in figures 5.4 and 5.5 there is a very obvious curved shape to the weld zone. The weld width is wider at the edge of the ring than at the centre in both rings. This is due to the higher heat density at the centre as shown by Muller et al (2010) in LFW (54). This heat density then gradually reduces towards the edge of the sample. The high amount of energy upon initial contact results in temperatures above the β -transus temperature, leading to the formation of the CZ at the weld interface. The OM image in figure 5.3 gives a good account of the weld itself although to identify the microstructural differences SEM is generally required. Figures 5.4 & 5.5 also show the weld zones with the CZ, TMAZ and Parent being easily identified.

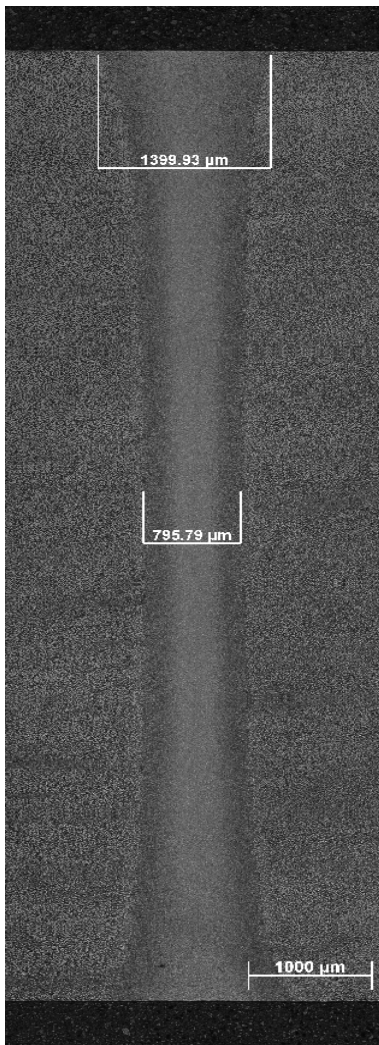


Figure 5.4: Inertia weld of PDRIW119-02 Ring

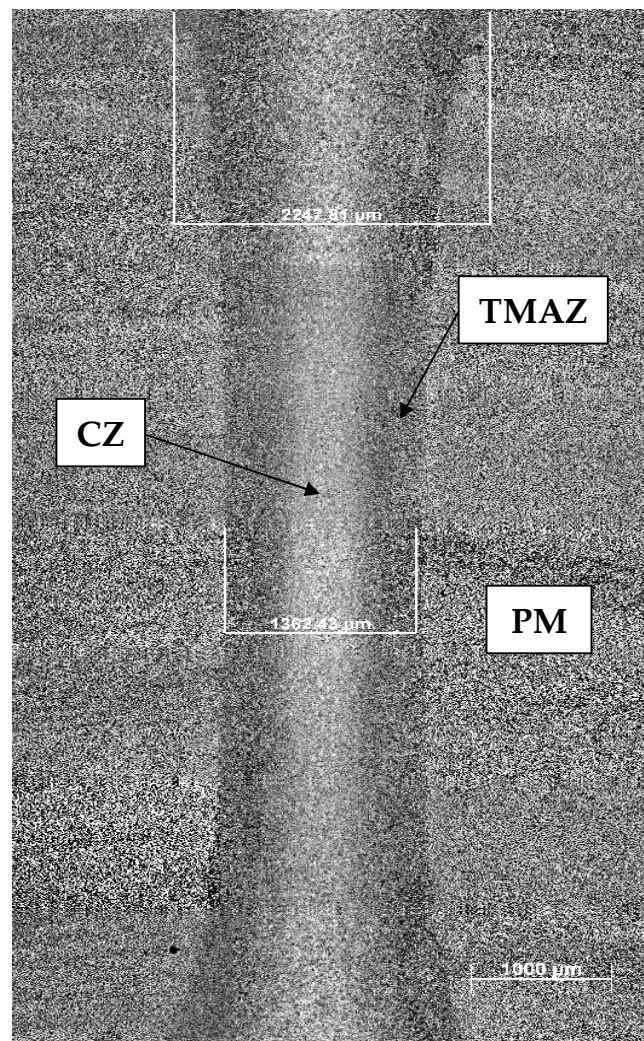


Figure 5.5: Inertia weld of PDRIW119-03 Ring

The cooling rate is vital in the formation of the weld zone and its appearance. The centre of the weld interface has a very rapid cooling rate once the optimum upset has been achieved, as heat is dissipated from the centre towards the parent material (cold end). This effect of cooling rate was also found by Boswell (2010) in LFW with cooling rates of up to 250°C being observed [55].

As you can see from figures 5.4 and 5.5 the 02 weld has a much smaller weld region at the centre 0.8mm than that of the 03 weld 1.36 mm. Both welds exhibit the shape typically found within inertia welding and at the edge of the weld interface are almost twice the width than at the centre. The reason for this variation in weld width must therefore be down to the welding parameters since the same process and material was used in each weld.

The 02 weld had a greater energy density 37.70 MW/m² compared to a reduced 30.60 MW/m² in the 03 weld. This was most likely a result of the increased rotational speed of the rotary part during the process 807 RPM in the 02 weld compared with 728 RPM in the 03 weld, this created a far higher temperature at the weld interface. The pressure applied to the 03 weld 137.90 Kg/m² compared to only 69 kg/m² in the 02 weld meant that the weld interface was exposed to a higher temperature for a shorter period due to the hot metal being expelled from the weld more rapidly in the form of flash. Whilst the width of the CZ is similar in both welds, the larger weld zone within the 03 weld would suggest that the weld width is determined mainly by the presence of extremely high pressures at the weld interface although most research by researchers such as Delgard et al (2010) on LFW contradicts this stating that the higher pressure would produce a smaller weld zone [56].

Generally a higher pressure means that material is expelled from the material faster and therefore leaving the material in the centre at high temperature for less time meaning a smaller weld. However, in this case less cold upset has been consumed at the higher pressure and therefore less material expelled which may explain the reason for the 03 weld having a larger weld zone despite the higher pressure. The reason for a smaller weld zone perhaps is a result of the higher rotational speed and

energy density of the 02 weld although more work is required in order to be able to state this with any confidence.

Another common feature observed during optical microscope observation of the inertia weld zones, was the obvious flow of the material dependent upon weld orientation. This phenomenon is apparent within the TMAZ as the material becomes plastic and is allowed to flow as shown below in figure 5.6. The reason why flow is able to be seen in the TMAZ and not the CZ is due to dynamic recrystallization occurring as a result of the extremely high temperatures.

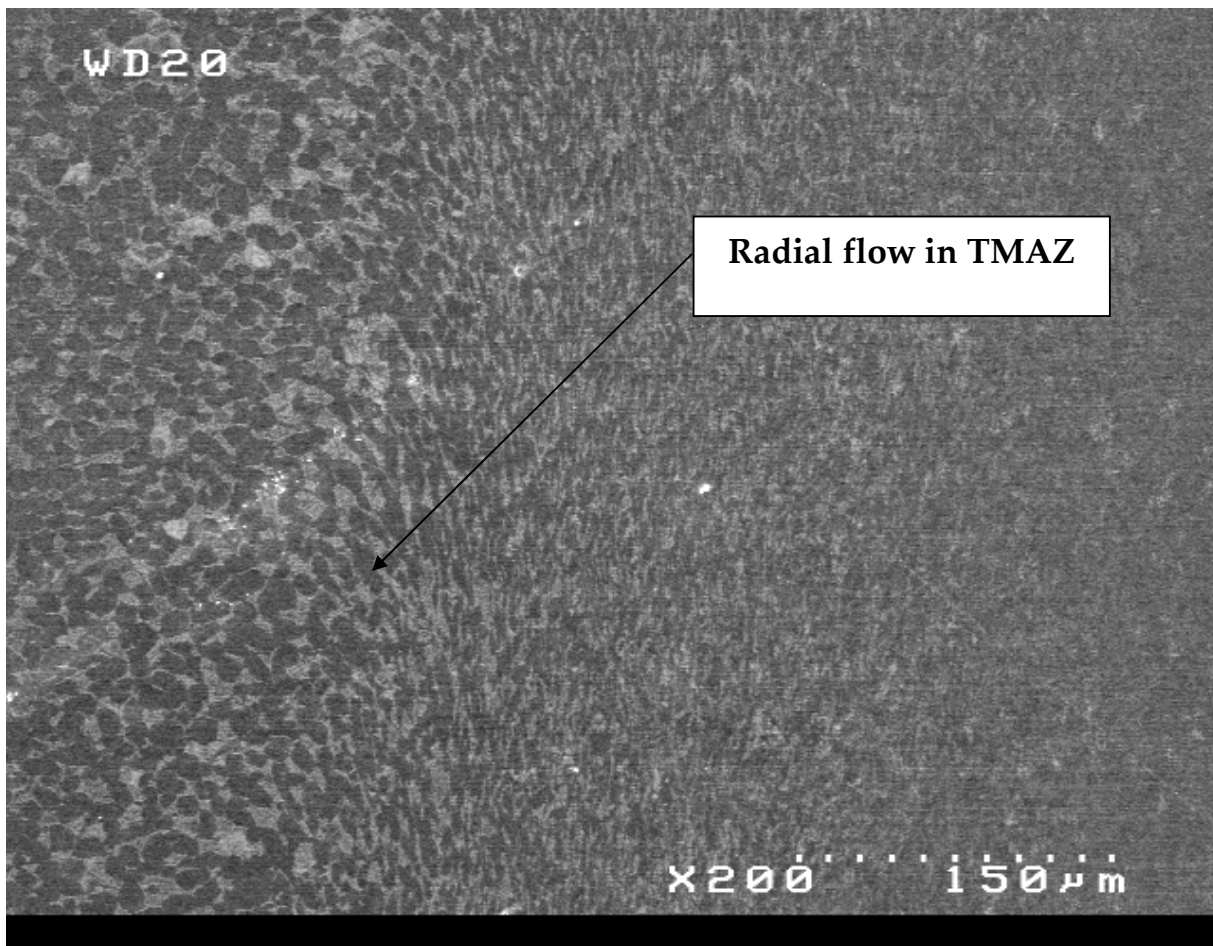


Figure 5.6: Radial flow of the material within the TMAZ of the 02 weld at X200 magnification

5.1.2.1 Central zone (CZ)

The central zone is located at the weld interface and formed after extreme exposure to heat and pressure after an oscillating and stationary part are brought together during the inertia welding process. The main reason for the features found within the CZ however is due to the cooling rate.

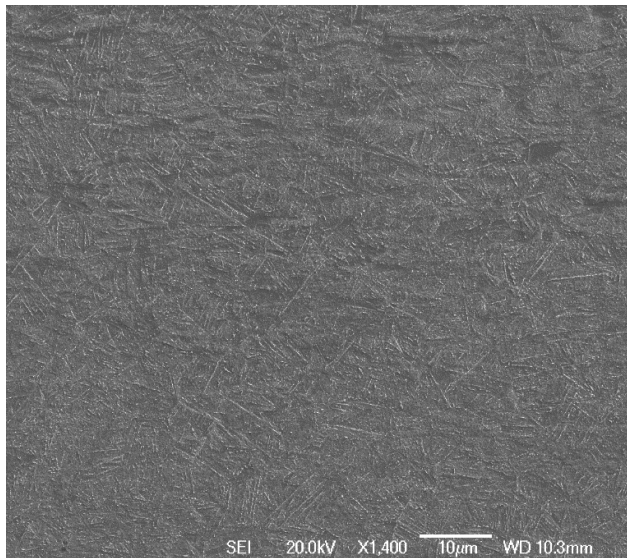


Figure 5.7: CZ of 02 weld at X1400 magnification

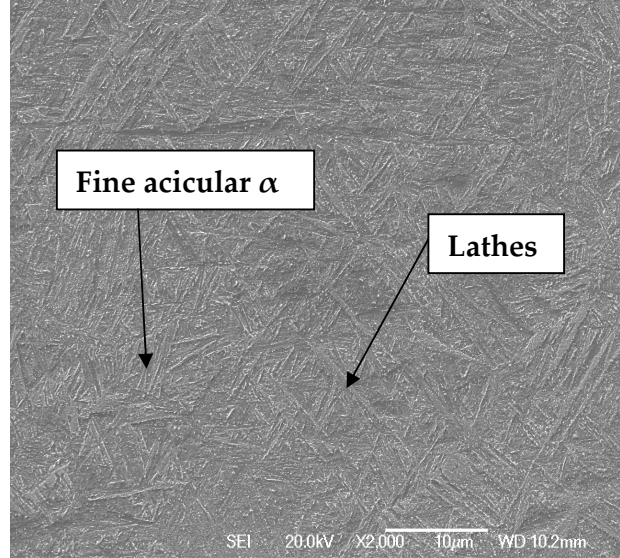


Figure 5.8: CZ of 03 weld at X2000 magnification

The CZ observed can be seen in figure 5.7 & 5.8 above. The microstructure observed here is a basket-weave microstructure with very fine acicular α particles. This was possibly due to the higher percentage of oxygen around the weld interface. The main reason for the formation of this fine acicular α is the cooling from above the β transus at temperatures of up to 1100°C [72]. However, due to the high temperatures produced during the welding process, the re-crystallised β grains with very fine 'needle-like' martensitic α transformed into fine α during the PWHT [3, 57 & 64].

The very fine equiaxed grain size observed within this weld zone is generally associated with the temperature being above the β -transus and re-crystallisation occurring (58). Pardhi (2010) observed that higher rotational speeds on the inertia welding of Ti6246 resulted in larger grain size than slower rotational speeds

although the grains were always equiaxed. This increase in rotational speed means that the cooling rate is faster due to the higher thermal gradient between the cold parent material and the weld interface. More work is required to validate this in Ti64. However, it can be expected that the 02 weld will produce grains of a smaller size due to the increased cooling rate (3). This is backed up by Wanjara & Jahazi (2004) in their work on LFW of Ti64 that suggested that higher rotational speeds and lower pressures will produce smaller grains within the CZ [72].

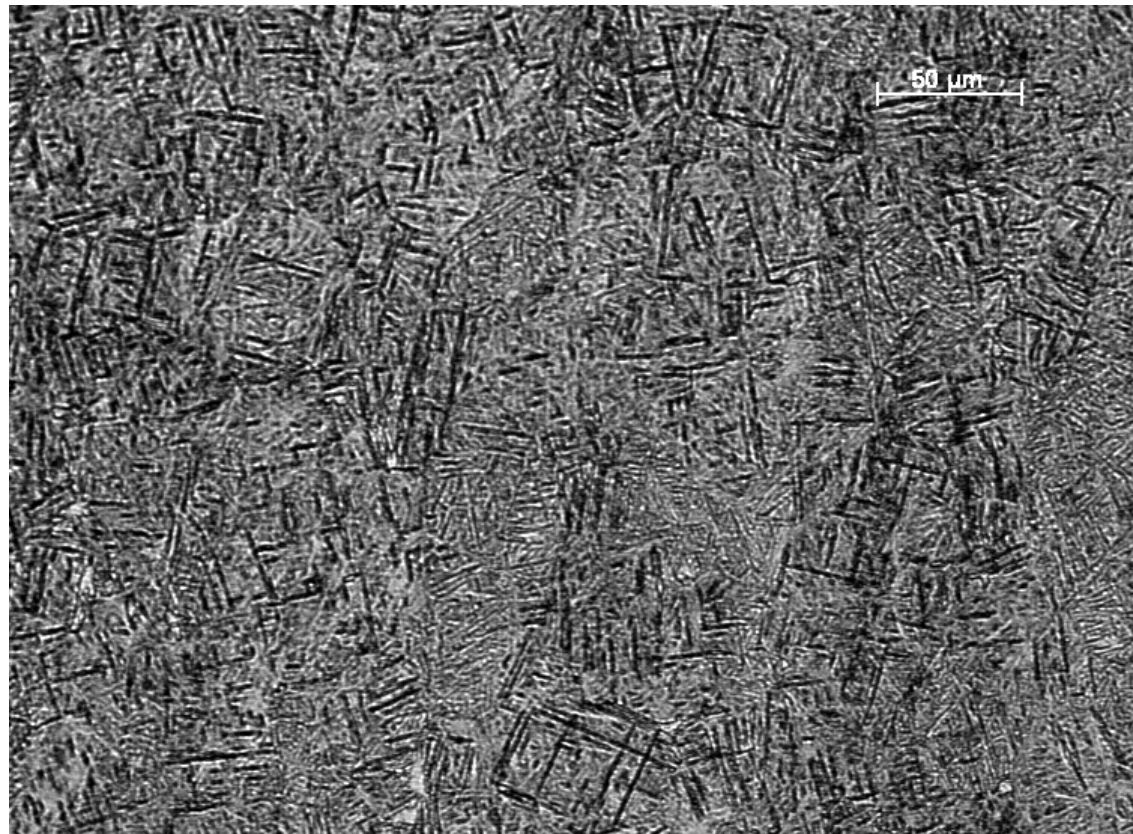


Figure 5.9: Equiaxed Basket-weave microstructure with fine acicular α in the 03 weld

5.1.2.2 Thermo-mechanically affected zone (TMAZ)

As you move further from the weld interface the next zone that became apparent was the TMAZ. The literature regarding the TMAZ is varied with some researchers suggesting that this is one zone and others deciphering two separate zones, the outer and inner TMAZ.

Within the TMAZ material flow was observed as a result of the rotator nature of the two components at the interface. This is something that has been observed by Pardhi (2010). However, little research was done into the flow of material in the radial/hoop direction of the weld. Figures 5.10 and 5.11 show the material flow in the TMAZ, in the hoop direction within the 02 and 03 welds.

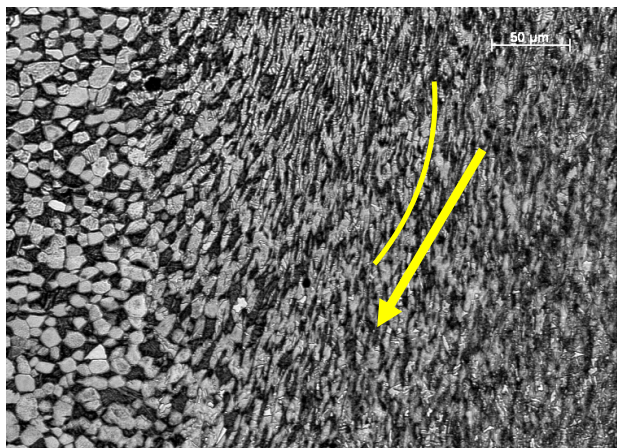


Figure 5.10: Hoop flow in the 02 weld

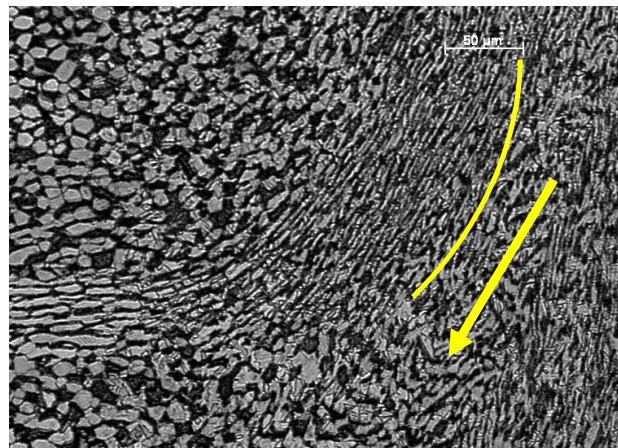


Figure 5.11: Hoop flow in the 03 weld

It can be seen that both welds have material flow when observed in the hoop direction. This flow is a result of the nature of the inertia welding process and the material flowing in a circular motion in line with the rotating component against the stationary component. This material flow was not observed in the radial direction however, which is something that whilst presumed until now has never been observed. This observed material was something not found by Yina [8] in her work on LFW of Ti64. This is due to the two components working against each other in a

reciprocating motion and therefore no distinct direction of material flow and relatively uniform structure along the weld interface. Whether this material flow has any detrimental and or property strengthening characteristics remains to be seen (8). The two welds whilst both showing this flow in the direction of component motion do have slightly different microstructures. Both have elongated grain structures due to the material attempting to flow in one direction under huge pressure although the 03 weld grains appear more uniform and less angular possibly due to the higher pressures it is exposed to.

The TMAZ will be observed in greater detail and shown to have two distinct zones as opposed to being just one as proposed by Yina [8] and many other researchers. This is similar to the observations of Pardhi ([3], although he determined that the HAZ was split into two zones rather than the TMAZ [3].

1) The Inner TMAZ

The inner TMAZ is located immediately adjacent to the CZ and therefore contains many of its characteristics.

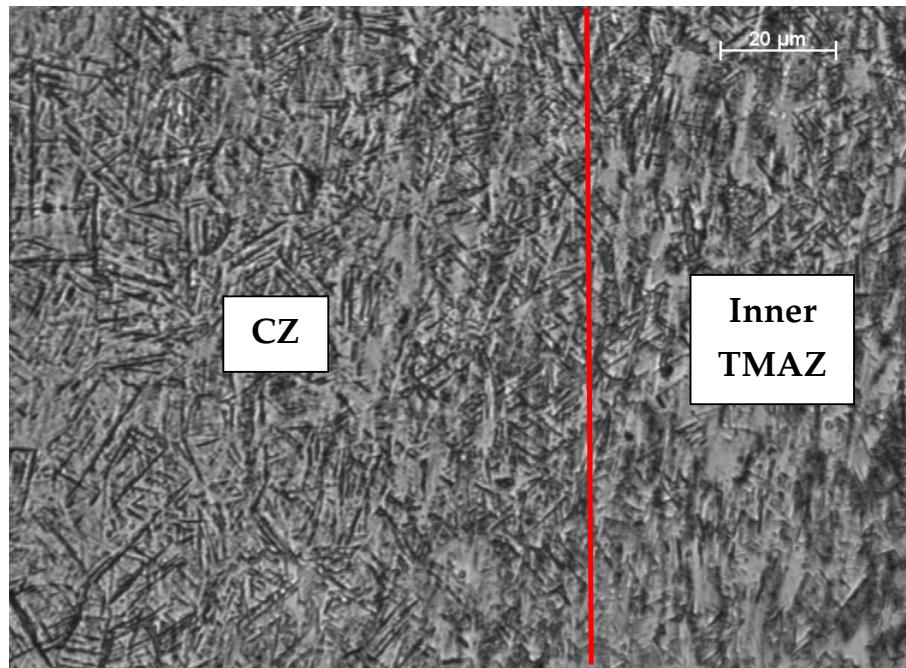


Figure 5.12: The CZ and inner TMAZ in the 03 weld

Figure 5.12 shows the transformation from the CZ to the inner TMAZ. The grains are a mixture of both equiaxed and angular grains that have been distorted in the hoop direction due to material flow. This region is still exposed to extreme temperatures from the weld interface although the cooling rate is lower here.

As you move further away from the weld interface the α plates become more coarse and there is a presence of martensitic α . As the temperatures are hovering around the β transus for a very short time interval there is partial dynamic recovery occurring within this region. The partial dynamic recovery within this region means that some will be in the α phase and some in the β phase as a result of the temperature being neither above nor below the β transus. This TMAZ was observed under high magnification using SEM as shown in figure 5.13 [3, 8].

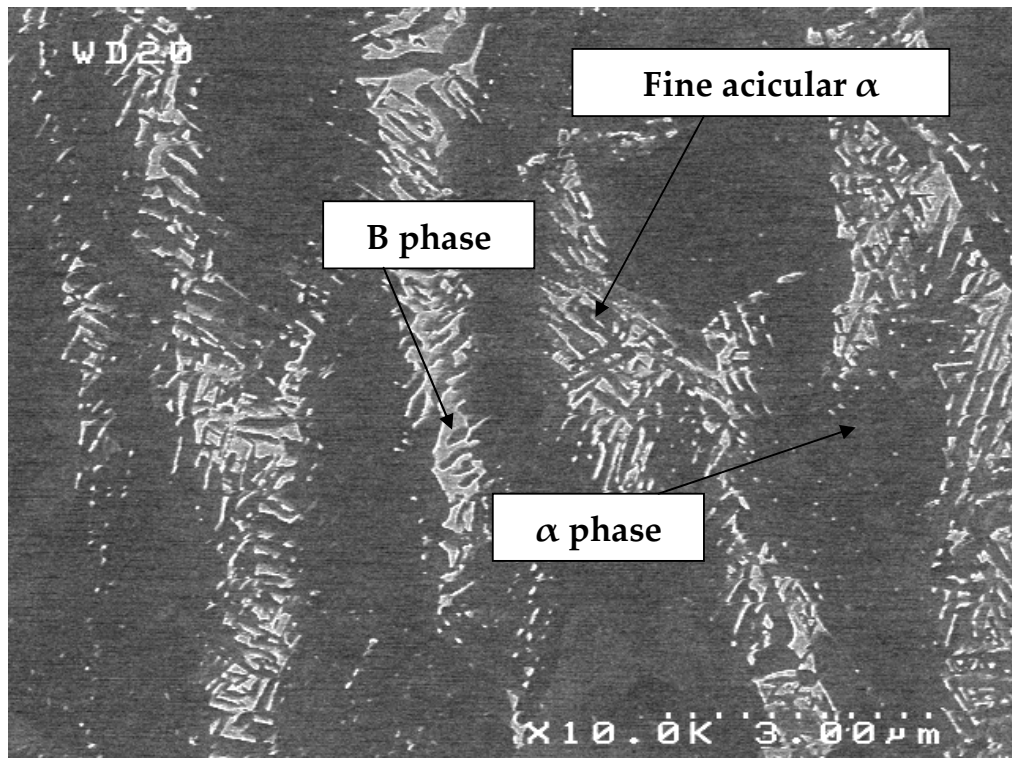


Figure 5.13: TMAZ observed at X10K magnification in the 02 weld

2) The Outer TMAZ

The outer TMAZ, or as Pardhi refers to it, the inner HAZ is the next zone along from the weld centre. Again this zone has features apparent both in the CZ and the parent material. The variation in microstructure between the inner TMAZ and outer TMAZ can be seen in figure 5.14 below [3].

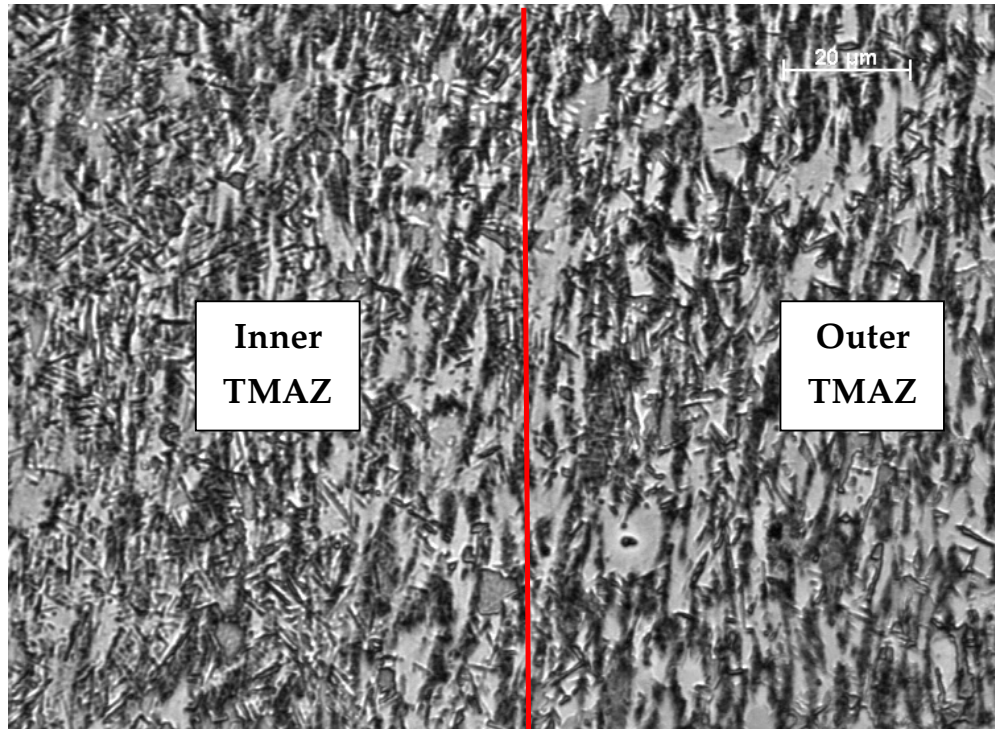


Figure 5.14: The inner TMAZ and outer TMAZ in the 03 weld

As you can see the α and retained β grains are still elongated and angular due to the plastic deformation that occurred within this region. This was due to the elevated temperature and material flow. The noticeable difference between the outer and inner TMAZ is the increase in grain size. The main reason for this is probably that the effect of both the heat and pressure will have far less effect in this zone and the opportunity for grain growth is possible due to a reduction in cooling rate. This progressive change occurs as you pass through the TMAZ and the presence of two

zones is very much open to interpretation, with some researchers such as Yina [8] classifying this region as one zone.

If any main difference was to be defined between the two zones, it would be that the α phases were larger and more apparent within the outer TMAZ. This is what was to be expected as more characteristic features of the parent material are picked up. These secondary α precipitates that form within the β phase are a direct result of the PWHT at 600°C [8].

5.1.2.3 Heat affected zone (HAZ)

The HAZ (figure 5.15) is the furthermost zone from the weld interface and is the last area where any noticeable difference can be observed from the parent material.

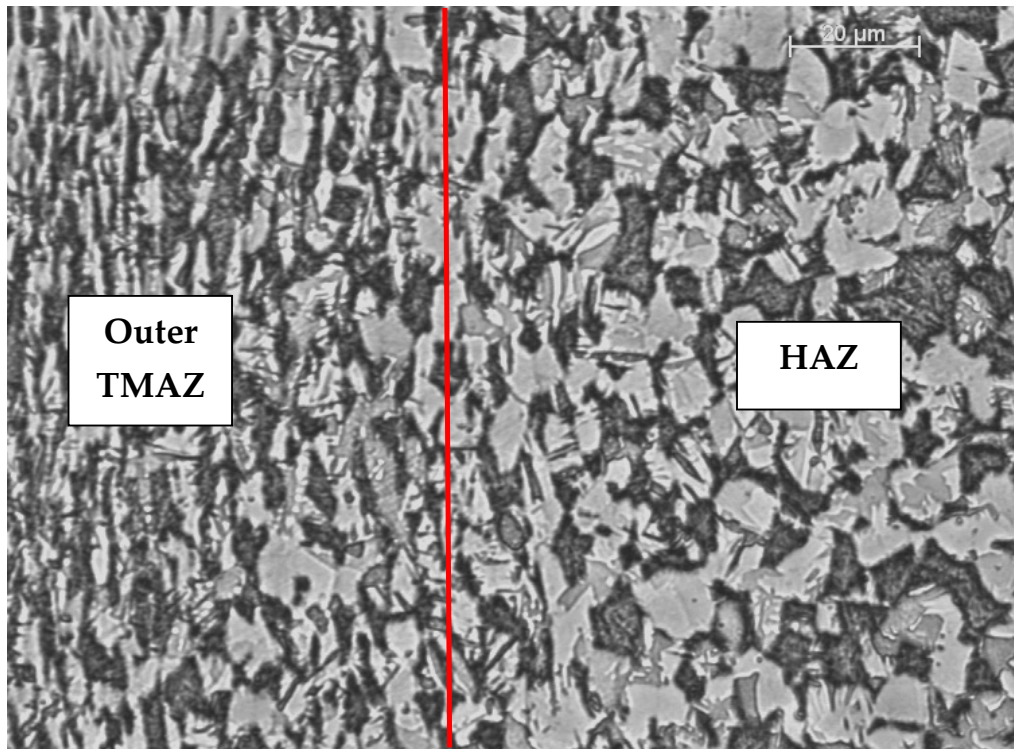


Figure 5.15: The outer TMAZ and HAZ in the 03 weld

The grains are noticeably more equiaxed and larger in size due to the conditions apparent at the weld interface having minimal effect. The β phase is now fully transformed and the α phase is clearly visible (figure 5.17) and much coarser than in the TMAZ. Figure 5.16 shows the difference between the HAZ and the parent.

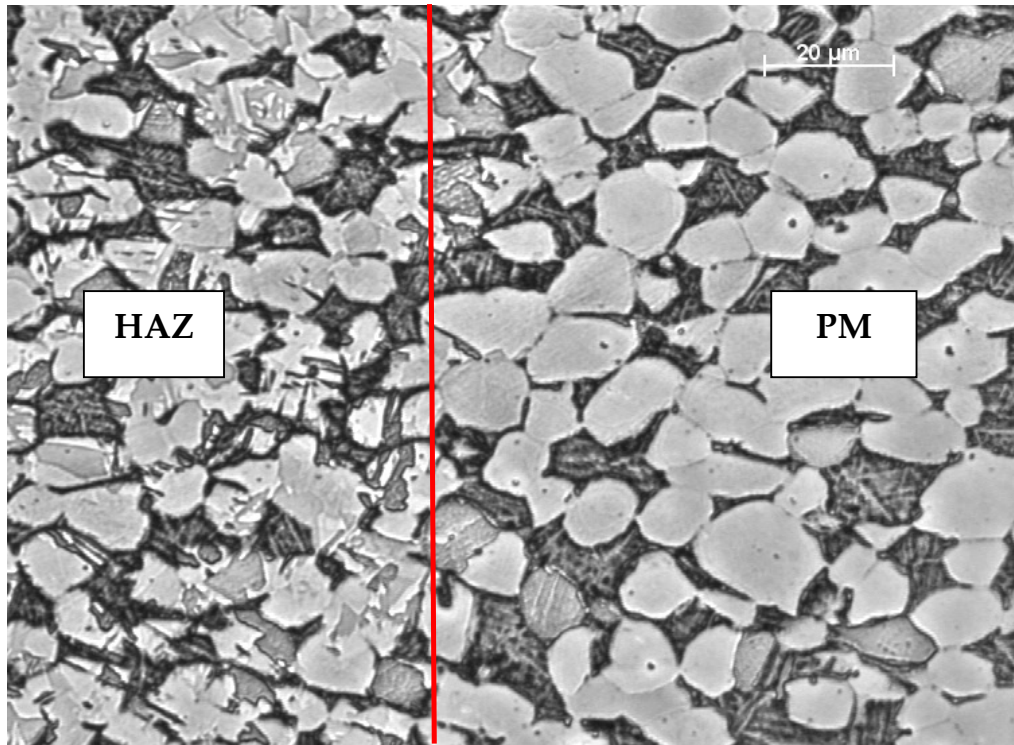


Figure 5.16: The HAZ and parent material in the 03 weld

In figure 5.16 you can see the α grains are larger than within the HAZ and the secondary α is very distinct within the β phase. The volume fraction of α can vary within the parent material and be intermediate as in figure 5.1 or very high as with figure 5.18. This figure also shows evidence of lamellar secondary α as opposed to the acicular randomly oriented secondary α previously observed.

The gradual change in microstructure from the weld interface into the parent material is shown clearly at high resolution in figure 5.19.



Figure 5.17: SEM image of the HAZ observed at X3500 magnification showing the transformed β phase and coarse acicular α

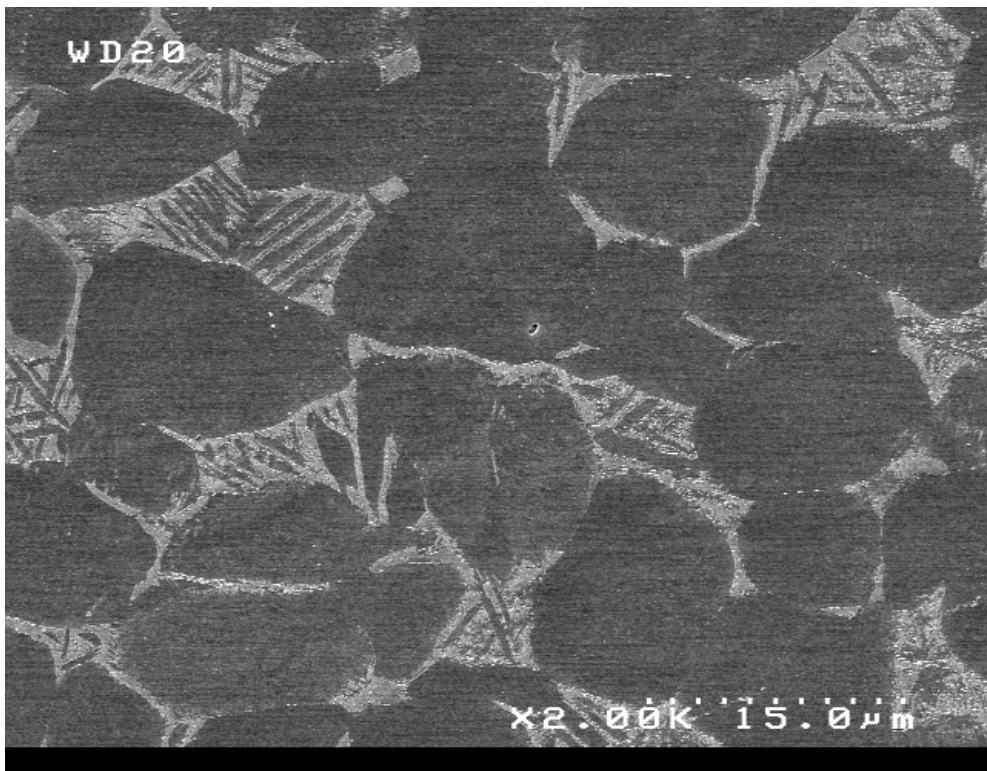


Figure 5.18: SEM image of the Parent observed at X2000 magnification showing the variations in secondary α precipitates

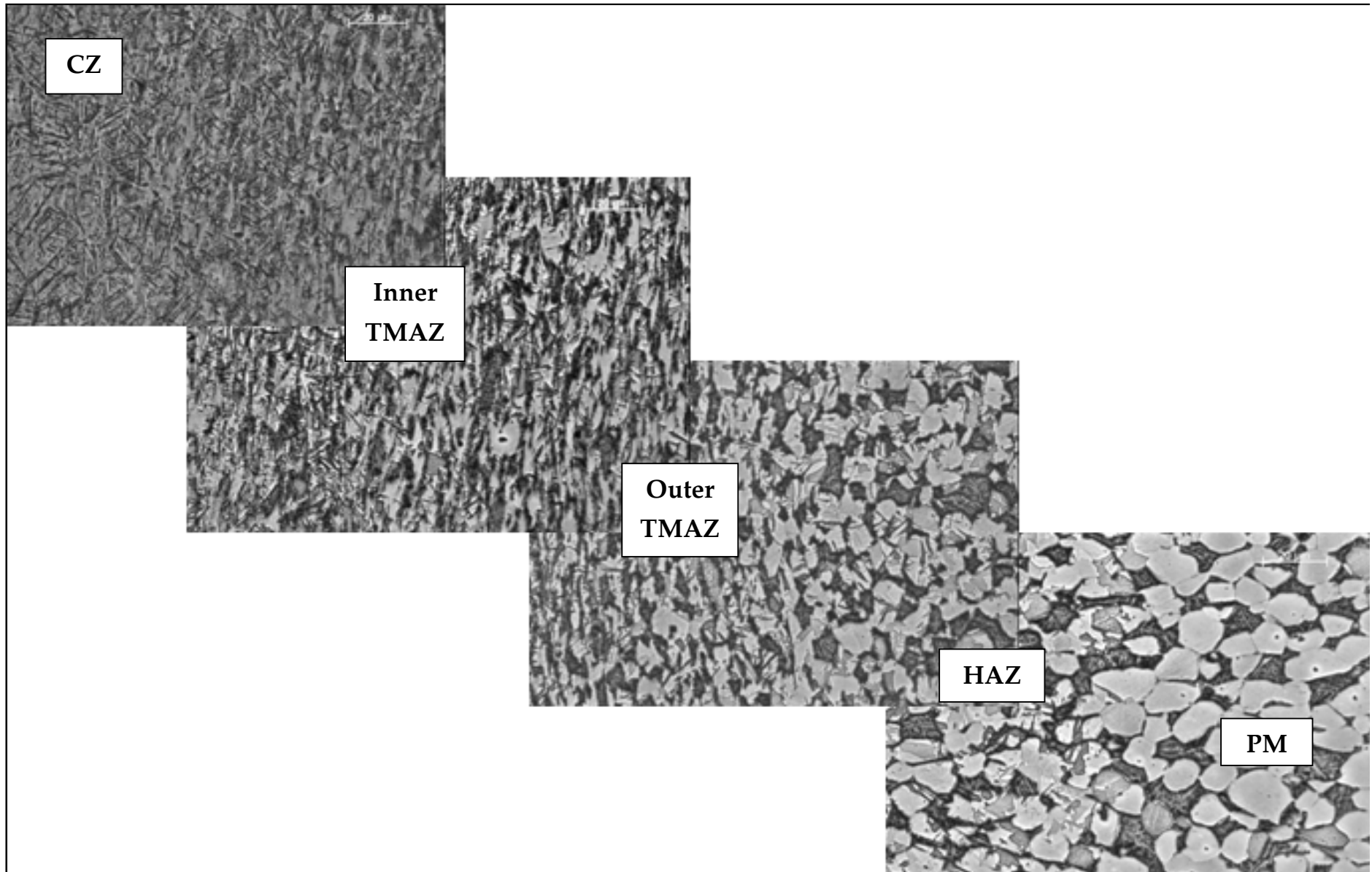


Figure 5.19: Optical microscope images of the changes in microstructure with distance from the weld interface

5.1.4 Micro-hardness distribution across the weld region

The micro-hardness profiles for both the 02 and 03 weld can be seen in figures 5.20 and 5.21. The top and bottom of the weld as referred to in the figures are the outer diameter (O.D) and inner diameters (I.D) of the weld.

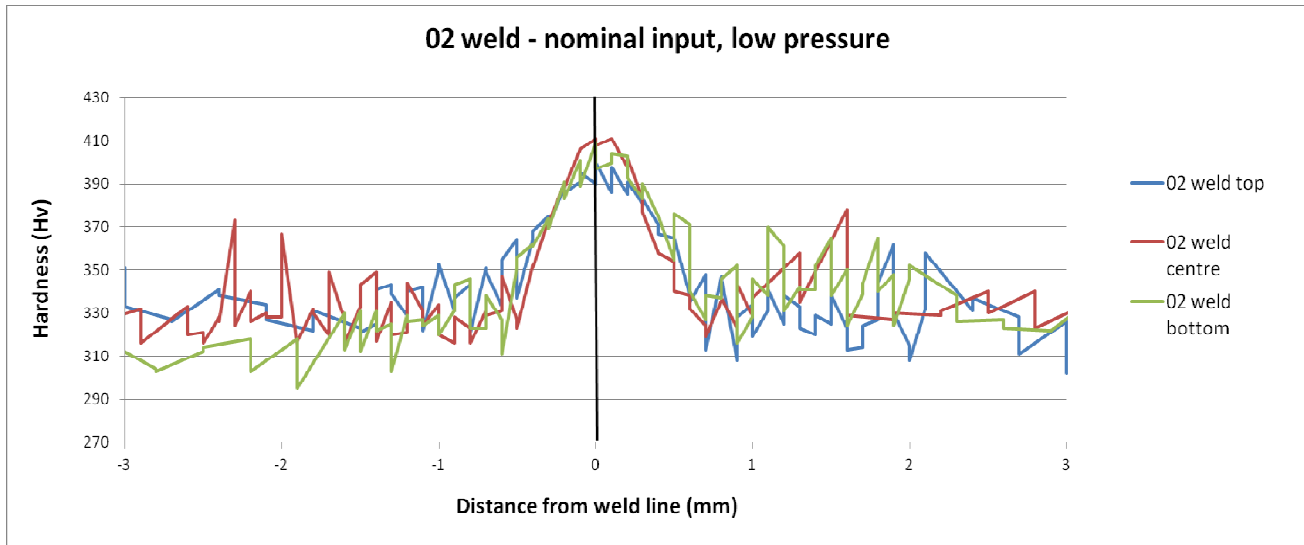


Figure 5.20: Micro-hardness profile of the 02 weld with higher energy density and rotational speed but lower pressure

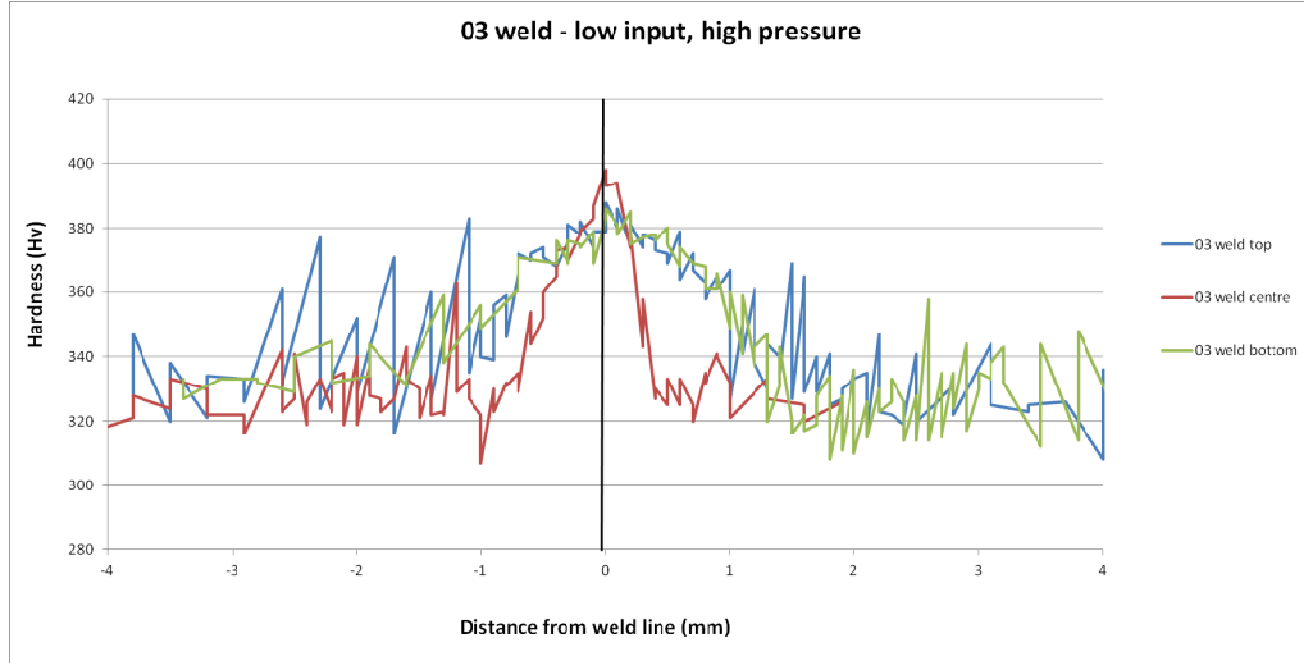


Figure 5.21: Micro-hardness profile of the 03 weld with lower energy density and rotational speed but higher pressure

The micro-hardness profile that was attained is very similar to work done by Yina (2010) and Wanjara & Jahazi (2004) in their work in LFW. The hardness within the weld zone is significantly greater than that of the parent material. The peak hardness within the 02 weld (410 Hv) is slightly higher than that of the 03 weld (395 Hv). This may be due to the slightly finer microstructure in the 02 weld as a result of the increased cooling rate due to the higher temperatures at the weld interface. This peak hardness is taken from the CZ. As you can see the 03 weld in figure 5.21 suggests that whilst the peak hardness is lower there is a larger area whereby elevated hardness results have been recorded suggesting a much larger weld zone in the 03 weld. This is backed up by the observed microstructures (figure 5.4 and 5.5). The difference between the micro-hardness results recorded can be seen more clearly in figure 5.22 [8, 71].

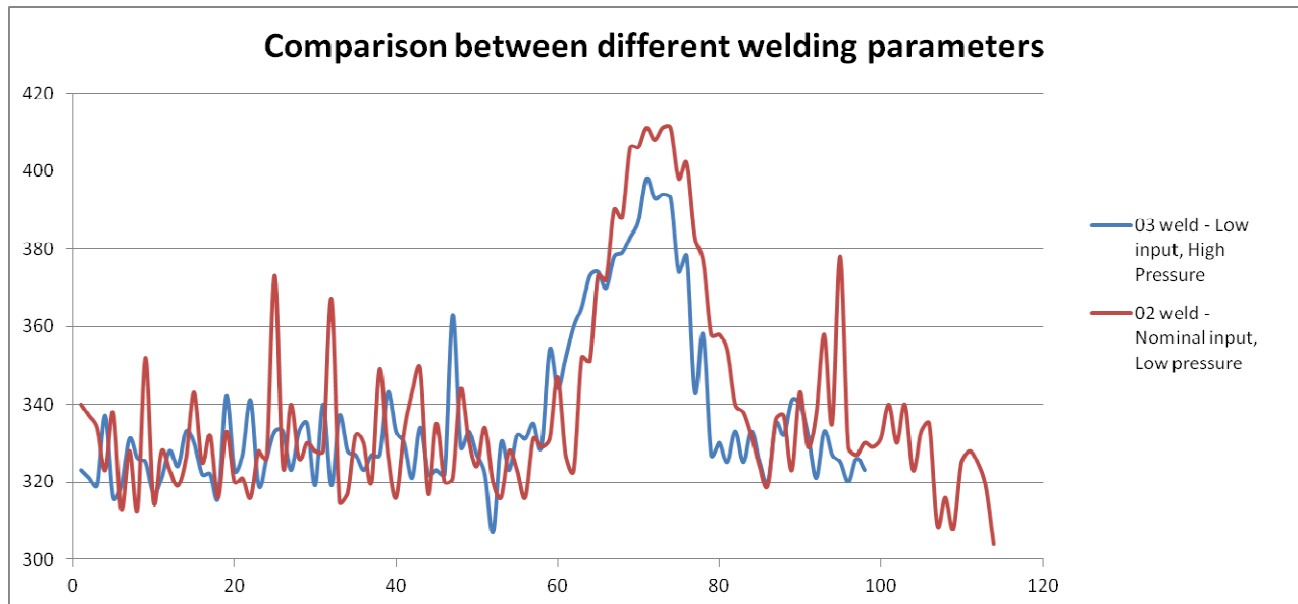


Figure 5.22: Comparison between micro-hardness in the 02 and 03 weld

The peak hardness within the CZ is due to a martensitic transformation occurring and a very fine microstructure due to the rapid cooling rate. As you pass into the TMAZ the micro-hardness is still elevated although it begins to drop off as the temperatures here are around the β -transus, although acicular α is present. There was no micro-hardness difference between the HAZ and parent material and if anything the hardness values within the HAZ are lower than the parent. The results are also very erratic in these areas. The reason for the hardness here being unaffected as you move away from the CZ is due to the microstructure being largely unaffected. This is a result of the heat not influencing the microstructure here as Ti64 is a poor conductor of heat. Therefore the HAZ microstructure largely has the characteristics of the parent. The micro-hardness distribution along with the change in micro-structure across the weld can be seen in figure 5.23.

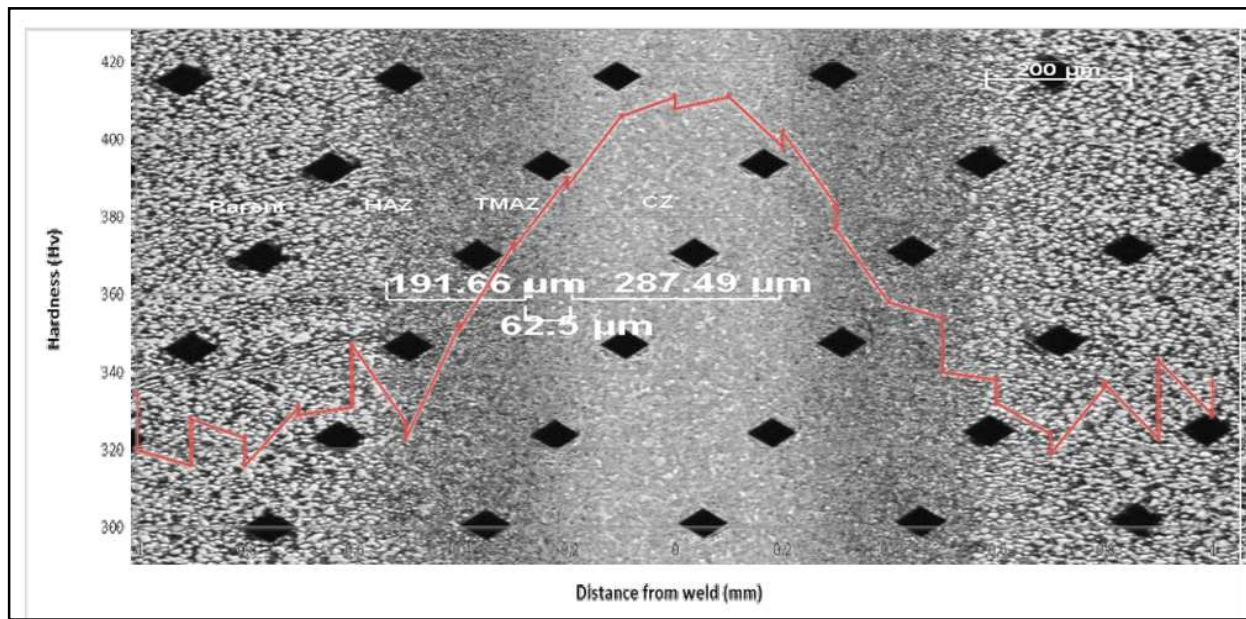


Figure 5.23: Micro-hardness distribution along with changes in micro-structure across the weld zone

The micro-hardness results suggest that the resultant peak hardness observed in Ti-64 is 410 Hv, although the micro-hardness did gradually drop-off as you move through into the TMAZ and HAZ. Pardhi who carried out work on Ti6246 put this down to the grain refinement within the CZ. The micro-hardness results here appear to show a very marginal decrease in the very centre of the weld giving a ‘trough-like’ appearance which was again observed by Pardhi [3] and also Wanjara & Jahaji [12] in friction welding of Ti6246 and Ti64 respectively. This is most likely a result of the formation of oxides and apparent porosity as this region is exposed to the atmosphere on initial formation although this phenomenon was not seen by Yina in LFW [3, 8, 12 & 71].

To compare Yina’s LFW results of Ti64 with the IW of Ti64 then the hardness values are very similar, around 320-350 Hv within the parent and a peak hardness of 410-420 Hv [8].

5.2 Mechanical testing

Now that the microstructure has been observed in the IW of Ti64, this must be compared and contrasted to the resultant mechanical properties of these welds. These mechanical properties are ultimately what allows for designers to substantiate whether processes are able to give the required mechanical properties. This enables them to determine whether the welded components are able to withstand the various environment stresses they are subjected to.

5.2.1 Effect of welding parameters and temperature on Tensile strength

The tensile testing was carried out by Rolls-Royce, plc at Swansea Materials Research & Testing Ltd (SMaRT) (32). The 02 and 03 welds were compared in terms of tensile strength and also at three different temperatures. A summary of the tensile results can be seen below in figure Table 5.1 [32].

Sample	Weld	Temp (°C)	UTS (Mpa)	Proof Stress (Mpa)	Strain to failure (%)
HT001	02	20	975	875	14.04
HT002	02	150	832	701	15.09
HT003	02	150	828	698	16.06
HT005	02	300	689	546	15.5
HT006	02	300	682	535	17.79
HT007	03	20	974	881	13.19
HT008	03	150	822	700	14.32
HT009	03	150	824	692	15.34
HT0011	03	300	679	540	15.63
HT0012	03	300	687	543	16.3

Table 5.1: Results of tensile testing carried produced by SMaRT for Rolls-Royce, plc at the Swansea Materials Research & Testing facility (32)

These results show that the samples taken from the 02 weld exhibited higher tensile properties than those taken from the 03 weld. The stress-strain curves for these tensile testing results can be seen in figures 5.24-5.26 [32].

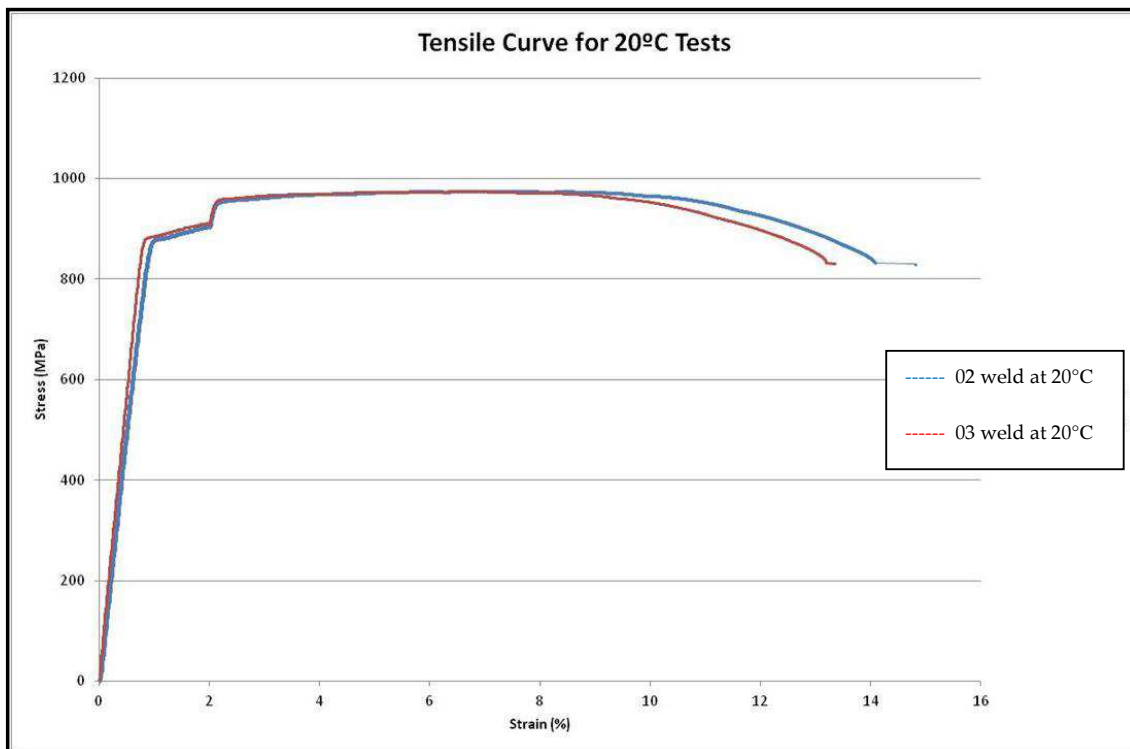


Figure 5.24: Stress-Strain curve at 20°C produced by SMaRT carried out for Rolls-Royce, plc at the Swansea Materials Research & Testing facility (32)

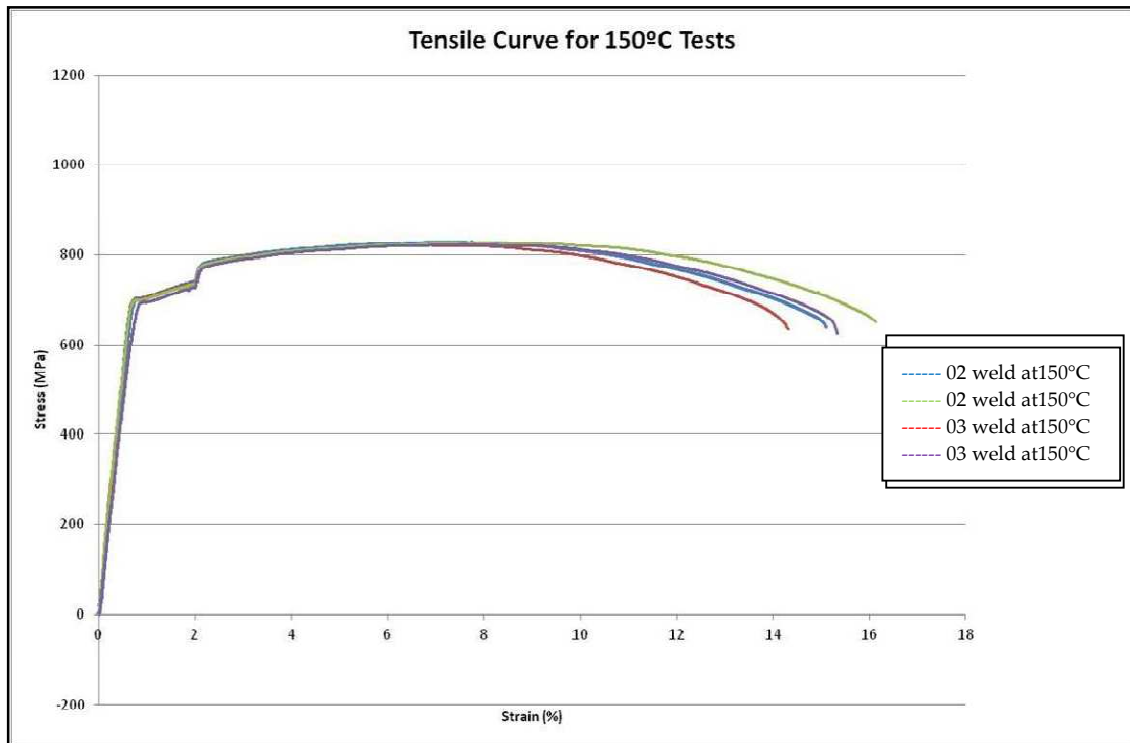


Figure 5.25: Stress-Strain curve produced by SMaRT at 150°C carried out for Rolls-Royce, plc at the Swansea Materials Research & Testing facility (32)

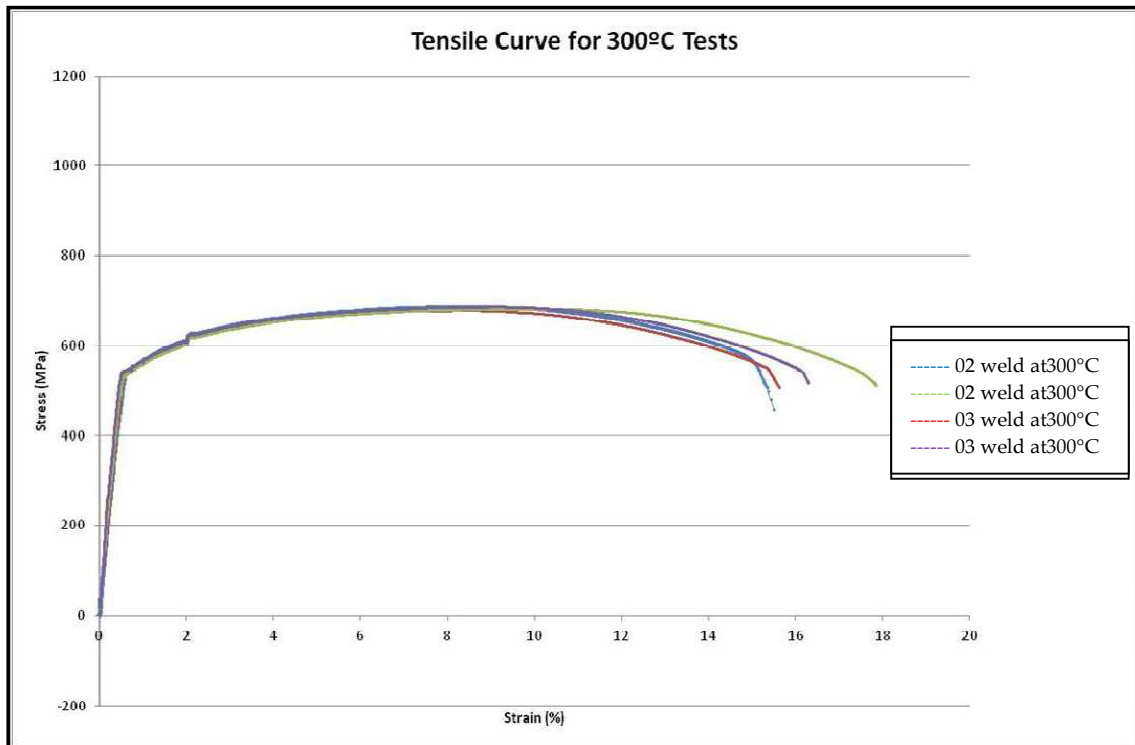


Figure 5.26: Stress-Strain curve produced by SMaRT at 300°C carried out for Rolls-Royce, plc at the Swansea Materials Research & Testing facility (32)

The variations between the two welds were only very marginal however and these differences cannot be seen visually in figures 5.24-5.26.

The welds were also compared in terms of difference in tensile properties across the three different temperature ranges as seen in figures 5.27 and 5.28. Here you can see much more clearly how the tensile properties reduce significantly as the temperature is increased. The significance of this however as proved by Pardhi (2010) is probably not great as the material always fails within the parent material. To actually test a material for tensile properties within the weld is near impossible. So providing the fracture site during a tensile test is within the parent material it can be said that the weld join is acceptable.

The most likely explanation for the increased strength in tension within the weld is the very refined microstructure due to re-crystallisation and fine α precipitates [3].

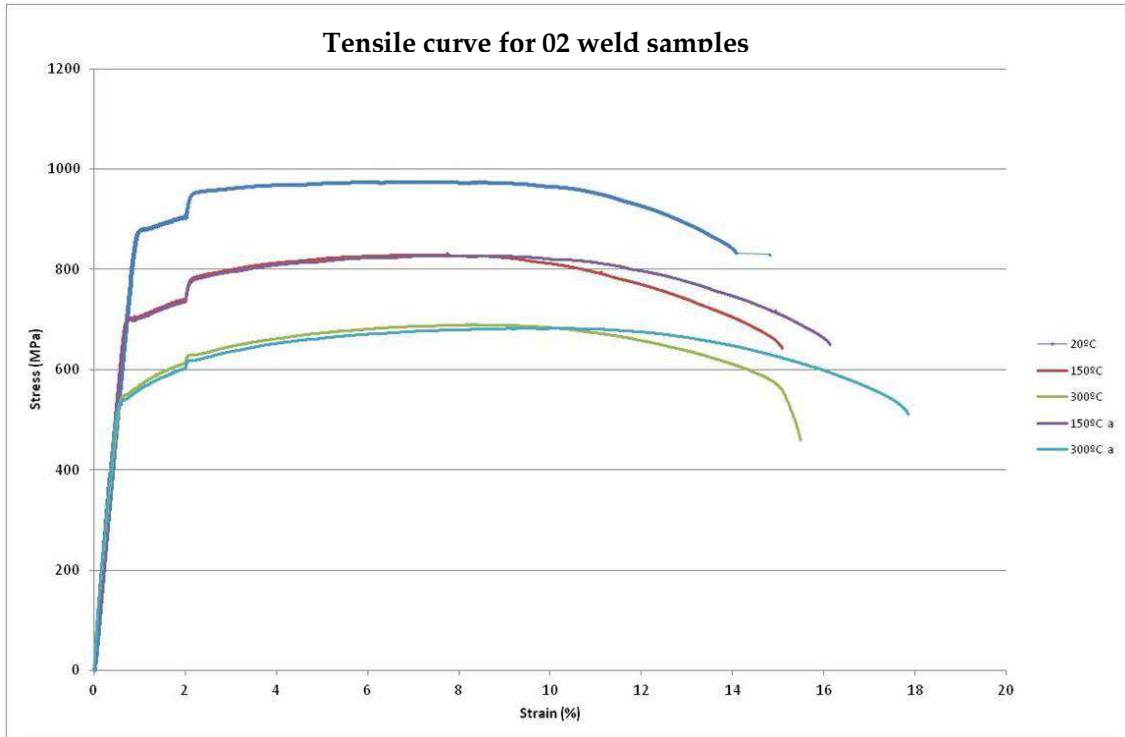


Figure 5.27: Stress-Strain curves produced by SMaRT for 02 weld samples carried out for Rolls-Royce, plc at the Swansea Materials Research & Testing facility (32)

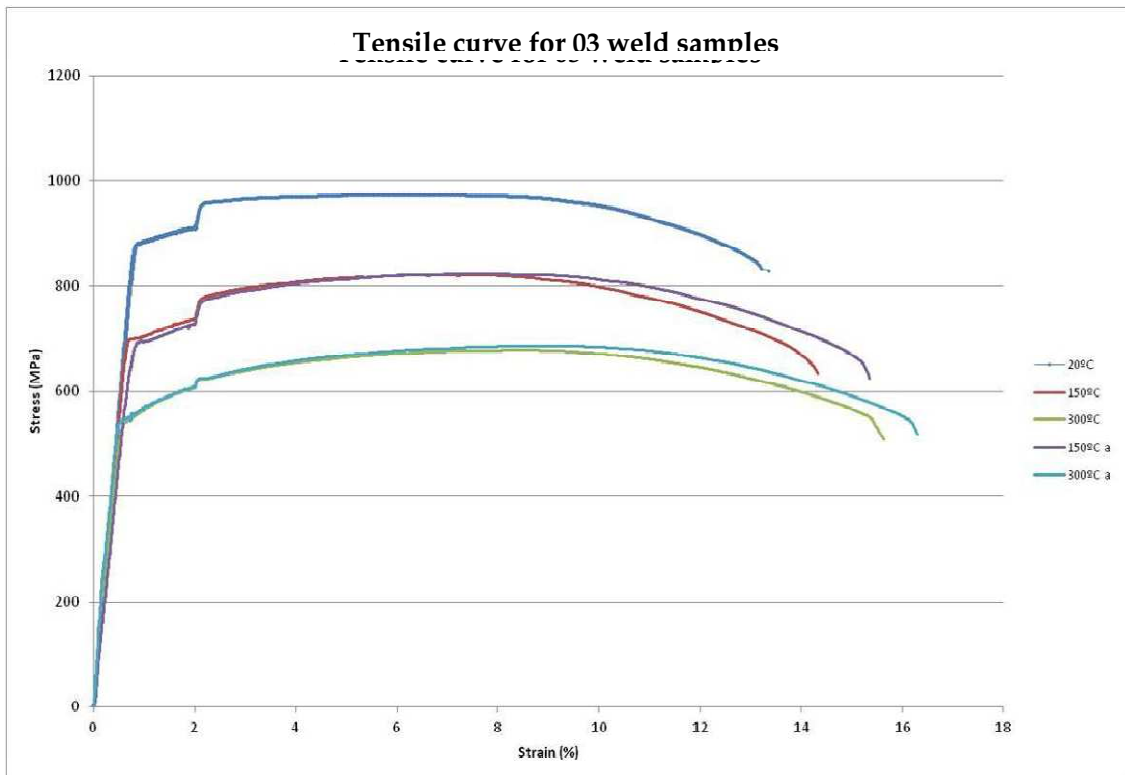


Figure 5.28: Stress-Strain curves produced by SMaRT for 03 weld samples carried out for Rolls-Royce, plc at the Swansea Materials Research & Testing facility (32)

5.2.2 Effect of welding parameters on LCF behaviour

Due to the nature of the application that these IW disks will be used in, the fatigue and crack propagation properties of the welds is hugely important in assessing their potential to excel in application.

The LCF is one such property that can be assessed. This work was again carried out by Rolls-Royce, plc at Swansea Materials Research & Testing Ltd (SMaRT) which is where these data shown below originates (32). The 02 and 03 welds were compared in terms of LCF performance (Table 5.2 & figure 5.29).

Sample	Weld	Temp (°C)	R Ratio	Maximum Applied Stress (Mpa)	Cycles to failure
LCF001	02	150	0.1	650	100000 (Run Out)
LCF002	02	150	0.1	750	11970
LCF003	02	150	0.1	700	25883
LCF004	02	150	0.1	850	61
LCF005	02	150	0.1	800	594
LCF006	02	150	0.1	800	628
LCF009	03	150	0.1	650	100000 (Run Out)
LCF010	03	150	0.1	750	12623
LCF011	03	150	0.1	700	33772
LCF012	03	150	0.1	850	51
LCF013	03	150	0.1	800	470
LCF014	03	150	0.1	750	14587

Table 5.2: Results of LCF produced by SMaRT carried out for Rolls-Royce, plc at the Swansea Materials Research & Testing facility (32)

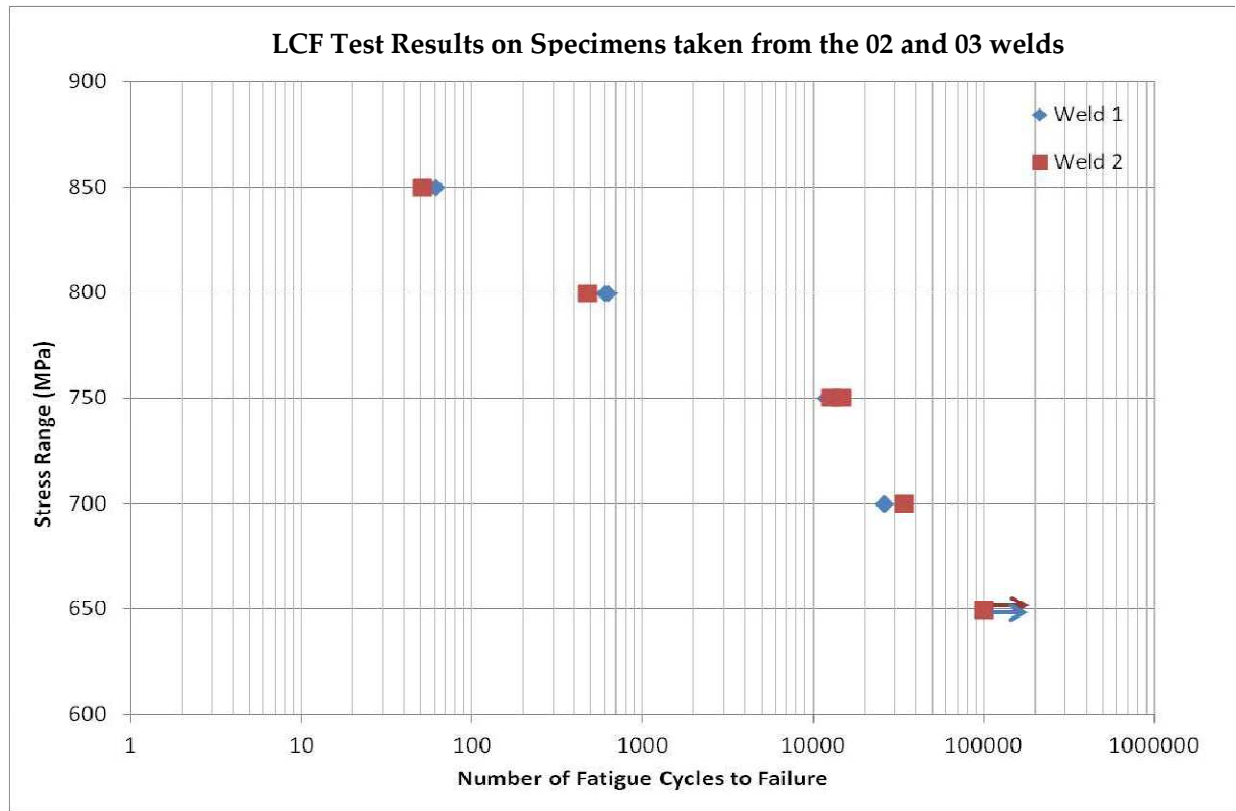


Figure 5.29: S-N curves for LCF data produced by SMaRT and carried out for Rolls-Royce, plc at the Swansea Materials Research & Testing facility (32)

As shown in figure 5.29, the LCF properties are very comparable in both the 02 and 03 weld. The results, like those for tensile testing meet the standards acceptable by Rolls-Royce, plc and are therefore deemed acceptable for application. Mohandas et al (1996) also stated that the desirable LCF behaviour is a result of the very fine transformed β grains in the weld zone and the absence of primary α . He also found LCF properties in his work on LFW of Ti64 to be enhanced compared to that of the parent material with a significantly higher number of cycles to failure being recorded [69].

5.2.3 Effect of welding parameters, weld orientation and temperature on mechanical threshold and crack propagation

The crack propagation and threshold are something that can be assessed specifically within the weld zone unlike many other mechanical properties like LCF and Tensile strength. The fundamental principles behind these tests is to establish how the material will behave if a crack is initiated within the weld region itself. This must be compared to the parent material, different orientations within the weld and also at low and elevated temperature.

The crack growth rate was much greater than that within the parent material. This is due to the refined microstructure within the weld region and suggests that a crack initiating in the weld would grow faster than within the parent. This is perhaps a limitation of welded samples and unlike other mechanical properties is inferior to the parent. This can be seen within figure 5.30. It should be noted however, that while the parent material may be expected to show slower crack growth the difference in this is normally much closer as shown.

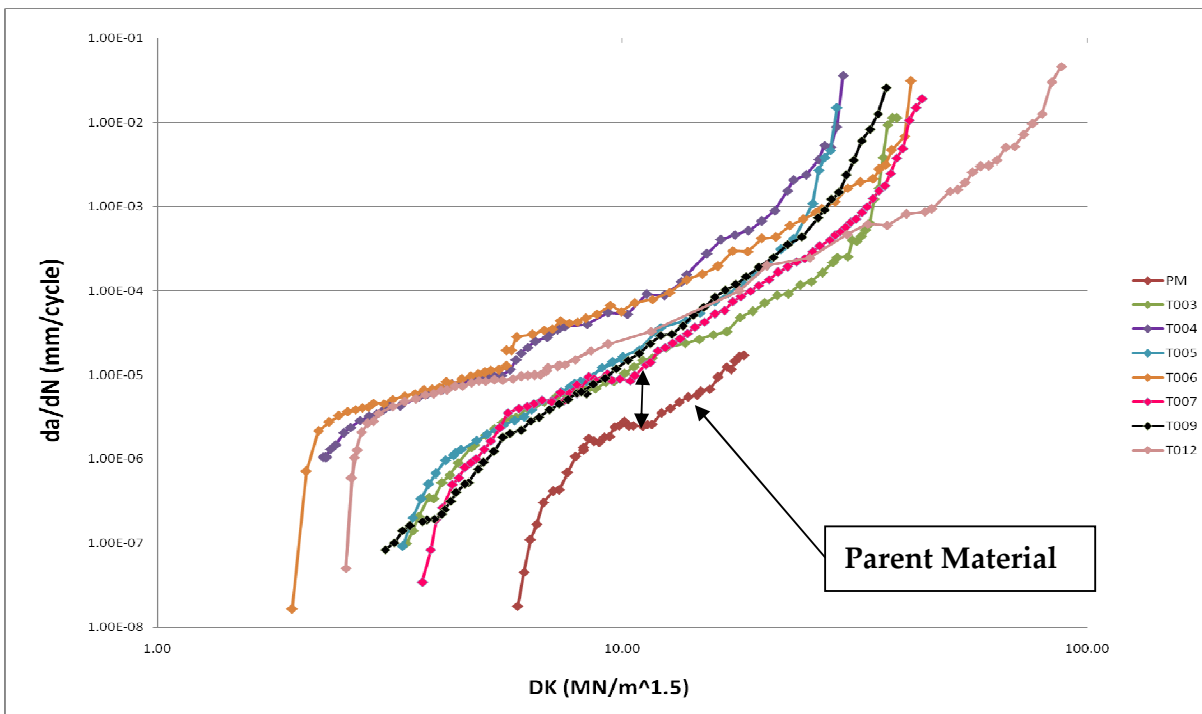


Figure 5.30: Effect of stress intensity factor (ΔK) on crack growth rate within the weld zones (T003-T012) and the parent material

The weld zones were compared in terms of both performance at room temperature and elevated temperature (400°C) and also the orientation within the weld that the crack was growing. Figure 5.31 & 5.32 show the crack growth behaviour in the hoop compared to the radial orientation at both room temperature and 400°C .

Figure 5.31 shows that the crack growth rate was higher in the radial direction than the hoop direction at room temperature. This was the case in both the threshold region (low ΔK) and in the crack propagation region (high ΔK). However, when the temperature was increased to 400°C the opposite effect was observed during the crack propagation phase. The mechanical threshold was similar although the crack still appeared to grow within the radial direction for longer at very low stress intensity. This relationship continued throughout the Paris region until ΔK was increased more rapidly. Once this occurred, the crack growth rate increased dramatically in the hoop direction, where the increase in growth rate in the radial direction was less dramatic.

This suggests that a rise in temperature has a bigger effect on crack growth rate during the crack propagation phase in the hoop direction than in the radial direction. A rise in temperature is relatively insignificant at low ΔK as the material reaches its threshold value within the Paris region.

The crack growth rate in terms of the effect of weld orientation can be seen more clearly within figures 5.33 & 5.34. In figure 5.31 it can be seen quite noticeably that temperature has a dramatic effect on crack growth when in the hoop direction. The crack growth at low ΔK is still quite fast and then suddenly the mechanical threshold is reached and no more crack movement can be seen. This suggests that an increase in temperature leads to an increase in crack growth rate but threshold is reached when reasonably high stresses are still being placed on the material. The reason for this increase in temperature leading to an early onset of crack growth rate in the hoop direction (figure 5.33) is most likely down to creep deformation. Generally creep deformation will occur above 350°C . This along with the very fine microstructure in the CZ as a result of the IFW process the resistance to creep is

reduced. This was also found by Pardhi et al (2009) and Roder et al (2006), both studying the effects of temperature on crack growth in Ti6246 [59, 60].

The opposite effect however, is seen within the radial direction, as can be seen in figure 5.34. The increase in temperature appears to reduce the crack growth rate as the curves cross over within the Paris region. When ΔK is low at elevated temperature this shows an elevated crack growth rate compared to the growth at room temperature, although the threshold is only reached once the ΔK has been reduced to a much lower value. Then as the ΔK is increased and crack propagation occurs the opposite effect is observed compared to that observed in the hoop direction. This increase in temperature during propagation of the crack leads to a decrease in crack growth rate compared to room temperature. This phenomenon of slow crack growth at room temperature and then a rapid increase once a certain ΔK is reached was found by Pardhi et al (59). Pardhi's work on fractography suggested the cracks grew by transgranular crack growth at low ΔK but mixed mode and sometimes only intergranular crack growth with an increase in ΔK [59]. This crossover point occurs within the Paris region where crack growth begins to accelerate and a change in growth mode is apparent. As these stress intensities increase the plastic zone sizes increase. When these zones become larger than the grain size, the grain boundaries fail and intergranular crack growth can occur, which is far more rapid than that of the transgranular mode, known as Irwin's approximation [59, 61 & 62].

The variation observed in figures 5.33 & 5.34 therefore, may be explained by the grain size in the hoop and radial direction. It suggests that grain growth may occur in the hoop direction when the temperature is increased to 400°C (nearing PWHT temperature), perhaps due to the orientation, thus restricting accelerated crack growth, although this must be investigated further.

The decrease in ΔK at room temperature is more rapid than at elevated temperatures as shown clearly in figure 5.33 & 5.34. This observation was also found by Pardhi et

al (2009) in Ti6246. This suggests that the fracture toughness of the material may be lower at room temperature [59].

The final variable to consider is that of the welding parameters. This can be analysed using figures 5.31 & 5.32. In figure 5.31 at room temperature, the 02 welds seem to represent faster crack growth rates at high ΔK (crack propagation) than those of the 03 welds but only in the hoop direction. This can also be observed at 400°C. The reasons for this are most likely due to a finer microstructure with the 02 welds due to the increased cooling rate. As discussed already Irwin's approximation suggests that intergranular (more rapid) crack growth occurs when the plastic zone size becomes larger than the grain size [62]. Therefore due to the microstructure being more refined in the 02 weld than the 03 weld this change in crack growth mode will occur sooner and therefore leading to an increase in crack growth rate at a lower ΔK than the 03 weld. The graphs also show that an increase in temperature has an effect on this onset in rapid crack growth with this transition being more distinct at room temperature (figure 5.31). Again this could be due to Irwin's approximation.

The stage where this sudden increase in crack growth occurs appears to be generally in the region of 22-29 ΔK , which is very similar to that observed by Pardhi ($\Delta K = 23$) although this may not be comparable as his work was carried out in Ti6246 [3, 64].

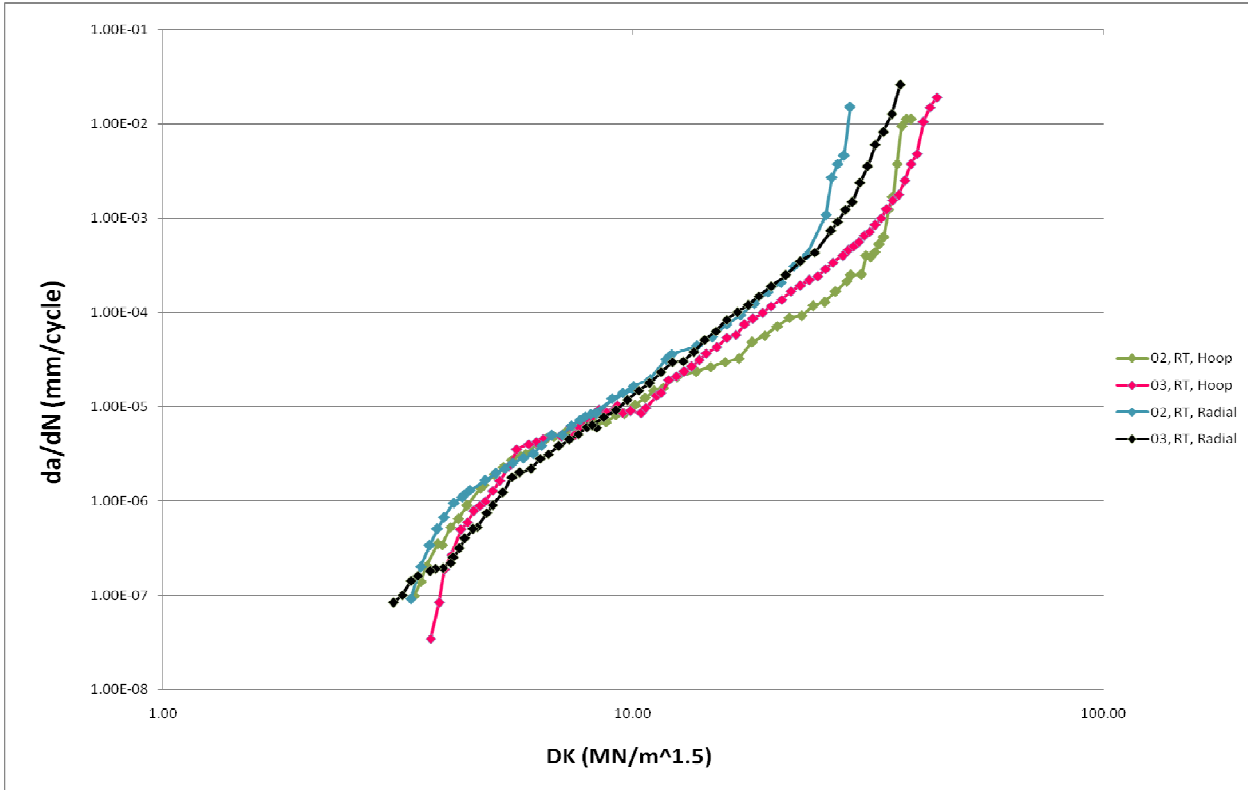


Figure 5.31: Effect of stress intensity factor (ΔK) on crack growth rate at RT in the Hoop and Radial direction

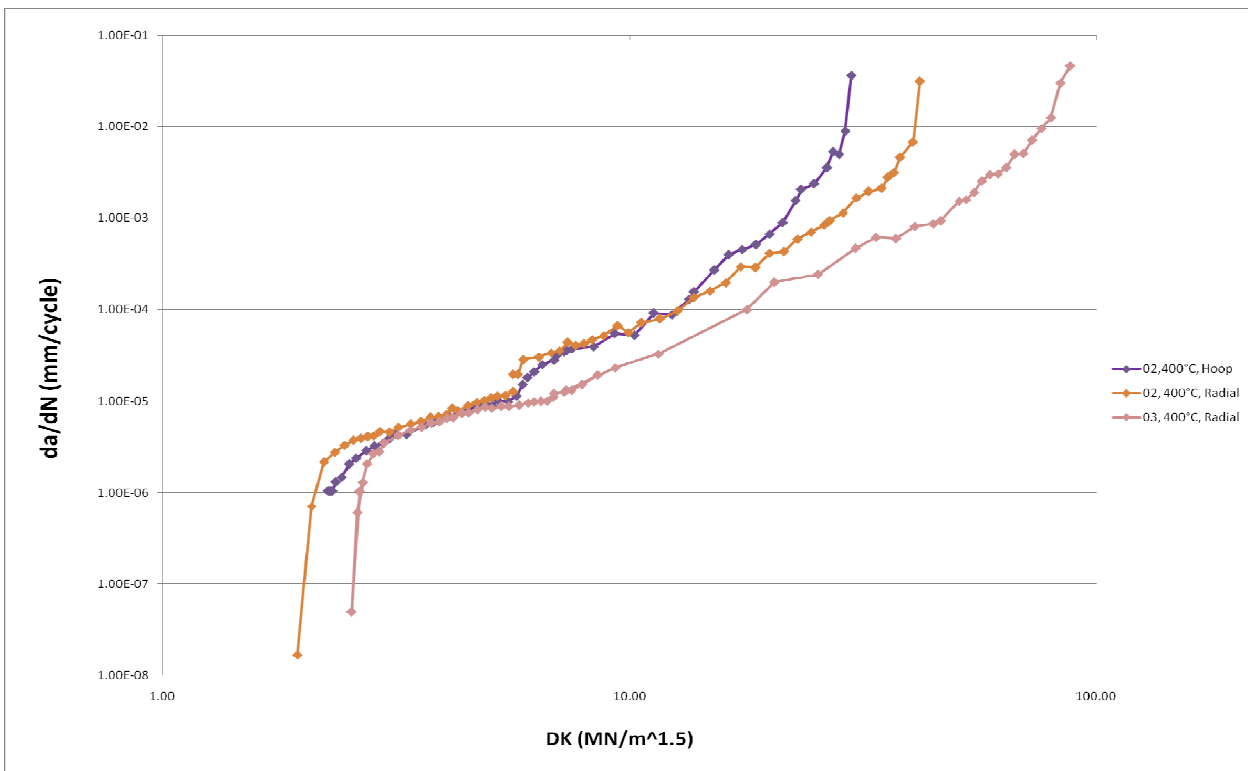


Figure 5.32: Effect of stress intensity factor (ΔK) on crack growth rate at 400°C in the Hoop and Radial direction

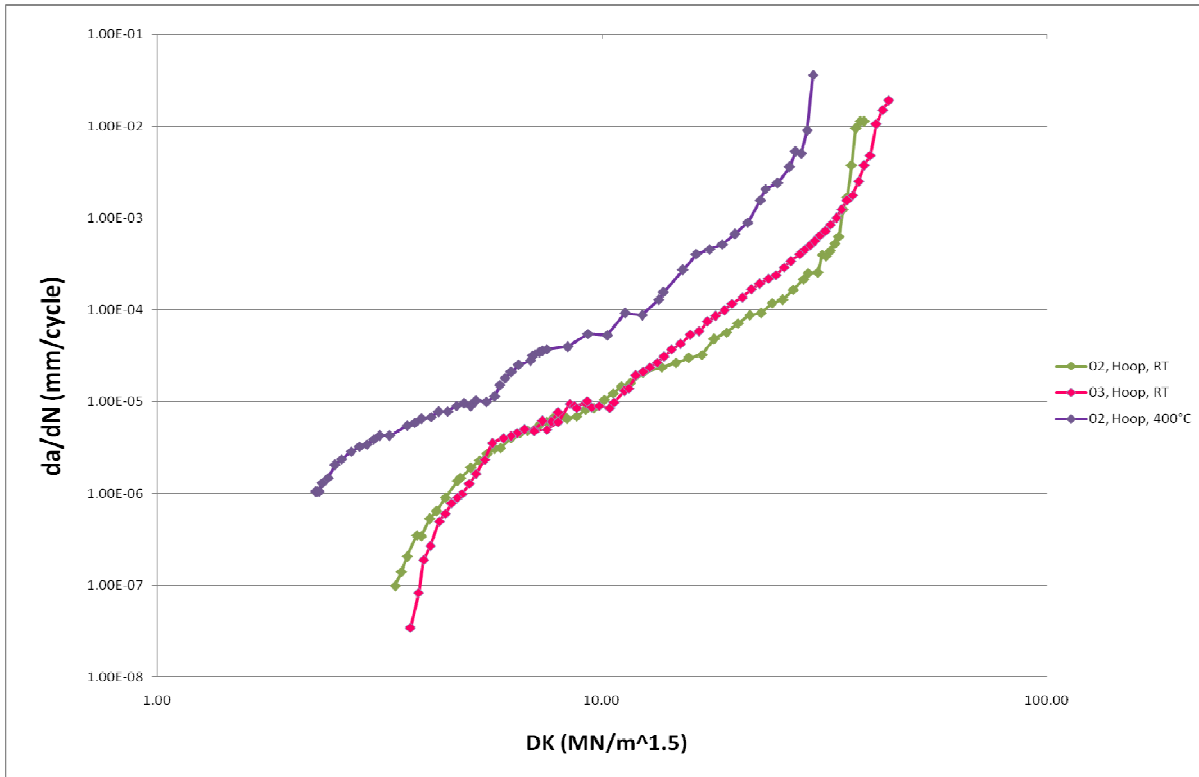


Figure 5.33: Effect of stress intensity factor (ΔK) on crack growth rate in the Hoop direction at RT and 400°C

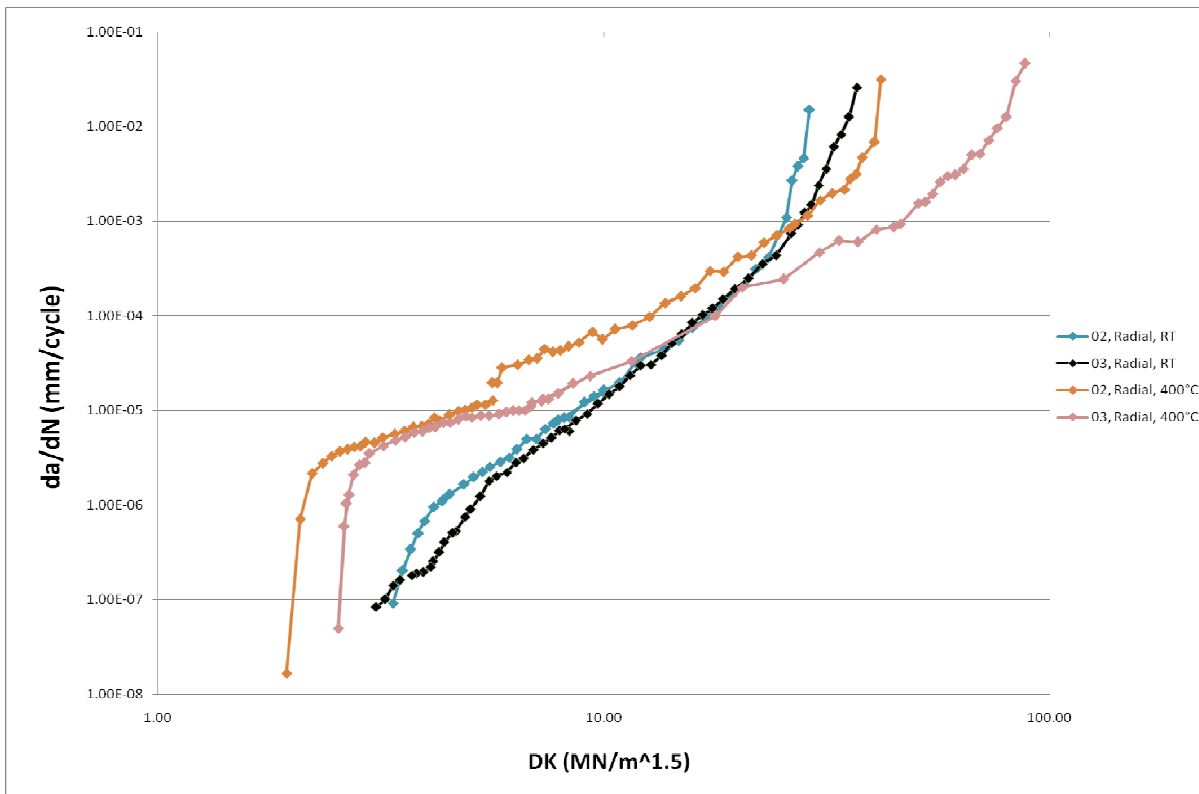


Figure 5.34: Effect of stress intensity factor (ΔK) on crack growth rate in the Radial direction at RT and 400°C

5.2.4 Effect of welding parameters, weld orientation and temperature on Fracture toughness

Fracture toughness is the final mechanical property that will be discussed. The results of the fracture toughness testing can be seen below in table 5.3. The variables that were used were the weld, R ratio, weld orientation/direction and also the temperature.

Sample	Weld Description	R	Direction	Temp (°C)	$K_q/\text{MPam}^{0.5}$
FT003	PDRIW119-02	0.1	Radial	RT	30.956
FT004	PDRIW119-02	0.1	Hoop	400	57.985
FT005	PDRIW119-02	0.1	Radial	400	56.545
FT006	PDRIW119-02	0.5	Hoop	RT	41.175
FT008	PDRIW119-02	0.5	Hoop	400	57.408
FT009	PDRIW119-03	0.1	Radial	400	64.598
FT010	PDRIW119-03	0.1	Hoop	400	63.093
FT011	PDRIW119-03	0.5	Radial	400	63.895
FT013	PDRIW119-03	0.1	Radial	RT	44.318
FT014	PDRIW119-03	0.5	Hoop	400	66.037
FT015	PDRIW119-03	0.1	Radial	RT	41.802
FT016	PDRIW119-03	0.5	Hoop	RT	48.225

Table 5.3: Summary of the fracture toughness testing results that was carried out on 12 samples provided by Rolls Royce, Plc

The results clearly show an immediate trend in that the fracture toughness work carried out at elevated temperature (400°C) exhibit a noticeable increase in fracture toughness than those tested at room temperature. The weld, R ratio and also weld orientation appear to have very little effect on the trend on these results.

The effect of the microstructure on the fracture toughness of materials may be down to two main parameters suggests Kwietniewski et al (2006). Firstly crack path tortuosity or the difficulty provided by the microstructure to the growth of cracks.

Secondly plastic deformation along the crack of the path. If both of these two factors are at a maximum then the fracture toughness will be at its highest [65]. Toughness is dependent on factors that prevent crack propagation as opposed to those that prevent crack initiation.

The reasons for the increase in temperature increasing the fracture toughness of the material could be related to that observed in the crack propagation results. As the increase in temperature leads to an increase in the grain size within the material, perhaps the cracks are forced to grow trans-granularly rather than inter-granularly as the force applied is not sufficient to produce a plastic zone greater than the grain size and therefore making this crack propagation more difficult. This in turn leads to a higher applied stress being required to plastically deform the material enough to cause failure [64]. This is proved by the fracture images shown in the 02 weld figures 5.35 & 5.36 at both room temperature and 400°C and also in the 03 weld (figure 5.37 & 5.38) at room temperature and 400°C.

It can be seen that the fracture surface of the samples from both welds tested at room temperature (figures 5.35 & 5.37) have a very smooth fracture surface due to trans-granular crack growth which resulted in the low fracture toughness values. Where in figures 5.36 & 5.38 where the crack underwent a difficult path via inter-granular growth, the fracture surface is very irregular due to the crack growth occurring in different directions and shear lips being apparent on the fracture surface [67, 68]. These shear lips occur when the crack growth is occurring at more than 45°C to the loading direction [66].



Figure 5.35: Fracture surface of respective 02 weld samples FT003 (Hoop) and FT006 (Radial) at RT



Figure 5.36: Fracture surface of respective 02 weld samples FT004 and FT008 (Hoop) and FT005 (Radial) at 400°C

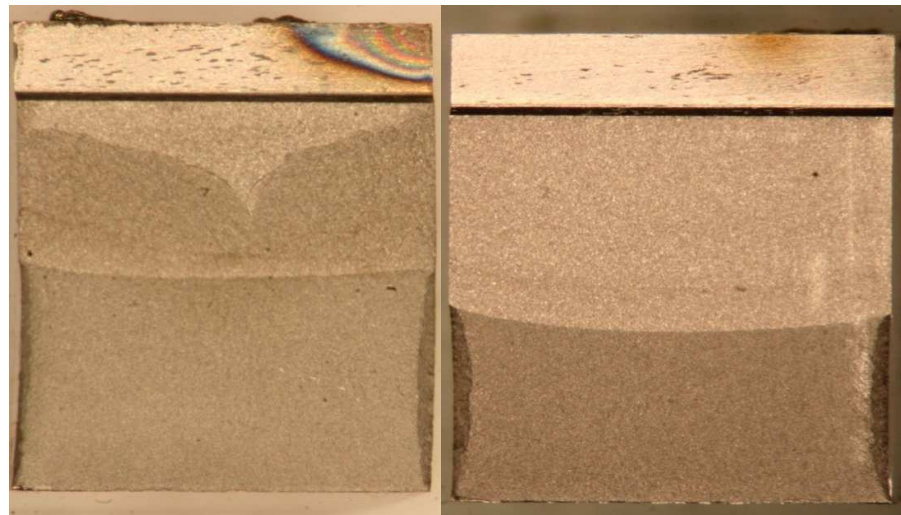


Figure 5.37: Fracture surface of respective 03 weld samples FT016 (Hoop) and FT013 (Radial) at RT

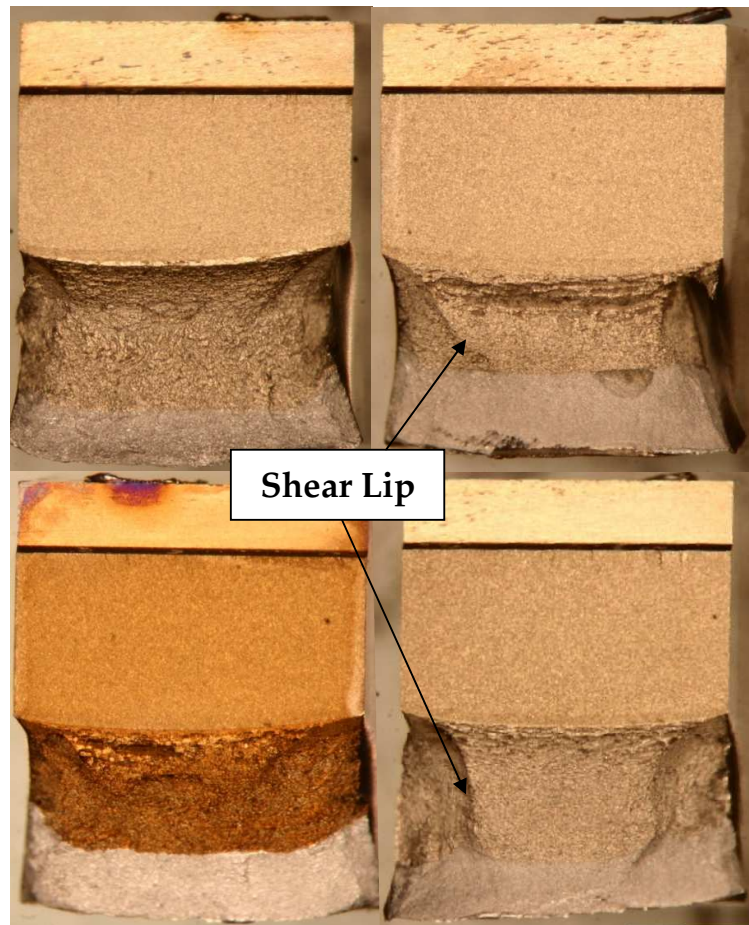


Figure 5.38: Fracture surface of respective 03 weld samples FT010 & FT014 (Hoop) at the top and FT009 & FT011 (Radial) at the bottom at 400°C

CHAPTER 6 CONCLUSIONS

6.1 Microstructure development in inertia welded Ti64 and its effect on micro-hardness

The microstructure developed during the Inertia Welding process is quite different to that of the parent material. The microstructure of the CZ was very refined and almost identical to that observed in LFW of Ti64. There were noticeable variations within this microstructure with distance from the weld interface with more characteristics of the parent being observed. Within the TMAZ slight variations were observed leading to an inner and outer zone to be defined and flow was observed within the hoop direction. The microstructure of the HAZ was very similar to that of the parent. There were a number of variables that influenced the development of the observed microstructure. This includes speed of rotation, pressure and local temperature at the weld interface. However, it can be said that the overall controlling parameter of the microstructure was the cooling rate.

The faster the cooling rate the more refined the microstructure became and this in turn resulted in higher peak hardness values within the CZ due to martensitic transformation. The micro-hardness then drops off through the TMAZ and HAZ until the post weld parent material hardness is reached. The hardness within the HAZ is often lower than the parent. These findings are very similar to the work done on LFW in Ti64 and it can be said that inertia welding of Ti64 produces a microstructure with superior hardness properties to the parent.

6.2 Mechanical properties in inertia welded Ti-64

The mechanical properties assessed suggest that Inertia welded Ti64 offers performance very similar to that of LFW of Ti64. The tensile strength of the weld was not assessed directly although the failure will always occur outside of the weld zone. Therefore, it can be said that the weld does not affect the integrity of the material. However, the tensile strength is considerably higher at room temperature than at elevated temperatures. The LCF behaviour of the weld was superior to that of the parent, although not as desirable as the LCF in LFW.

The crack growth behaviour showed that crack growth in the inertia welded Ti-64 is more rapid than that observed in the parent material. The rate was slower in the hoop direction than radial direction at room temperature although this trend is reversed when the temperature of the surrounding environment is elevated. This is most likely due to grain growth in the hoop direction with an increase in temperature, along with the crack growth mechanism mode becoming intergranular as opposed to transgranular much earlier than that of cracks in the hoop direction. The resultant microstructure as a result of the welding process also affected the crack growth behaviour with more refined microstructures as a result of faster cooling rate experiencing more rapid crack growth due to intergranular crack growth sooner than that of the less refined microstructure. Similar behaviour was the result of higher fracture toughness values being obtained at elevated temperature. The increase in grain size at the elevated temperatures resulted in transgranular growth occurring and failure occurred when the applied stress is high enough to cause the material to shear.

6.3 General conclusions

The Inertia welding of Ti64 on small scale welds suggests that this process is a suitable application for producing modular fan disks. The microstructure and micro-hardness are superior to that of the parent material. Failure due to low cycle fatigue or tensile failure will not occur as a result of the weld. The crack growth behaviour may not be as desirable as the parent material although this requires further research. The increase in crack growth rate due to an increase in temperature will not be an issue as the fan disk will not be exposed to these elevated temperatures during service.

CHAPTER 7 FUTURE WORK

Although the work carried out so far on Inertia welded Ti64 is very promising, much work is still required in order to be able to confidently justify using this process for fan disk production in the future.

More testing is required into the crack growth behaviour in the weld zone compared to the parent material and whether this will be detrimental to the performance of the disk. Along with this, more work is required into the effect of grain size on this crack growth rate and its significance.

This work must also be carried out on progressively larger scales to assess whether the processing parameters will have an effect on larger welds. The reason for this is that the cooling rate has been found to be the most significant factor on the microstructure formed and the resultant mechanical properties. Will the increase in size of components being welded (as with full scale production) lead to a greatly reduced cooling rate and prevent these desirable features being obtained?

REFERENCES

- 1) P. Spittle, (2003). Gas turbine technology. Physics education. 38 (6): pp. 504-511.
- 2) Power Jets. 2013. History of the Jet. [Online]. Available from <http://www.powerjets.co.uk/History.html> [Accessed 12 October 2013]
- 3) Y. U. Pardhi, (2010). Microstructure evolution and its effect on fatigue performance in inertia welds of Titanium and Nickel based alloys. (PhD thesis), University of Birmingham, Birmingham, UK
- 4) Rolls Royce, (2012) Large aircraft engines [online] Available from <http://www.rolls-royce.com/> [Accessed 28 November 2012]
- 5) Rolls-Royce, (2012) Rolls-Royce Holdings Plc Annual Report [Online] Available from <http://www.designworldonline.com/parker-aerospace-awarded-rolls-royce-supplier-of-the-year-for-gas-turbines/> [Accessed 12 October 213].
- 6) A. M. M, García (2011). BLISK Fabrication by Linear Friction Welding, Advances in Gas Turbine Technology, Dr. Ernesto Benini (Ed.), ISBN: 978-953-307-611-9, InTech, Available from <http://www.intechopen.com/books/advances-in-gas-turbine-technology/blisk-fabrication-by-linear-frictionwelding> [Accessed 12 October 2013]
- 7) G. Welsch, R. Boyer & E. W. Collins (1994). Materials Properties Handbook: Titanium Alloys. Materials Park, OH : ASM International
- 8) Y. Guuo (2012) Microstructure characterisation of linear friction welded titanium alloys using EBSD and TEM. (PhD thesis), University of Birmingham, Birmingham, UK.
- 9) D.J. Jarvis & G. Voss (2005). IMPRESS Integrated Project – An overview paper. Materials Science and Engineering A. Vol. 413–414, Pages 583–591.
- 10) M. J. Donachie (Jr), Ed. Titanium and Titanium Alloys. Ohio: American Society for Metals, 1982.

- 11) I. J. Polmear, Light Alloys, 4th ed. Butterworth-Heinemann, 2006.
- 12) P. Wanjara & M. Jahazi, "Linear friction welding of Ti-6Al-4V: processing, microstructure and mechanical property inter-relationships," Metallurgical and Materials Transactions A, vol. 36A, no. 8, pp. 2149-64, 2005.
- 13) NDT Resource centre (2013). S-N Fatigue Properties. [Online] Available from <http://www.ndt-ed.org/EducationResources/CommunityCollege/Materials/Mechanical/S-NFatigue.htm> [Accessed 25 October 2013]
- 14) M. E. Fine, Y. W. Chung & R. R. McCormick, "Fatigue failures in metals," in fatigue and fracture: ASM Handbook. ASM International, 1996, vol. 19, pp. 63-72.
- 15) M.J. Donachie (Jr). Ed., Titanium: A technical guide, 2nd ed. ASM International, 2000.
- 16) J. Polmear, Light Alloys, 4th ed. Butterworth-Heinemann, 2006.
- 17) C. A. Stubbington and A. W. Bowen, "Improvements in the fatigue strength of Ti-6Al-4V through microstructure control," Journal of materials science, vol. 9, no. 6, pp.941-947, 1974.
- 18) M. R. Bache, W. J. Evans and M. McElhorne, "Effects of environment and internal oxygen on fatigue crack propagation in Ti-6AL-4V", journal of Materials Science and Engineering A, volume A, pages 918-922, year 1997.
- 19) V. Sinha, C. Mercer, and W. O. Sobeyejo, "Investigation of short and long fatigue crack growth behaviour of Ti-6AL-4V," Materials Science and Engineering A, vol. 287, no. 1, pp. 30-42, 2000.
- 20) R. O. Ritchie, B. L. Boyce, J. P. Campbell, O. Roder, A. W. Thompson, and W. W. Milligan, "Thresholds for high-cycle fatigue in a turbine engine Ti-6Al-4V alloy," International journal of fatigue, vol. 21, no. 7, pp. 653-662, 1999.
- 21) R. O. Ritchie, S. Suresh, J. W. Hutchinson, W. W. Milligan & A. W. Thompson, "High-cycle fatigue and time-dependent failure in metallic alloys for propulsion systems" Tech. Rep. ADA368794, 01 SEP 1999, <http://citeseer.ist.psu.edu/448248.html>

- 22) C. Leyens & m. Peters, Titanium and Titanium alloys: Fundamentals and applications. Wiley-VCH, 2003.
- 23) T. Mohandas, M. Srinivas and V. V. Kutumbarao, "Effects of post-weld heat treatment on fracture toughness and fatigue crack growth behaviour of electron beam welds of a titanium ($\alpha + \beta$ alloy), "Fatigue and Fracture of Engineering Materials and Structures, vol. 23, no. 1, pp. 33-38, 2001.
- 24) M, Aritoshi & K. Okita, "Friction welding of dissimilar metals," Yosetsu Gakkai Shi/Journal of the Japan welding society, vol. 71, no. 6, pp. 20-24, 2002.
- 25) R. Sahoo & P. Samantaray (2007). Study of Friction Welding. (PhD thesis). [Online] available from <http://ethesis.nitrkl.ac.in/4236/1/STUDY-OF-FRICTION-WELDING.pdf> [Accessed 25 October 2013]
- 26) M. E. Nunn, "Aero engine improvements through linear friction welding," 1st International Conference on Innovation and Integration in Aerospace Sciences, Queens University Belfast, Northern Ireland, UK, 4-5 August 2005.
- 27) K. K. Wang, "Friction welding," Welding Research Council Bulletin, no. 204, p.21, 1975.
- 28) L. Bjerregaard, K.G., B. Ottesen, and M. Ruckert, Metalog Guide2002, Denmark: Strusters A/S. 18-19.
- 29) E.A. Brandes, e., Smithells Metals Reference Book. 6th ed1983, London: Butterworth & Co (Publishers) Ltd.
- 30) British Standards Institute, (1998). "BS 6835-1:1998: method for the determination of the rate of fatigue crack growth in metallic materials; Part 1: Fatigue crack growth rates above 10^{-8} m per cycle," BSI, p. 30, December 1998.
- 31) E. F. Walker & m. J. May, "Compliance functions for nvariance tyoes of test specimen geometry," BISRA open report, Tech. Rep. MG/E/307/67, 1967.
- 32) R. J. Lancaster (2013). Mechanical Evaluation of Inertia Welded Titanium 6/4, Swansea: Swansrea Materials Research & Testing Ltd
- 33) SMaRT (2013). SMaRT_QS5.4d(1) STOP_LCF Force Controlled LCF Testing, Swansea, UK

- 34) British Standards Institute, (2011). BS6072:2011 Aerospace series. Metallic materials. Test methods. Constant amplitude fatigue testing. Milton Keynes, BSI.
- 35) The Institute of Materials, Minerals and Mining (2013). MMM31005 Materials and Mechanical Methods: Test Method and Data Analysis For Tensile Testing of Metallic Materials, London, UK
- 36) SMaRT (2013). SMaRT_QS5.4d(2) STOP_TMM Test Methods and Data Analysis for Tensile Testing of Metallic Materials, Swansea, UK
- 37) British Standards Institute (2013). BS EN ISO 6892-2:2011 Metallic materials. Tensile testing. Method of test at elevated temperature. Milton Keynes, BSI.
- 38) R. J. Lancaster (2013). Mechanical Evaluation of Inertia Welded Titanium 6/4, Swansea: Swansea Materials Research & Testing Ltd
- 39) R. J. Lancaster (2013). Mechanical Evaluation of Inertia Welded Titanium 6/4, Swansea: Swansea Materials Research & Testing Ltd
- 40) Key to Metals (2013). Heat treating of Titanium and Titanium Alloys [Online] Available from <http://www.keytometals.com/Article97.htm> [Accessed 5 November 2013]
- 41) C. Sauer & G. Luetjering, "Thermo-mechanical processing of high strength β -titanium alloys and effects on microstructure and properties," Journal of Materials Processing Technology, vol. 117, no. 3, pp. 311317, 2001.
- 42) P. Wanjara & M. Jahazi, "Linear friction welding of Ti-6AL-4V: processing, microstructure and mechanical property inter-relationship," Metallurgical and Materials Transactions A, vol. 36A, no. 8, pp. 2140-70, 2005.
- 43) W. A. Baeslack, D. Phillips, C. English, & A. P. Woodfield, "Inertia friction welding of an advanced rapidly solidified titanium alloy, "Journal of Materials Science Letters, vol. 10, no. 23, pp. 1401-8, 1991.
- 44) A. A. M da Silva, A. Meyer, J. F. dos Santos, C. E. F. Kwietnieski, & T. R. Stroehaecker, "Mechanical and metallurgical properties of friction welded TiC

- particulate reinforced T-6Al-4V," Composites Science and Technology, Vol, 64, no. 10-11, pp. 1495-1501, 2004.
- 45) J. Romero, M.M. Attallah, M. Preuss, M. Karadge, and S. Bray, Effect of the forging pressure on the microstructure and residual stress development in Ti-6Al-4V linear friction welds. *Acta Materialia*, 2009. 57(18): p. 5582-5592.
- 46) P. Wanjara and M. Jahazi, Linear Friction Welding of Ti-6Al-4V: Processing, Microstructure, and Mechanical -Property Inter-Relationships. *Metallurgical and Materials Transaction A* 2005. 36A: p. 2151-2164.
- 47) I. Katarov, S. Malinov, and W. Sha, Finite Element Modeling of the Morphology of α to β Phase Transformation in Ti-6Al-4V Alloy. *Metallurgy and materials transaction A*, 2002. 33A: p. 1027-1041.
- 48) M.J. Donachie and JR, eds. Titanium and titanium alloys. 1982, American society for metals, Metals Park: Ohio. 392.
- 49) R. Boyer, G. Welsch, and E.W. Collings, Materials Properties Handbook---- Titanium Alloys. 1994: ASM international.
- 50) Carpenter (2013). A technical data sheet, Titanium Alloy Ti 6Al-4V. [Online] Available from <http://cartech.ides.com/datasheet.aspx?i=101&E=269> [Accessed 12 December 2013].
- 51) Y. Karpat (2011). Temperature dependent flow softening of titanium alloy Ti6Al4V: An investigation using finite element simulation of machining. *Journal of Materials Processing Technology*, Vol. 211, Issue 4, 1 April 2011, Pages 737–749
- 52) J. Sorina-Müller, M. Rettenmayr, D. Schneefeld, O. Roder, and W. Fried, FEM simulation of the linear friction welding of titanium alloys. *Computational Materials Science*, 2010. 48(4): p. 749-758.
- 53) E. Boswell, Direct Thermocouple Temperature Measurement of Ti-64: Ti-64, Ti-6246: Ti-6246 and Ti-6246: Ti-64 material combination linear friction welds on the PDS machine, 2001, Rolls-Royce plc, Derby, Internal report.
- 54) E. Dalgaard, F. Coghe, L. Rabet, M. Jahazi, P. Wanjara, and J.J. Jonas, Texture Evolution in Linear Friction Welded Ti-6Al-4V in Thermec 2009 N.W. T.Chandra, W.Reimers, M.Ionescu, Editor. 2010, Advanced Materials Research p. 124-129.

- 55) N. Gey and M. Humbert, Specific analysis of EBSD data to study the texture inheritance due to the $\beta \rightarrow \alpha$ phase transformation. *Journal of Materials Science*, 2003. 38(6): p. 1289-1294.
- 56) J.J. Kearns, On the relationship among 'f' texture factors for the principal planes of zirconium, hafnium and titanium alloys. *Journal of Nuclear Materials*, 2001. 299(2): p. 171-174.
- 57) Y. Pardhi, C. Dungey, G. Baxter, P. Bowen and T. P. Halford (2010). Fatigue Crack Propagation Behaviour of an Inertia Friction Welded α/β Titanium Alloy. *Journal of ASTM International*, Vol. 7, No. 6
- 58) O. Roder, D. Helm and G. Lutjering (2003). "Microstructure and Mechanical properties of Inertia and Electron Beam Welded Ti-6246" Tenth world conference on Titanium, Hamburg, Germany, 13-18 July 2003, Gerd Luetjering and Joachim Albrecht, eds., Wiley VCH, Weinheim, Germany, pp. 2875-2882.
- 59) W. A. III. Baeslack and Y. Mahajan (1979). "Intergranular fracture of heat treated weldments in a High strength Alpha-Beta Titanium Alloy" *Scr. Metall.*, Vol. 13, 1979, pp. 959-964.
- 60) S. Suresh, (2004). *Fatigue of Materials*, 2nd ed., Cambridge University Press, Cambridge, UK, 204, pp.331-382.
- 61) D. R. Askeland (1994). *The science and engineering of materials*, third edition. PWS Publishing Company, United States of America.
- 62) C. Kwietniewski, J. F. Santos, A. A. M. da Silva, L. Pereira, T. R. Strohaecker & A. Reguly (2005). "Effect of plastic deformation on the toughness behaviour of radial friction welds in Ti-6Al-4V-0.1Ru titanium alloy". *Materials Science and Engineering A417* (2006) pp.49-55
- 63) Liu, A. (2005). *Mechanics and Mechanisms of Fracture: An Introduction*, ASM International.
- 64) M. J. Mullen, A. H. Griebel & J. M. Tartaglia (2007). *Fracture Surface Analysis*. Advanced Materials and Processes/December 2007. Stork Climax Research Services, Wixom, Michigan.
- 65) M. Corzo, Y. Torres, M. Anglada & A. Mateo (2007). "Fracture Behaviour of Linear Friction Welds in Titanium Alloys". *Anales de la Mecanica de Fractura*,

Vol 1(2007). Dpto Ciencia de los Materiales e Ingeneira Metalurgica,
Universitat Politecnica de Catalunya, Av. Diagonal647, 08028-Barcelona,
Espana

- 66) T. Mohandas, V. K. Varma, V. V. Kutumbarao & D. Banerjee (1996). "Low Cycle Fatigue Behaviour of Electron Beam and Friction Welded Joints of an α - β Titanium Alloy". Scripta Materialia, Vol. 35, No. 2, pp.187-192, 1996. Elsevier Science Ltd, Acta Metallurgica Inc, USA.
- 67) M. M. Attallah & M. Preuss (2011). Inertia friction welding for aerospace applications. University of Birmingham and University of Manchester, UK, Woodhead Publishing Limited
- 68) W. Y. Li, T. Ma, Y. Zang, Q. Xu, J. Li, S. Yang & H. Liao (2008). "Microstructure Characterization and Mechanical Properties of Linear Friction Welded Ti-6Al-4V alloy". Advanced Engineering Materials 2008, 10, No. 1-2.Wiley –VCH Verlag GmbH & Co. KGaA, Weinheim.
- 69) P. Wanjara, & M. Jahazi (2005). "Linear Friction Welding of Ti-6Al-4V: Processing, Microstructure and Mechanical-Property Inter Relationships". Metallurgical and Materials Transactions A, 2150-Vol. 36A, National Research Council, Montreal, Canada.
- 70) ASTM Standard E 647 - 08, 2003, "Standard Test Method for Measurement of Fatigue Crack Growth Rates," ASTM International, West Conshohocken, PA
- 71) ASTM Standard E 1820 - 05, 2005, "Standard Test Method for Measurement of Fracture Toughness," ASTM International, West Conshohocken, PA
- 72) ASTM Standard E 399 - 90, 1990, "Standard Test Method for Plain-Strain Fracture Toughness of Metallic Materials," ASTM International, West Conshohocken, PA